Experimental and theoretical frameworks for enabling environmental synthetic biology

Thesis by
John P. Marken

In Partial Fulfillment of the Requirements for the
Degree of
Doctor of Philosophy in Bioengineering

CALIFORNIA INSTITUTE OF TECHNOLOGY
Pasadena, California

2023
Defended May 9, 2023

John P. Marken
ORCID: 0000-0001-9696-088X

ACKNOWLEDGEMENTS

Throughout my almost six years at Caltech, I have had the tremendous privilege of working on many different research questions through many different types of approaches. My hope when I began my journey here was to conduct research that was useful from both an engineering and a basic science mindset, and to do so in both experimental and theoretical domains. I am grateful to have been able to realize this goal, through the support of the many fantastic people that I have had the good fortune to work with.

I must begin by thanking my advisor, Richard Murray, whose unwavering support provided the foundation and confidence I needed to think of myself as an independent scientist and to actualize that self-conception. It is rare that an advisor can be so willing to follow you into so many different scientific directions, but it is due to the breadth of Richard's scientific expertise and the depth of his commitment to mentorship that I was so able to thrive during my time here.

I would also like to thank the many people involved with the Resnick Sustainability Institute, particularly Dianne Newman, Neil Fromer, Bruce Hay, Niles Pierce, Gözde Demirer, and Elliot Meyerowitz, for trusting me and my scientific vision to start and manage a collaboration which I am excited to continue developing over the next couple years.

Scientific growth occurs not just in the laboratory, but also in the classroom. I would specifically like to thank Lea Goentoro, Lulu Qian, Michael Elowitz, and Justin Bois for teaching deeply engaging courses that shaped the way I think about science, and I would particularly like to thank Michael and Justin for trusting my own pedagogical views enough to let me work with them to refine the content of the Biological Circuit Design course. My gratitude also extends to the fantastic professors I had in college at William and Mary, who provided me with a supportive environment to try bold things and to succeed and fail grandly. I would particularly like to thank professors Margaret Saha, Greg Conradi-Smith, Bev Sher, and Dan Cristol.

While I have written repeatedly about independence, science does not happen in a vacuum. The company of my scientific peers plays a major influence both in shaping the way that I approach scientific problems but also in continually revitalizing my excitement for these challenges. I must particularly thank Fangzhou Xiao, with whom I was fortunate to be able to begin a wonderful and ongoing collaboration

whose results make up the contents of Chapters 3 and 4 of this thesis. I would also like to thank the many friends and colleagues with whom I have initiated collaborations, many of which I could not describe in this thesis, including Andy Halleran (Operation Witchcraft), Andrey Shur (TouchColi), Elin Larsson (Stationary Phase), Ethan Jones (Synstainability), Gabe Salmon (KoaLAG), Liana Merk (Secretion), Mark Prator (Stationary Phase), Mengyi Cao (Worms), Rory Williams (Dps), and Victoria Chen (RMCE, Worms).

I would also like to thank the wonderful members of the Murray lab, who formed a kind and community throughout my time here. I would particularly like to acknowledge Alex Johnson, Anandh Swaminathan, Andy Halleran, Andrey Shur, Ayush Pandey, Chelsea Hu, Elin Larsson, James Parkin, Joe Meyerowitz, Leo Green, Liana Merk, Manisha Kapasiawala, Mark Prator, Matthieu Kratz, Mengyi Cao, Miki Yun, Reed McCardell, Rory Williams, Sam Clamons, Victoria Chen, Vipul Singhal, William Poole, Zach Martniez, and Zoila Jurado. I would also like to specifically express my gratitude for my wonderful friends and William and Mary compatriots Andy Halleran, Caroline Golino, and Sam Clamons, who provided me with the unique pleasure of blending a deep and natural friendship with engaging and exciting scientific discussions.

And finally, I would like to thank my loved ones, my family and my friends, who played a central role in shaping the person I am today. You are too many and your impacts are too deep to enumerate here, but you know who you are, and I will always be grateful for you.

ABSTRACT

Although the field of synthetic biology has made great advances toward becoming a mature engineering discipline over its first quarter-century, the vast majority of these efforts have focused on improving the design and performance of genetic circuits intended to operate in well-controlled, laboratory settings. The goal of safely deploying engineered microbes to reliably perform their programmed functions in natural, uncontrolled environments begets its own set of foundational challenges that will require new frameworks that shift our existing mindsets about the way we engineer biological systems.

These frameworks, because they focus on enabling system properties that were not priorities for conventional synthetic biology research, can constitute a new field of research which I refer to as *environmental synthetic biology*. The central priorities of environmental synthetic biology include (1) developing and characterizing effective ways to introduce engineered biological systems into natural environments, (2) ensuring that the performance of these systems can remain robust and predictable in the face of environmental variability, (3) developing and characterizing ways to control and monitor the behavior of an engineered system after deployment in an inaccessible environment, and (4) developing fundamental architectures to enable autonomous system operation and adaptation within environmental contexts.

In this thesis, I present the initial steps towards the development of three frameworks that address these priorities of environmental synthetic biology. The first framework, described in Chapter 2, demonstrates the potential of using DNA as the substrate for addressable and adaptable intercellular communication in engineered populations. This enables the ability to one day create multicellular systems that can autonomously reconfigure their own architecture in the face of changing environmental conditions. The second framework, described in Chapters 3 and 4, presents a new mathematical representation of biomolecular reaction systems that enables geometric bounds on the space of possible behaviors under all possible configurations for a particular system architecture. The third, ongoing framework emphasizes the importance of explicitly incorporating the physiological state of the host cell into the assessment of a genetic circuit's behavior by exploring the impact of cellular growth arrest on transcriptional response curves. The preliminary results of this work are presented in Chapter 5.

PUBLISHED CONTENT AND CONTRIBUTIONS

1 John P. Marken and Richard M. Murray. "Addressable and adaptable intercellular communication via DNA messaging". *Nature Communications* (2023). DOI: 10.1038/s41467-023-37788-z.
J.P.M. conceived and designed the project, performed the experiments, analyzed the data, and wrote the manuscript.

2 John P. Marken, Fangzhou Xiao, and Richard M. Murray. "A geometric and structural approach to the analysis and design of biological circuit dynamics: a theory tailored for synthetic biology". *bioRxiv Preprint* (2020). DOI: 10.1101/2020.02.18.953620.
J.P.M. and F.X. jointly developed the project and performed the analysis. J.P.M. wrote the manuscript with input from F.X.

TABLE OF CONTENTS

Chapter 1

INTRODUCTION

Some of the points presented in Section 1.2 of this chapter summarize concepts presented in the review

> Ethan M. Jones, John P. Marken, and Pamela A. Silver. "Synthetic microbiology for sustainability applications" (*Submitted*).
> E.M.J and J.P.M. jointly developed the narrative. J.P.M. wrote approximately half of the manuscript.

1.1 The need for environmental synthetic biology

In the year 2000, the publication of two seminal papers launched the field of synthetic biology. The construction of the Repressilator [1] and the genetic toggle switch [2] showed for the first time that transcription factors could be treated as modular components of a genetic programming language, and used to build circuits encoding fully-synthetic behaviors into living cells.

In the years that followed, the community made rapid advances in laying the foundations for synthetic biology to become a formal engineering discipline. These included efforts to standardize the construction and characterization of new genetic parts through the BioBricks format [3], develop comprehensive part libraries for various host organisms [4–7], and develop genetic insulation technologies to ensure that the performance of a part is consistent across different genetic contexts [8]. While these efforts are by no means complete, their successes so far have developed the field to the point where synthetic biology is now a cornerstone of many biotechnology companies in successful deployment today.

Now, as synthetic biology nears the completion of its first quarter-century, researchers are beginning to develop sophisticated synthetic biology systems intended for deployment in natural environments like the human gut [9] or farmland soils [10]. The design process for these systems, however, often involves a significant amount of troubleshooting and optimization because part performance does not often translate reliably between the well-controlled laboratory conditions where it was characterized and the variable environmental conditions of a target application. This means that such systems cannot fully benefit from the existing efforts towards

reliable engineering of synthetic biology devices, and instead must be conducted in an *ad hoc*, case-by-case manner.

In order to bring the level of consistency and reliability associated with mature engineering disciplines to the design process for these systems, additional efforts must be made to address fundamental challenges that are shared by systems deployed in natural environments that were not pertinent for the systems designed in the early years of synthetic biology. I propose the term *environmental synthetic biology* to describe these efforts. Here, the term 'environment' does not refer exclusively to natural environments like terrestrial or aquatic ecosystems, but any operational context where the system or its environment are not fully amenable to control or monitoring. I argue that the central challenges of environmental synthetic biology, presented in the following section, are sufficiently distinct from those that occupy conventional synthetic biologists to merit viewing them as a related, but nonetheless distinct, field of study.

1.2 Major research areas in environmental synthetic biology

In this section, I describe some of the core principles underlying environmental synthetic biology. It is important to emphasize that many researchers have previously identified many of these areas as important research directions, and that some of these directions have had a number of key developments already established. However, the notion of collecting these research directions together to serve as as the foundations for a mature, environmentally-motivated subfield of synthetic biology has not been fully explored. In presenting this framework, I hope to promote the formation of new mindsets and angles with which to view existing research questions from a new light, identifying shared challenges and opportunities between otherwise-disparate research areas.

System delivery

This first pillar of environmental synthetic biology is perhaps its most foundational: how does one actually deliver the engineered system to the target environment? Introducing a nonnative strain into a natural environment is a challenging problem because the native microbes, being already adapted to their host environment, are likely to outcompete the introduced strain. The fact that engineered genetic circuits typically convey a metabolic burden to their hosts only exacerbates this problem. Resolving this issue will likely require a multi-pronged approach that takes advantage of both the natural colonization capacities of different host strains as well as the

design of dedicated genetic circuits intended to promote niche establishment and persistence.

Despite the foundational import of this challenge, there has been little work to date from synthetic biologists that specifically addresses this question, particularly for external environments like soil rhizosphere communities. In a recent perspective, de Lorenzo [11] proposes the term *Environmental Galenics* to describe this overarching research space, named after the field of pharmacological science that focuses on the delivery and administration of drugs. de Lorenzo identifies the study of horizontal gene transfer as an area particularly overlooked by synthetic biologists that will likely play an essential role in maintaining the persistence of an engineered genetic circuit within a target environment.

The question of biocontainment is also a major component of system delivery– in addition to making sure the engineered system can colonize and persist in a target environment, synthetic biologists must ensure that the system is not so potent that it extends its intended reach in either space or time. Because synthetic biology devices will be, by nature, genetically modified (GM) organisms, developing effective biocontainment strategies will be critical in enabling their safe deployment while meeting regulatory guidelines for the dissemination of GM organisms.

While synthetic biologists typically address biocontainment challenges through engineering auxotrophies or kill switches into their host strains [12], one area that has been overlooked is the explicitly spatiotemporal characterization and engineering of the persistence and dispersal of both microbes and the DNA they carry in natural environments. Even when DNA vectors are not known to be mobile, they can still persist in the environment in the form of extracellular DNA (eDNA) upon the death of their hosts, and potentially be taken up by native microbes. Understanding the persistence and dispersal dynamics of eDNA in natural environments is still an active research question for environmental microbiologists [13, 14], and therefore provides a fruitful opportunity for collaboration between the two fields to better understand and optimize these dynamics.

Robustness and predictability

Ensuring that the performance of a genetic device is reliable and predictable is a principle that has been long-established in synthetic biology, and is certainly not unique to applications intended for environmental deployment. There are, however, some important nuances associated with device performance natural environments

that will imply some specific subpriorities within this larger goal that have so far not been prioritized.

Early efforts towards establishing predictable performance in synthetic biology focused generally on two forms of insulation. The first is genetic insulation, which tries to ensure that the performance of a genetic part is robust to the nature of the genetic sequences surrounding it [15]. The second is robustness to cellular burden, which recognizes that synthetic genetic devices can draw significantly from the cell's limited pool of gene expression machinery and thereby cause unintended consequences like retroactivity [16, 17]. However, there are more general classes of robustness that will become relevant when these engineered systems move outside of the context of a well-controlled laboratory environment.

First, there is the fact that external environmental parameters can directly influence the function of the biomolecular components that implement the genetic circuits. One such factor is temperature– although temperature is likely to stay relatively constant inside mammalian hosts due to homeostasis, external environments like terrestrial or aquatic habitats will experience significant fluctuations in temperature on both daily and seasonal timescales. Despite the relative ease with which temperature can be manipulated in laboratory settings, its direct impact on the performance of synthetic circuits is rarely studied [18].

Environmental parameters can also influence the performance of genetic circuits indirectly via changing the physiological state of the host cell. The presence of active stressors such as antibiotic compounds or reactive oxygen species, or the absence of beneficial compounds like in nutrient limitation, will all have a significant impact on cells' global gene expression and proteome maintenance properties that will undoubtedly impact the performance of the genetic circuits contained inside. Characterizing part and circuit performance within well-controlled laboratory settings where cells can grow at their maximal growth rate will likely not yield insights that can be directly applied to predict performance in field conditions. Experimental substrates that better-simulate such environmental variables within the controlled context of a laboratory setting will be essential for enabling the reliable performance of engineered biological systems.

Control and monitoring

Synthetic biologists evaluate the performance of their circuits almost exclusively through the use of fluorescent proteins as the final readout. But application envi-

ronments, whether they are inside mammalian hosts or within the soil, are typically optically inaccessible. Even in optically-permeable settings like aquatic habitats, the fact that cells must be sampled and directly interrogated to observe their fluorescence means that it is typically infeasible to continuously monitor the performance of a synthetic biology system after deployment.

A similar issue is raised for the active external control of these systems. Within the laboratory setting, synthetic biologists typically apply chemical inducers to activate the expression of targeted genetic components within the circuit. But whether a given inducer can operate effectively within a natural environment cannot be assumed, as factors that promote its degradation or sorption will compromise its fidelity in carrying a control instruction to the engineered system [19].

It is therefore of great importance to characterize the efficacy of these communication modalities, both from the experimenter to the system and from the system to the experimenter, in the context of various natural environments. It will also be important to develop alternative communication architectures whose properties are optimized for different classes of environments.

Significant progress in this direction has been made in the Shapiro group for the environment of mammalian hosts. By incorporating bacterial gas vesicles as a readout for ultrasound signals, one can 'image' cells deep within intact tissue that would be inaccessible with conventional optical methods due to the scattering of light [20, 21]. Bioelectric interfaces are another major research direction, where cells are deployed alongside miniature electronic systems that can detect cellular responses locally and wirelessly transmit this information to an external receiver [22]. Such systems could also be harnessed to deliver control instructions to the cells, for example via local optogenetic control of gene circuit function [23]. In the context of external environments, the Silberg group has also developed gas-based reporters that can be used to continuously monitor microbial processes within soil environments [24].

More efforts on these fronts, particularly efforts that focus on delivering control instructions to cellular systems, will be an essential part of the continued development of environmental synthetic biology as as mature engineering discipline.

Autonomous operation and error correction

Finally, the inaccessible nature of natural environments means that the autonomous operation of engineered biological systems carries a much greater weight than it

does for conventional applications of synthetic biology. Consider, for example, the notion of catastrophic system failures. In the context of a well-controlled system like a bioreactor, such a failure would be undesirable but could be ameliorated by purging and resetting the system. In the context of a natural environment, however, such resetting is often infeasible, and when the environment itself is a human patient or a native ecosystem, the consequences of this failure could potentially be extremely grave.

It is therefore critical for environmental synthetic biologists to develop rigorous foundations for the reliable and fully-autonomous performance of engineered biological systems, particularly in the context of error correction. Systems designed to actively self-monitor their state to check for errors and remove or correct them are a category of circuit architecture that has not yet been explored by synthetic biologists. This is particularly relevant in the context of the evolutionary stability of circuits, as the unavoidable presence of random genetic mutations will remain an ever-present destabilizing influence on the system's performance.

1.3 Outline of thesis chapters

In the following chapters, I present work from three different projects that touch on the different overarching themes of environmental synthetic biology presented above. Each project presents an alternative framework to the conventional approaches taken by synthetic biologists to their respective areas, and in doing so suggests new research directions that could help enable the continued development of environmental synthetic biology as a whole.

In Chapter 2, I present a new system for intercellular communication in engineered bacterial populations that encodes messages within horizontally-mobile DNA vectors. While DNA-based communication has been described in the past [25], this work is the first communication framework to make use of the fact that the dynamic mutability of DNA allows the message to be modified *in situ* by the cells themselves. In this way, the communicated messages can adapt to the changing needs of the system rather than remaining hard-coded, paving the way towards engineering autonomously adaptable biological systems.

In Chapter 3, I present a new mathematical framework developed jointly with Fangzhou Xiao that enables the analysis of a particular class of biomolecular binding networks in such a way that its behavior under all possible system variations can be tractably represented in a concise geometric object. This greatly improves the predictability of system performance as the influence of environmental factors, even when unknown, are nonetheless still governed by these well-defined constraints. I then present some initial results towards extending the scope of the classes of biomolecular systems that can be analyzed with this approach in Chapter 4.

In Chapter 5, I present some preliminary results from a study of inducible transcriptional response functions under conditions of growth arrest. These initial results form the basis of a library-scale dataset that would provide valuable information about which transcriptional control systems are viable or unviable for use in implementing genetic circuits for applications in environments where cells experience nutrient limitation. Finally, I conclude with some closing remarks on the future of environmental synthetic biology in Chapter 6.

References

[1] Michael B. Elowitz and Stanislas Leibler. "A synthetic oscillatory network of transcriptional regulators". *Nature* 403.6767 (2000), pp. 335–338.

[2] Timothy S. Gardner, Charles R. Cantor, and James J. Collins. "Construction of a genetic toggle switch in Escherichia coli". *Nature* 403.6767 (2000), pp. 339–342.

[3] Reshma P. Shetty, Drew Endy, and Thomas F. Knight. "Engineering BioBrick vectors from BioBrick parts". *Journal of Biological Engineering* 2.1 (2008).

[4] Mark Mimee et al. "Programming a Human Commensal Bacterium, Bacteroides thetaiotaomicron, to Sense and Respond to Stimuli in the Murine Gut Microbiota". *Cell Systems* 1.1 (2015), pp. 62–71.

[5] Weston R. Whitaker, Elizabeth Stanley Shepherd, and Justin L. Sonnenburg. "Tunable Expression Tools Enable Single-Cell Strain Distinction in the Gut Microbiome". *Cell* 169.3 (2017), 538–546.e12.

[6] Pablo I. Nikel and Victor de Lorenzo. "Pseudomonas putida as a functional chassis for industrial biocatalysis: From native biochemistry to trans-metabolism". *Metabolic Engineering* 50 (2018), pp. 142–155.

[7] Bradley W. Biggs et al. "Development of a genetic toolset for the highly engineerable and metabolically versatile Acinetobacter baylyi ADP1". *Nucleic Acids Research* 48.9 (2020), pp. 5169–5182.

[8] Chunbo Lou et al. “Ribozyme-based insulator parts buffer synthetic circuits from genetic context”. *Nature Biotechnology* 30.11 (2012), pp. 1137–1142.

[9] Florian Schmidt et al. “Noninvasive assessment of gut function using transcriptional recording sentinel cells”. *Science* 376.6594 (2022).

[10] Min-Hyung Ryu et al. “Control of nitrogen fixation in bacteria that associate with cereals”. *Nature Microbiology* 5.2 (2019), pp. 314–330.

[11] Victor de Lorenzo. “Environmental Galenics: large-scale fortification of extant microbiomes with engineered bioremediation agents”. *Philosophical Transactions of the Royal Society B: Biological Sciences* 377.1857 (2022).

[12] Finn Stirling and Pamela A. Silver. “Controlling the Implementation of Transgenic Microbes: Are We Ready for What Synthetic Biology Has to Offer?” *Molecular Cell* 78.4 (2020), pp. 614–623.

[13] Sara Hope Sirois and Daniel H. Buckley. “Factors governing extracellular DNA degradation dynamics in soil”. *Environmental Microbiology Reports* 11.2 (2018), pp. 173–184.

[14] Heather A. Kittredge, Kevin M. Dougherty, and Sarah E. Evans. “Dead but Not Forgotten: How Extracellular DNA, Moisture, and Space Modulate the Horizontal Transfer of Extracellular Antibiotic Resistance Genes in Soil”. *Applied and Environmental Microbiology* 88.7 (2022).

[15] Enoch Yeung et al. “Biophysical Constraints Arising from Compositional Context in Synthetic Gene Networks”. *Cell Systems* 5.1 (2017), 11–24.e12.

[16] Domitilla Del Vecchio, Alexander J. Ninfa, and Eduardo D. Sontag. “Modular cell biology: retroactivity and insulation”. *Molecular Systems Biology* 4.1 (2008), p. 161.

[17] Francesca Ceroni et al. “Burden-driven feedback control of gene expression”. *Nature Methods* 15.5 (2018), pp. 387–393.

[18] Abhilash Patel, Richard M. Murray, and Shaunak Sen. “Assessment of Robustness to Temperature in a Negative Feedback Loop and a Feedforward Loop”. *ACS Synthetic Biology* 9.7 (2020), pp. 1581–1590.

[19] Ilenne Del Valle et al. “Artificial soils reveal individual factor controls on microbial processes”. *Msystems* 7.4 (2022), e00301–22.

[20] Raymond W. Bourdeau et al. “Acoustic reporter genes for noninvasive imaging of microorganisms in mammalian hosts”. *Nature* 553.7686 (2018), pp. 86–90.

[21] Jerzy O. Szablowski et al. “Acoustically targeted chemogenetics for the non-invasive control of neural circuits”. *Nature Biomedical Engineering* 2.7 (2018), pp. 475–484.

[22] Mark Mimee et al. “An ingestible bacterial-electronic system to monitor gastrointestinal health”. *Science* 360.6391 (2018), pp. 915–918.

[23] Sant Kumar and Mustafa Khammash. “Platforms for Optogenetic Stimulation and Feedback Control”. *Frontiers in Bioengineering and Biotechnology* 10 (2022).

[24] Hsiao-Ying Cheng et al. “Ratiometric Gas Reporting: A Nondisruptive Approach To Monitor Gene Expression in Soils”. *ACS Synthetic Biology* 7.3 (2018), pp. 903–911.

[25] Monica E. Ortiz and Drew Endy. “Engineered cell-cell communication via DNA messaging”. *Journal of Biological Engineering* 6.1 (2012), pp. 1–12.

Chapter 2

ADDRESSABLE AND ADAPTABLE INTERCELLULAR COMMUNICATION VIA DNA MESSAGING

The contents of this chapter are reproduced, with some narrative changes to the Introduction and some editorial changes throughout, from

> John P. Marken and Richard M. Murray. "Addressable and adaptable intercellular communication via DNA messaging". *Nature Communications* (2023). DOI: 10.1038/s41467-023-37788-z.
> J.P.M. conceived and designed the project, performed the experiments, analyzed the data, and wrote the manuscript.

2.1 Introduction

A major current focus of synthetic biology research is to expand beyond the field's original paradigm of engineering a single cell strain for a particular application and to instead engineer consortia, which are populations consisting of multiple distinct cell types [1, 2]. By enabling the division of labor among its constituent strains, a consortia-based approach allows each strain to specialize itself to its assigned task while minimizing the metabolic burden to itself [3]. Engineered consortia are therefore able to achieve higher levels of functional complexity [4–6] and evolutionary stability [7, 8] than analogous single-strain systems.

In order for an engineered consortium to function properly, however, it is necessary that each of its constituent strains can stably coexist and act in concert with each other. This coordinated activity is maintained by intercellular communication systems that allow the strains to dynamically instruct each other to perform programmed functions, like modulating their growth rate or activating a target gene. The achievable complexity of a consortium's behavior is therefore constrained by the capacity of its communication channels to transmit complex messages [6]. Realizing this, the synthetic biology community has placed much effort towards expanding the toolbox of intercellular communication channels and enabling increasingly information-dense communication between cells [9–15].

These efforts have almost exclusively focused on a molecular architecture that we will term Small Molecule Actuated communication (SMA communication), wherein

a sender cell synthesizes a small molecule that diffuses through the extracellular environment to enter a receiver cell that contains the requisite machinery to initiate a preprogrammed response to the signal. SMA communication channels were originally implemented using molecular parts co-opted from quorum sensing systems [9], but in recent years the toolbox has expanded to include metabolites [10], hormones [13], and antibiotics [16, 17] as signal vectors.

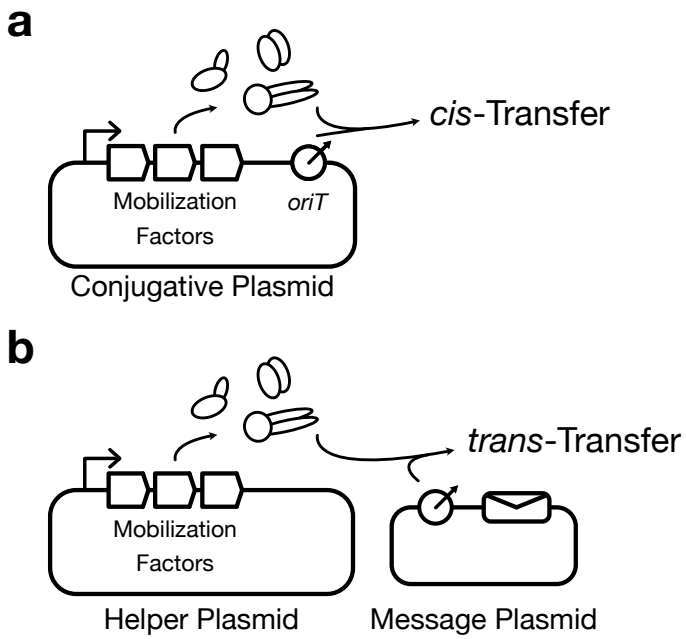

Figure 2.1: How natural horizontal gene transfer systems are converted into DNA messaging channels. (a) Schematic of the architecture of a natural horizontal gene transfer system, using a conjugative plasmid as an example. The mobile vector expresses a set of genes, collectively called the mobilization factors, that transfer DNA elements that contain a cognate recognition sequence called the origin of transfer (*oriT*). Because the conjugative plasmid itself contains an *oriT* site, it transfers itself in a process termed *cis*-transfer. (b) Schematic of the architecture of a DNA messaging channel. The *oriT* is removed from the conjugative plasmid to create a helper plasmid that confers the ability to transfer DNA to its host cell but cannot transfer itself. The cognate *oriT* sequence can be placed onto another DNA vector to create a DNA message, which can then be transferred to another cell via the mobilization factors expressed by the helper plasmid. This process is called *trans*-transfer. Other horizontal gene transfer mechanisms, like non-lytic bacteriophages, share this same fundamental architecture and can be converted into DNA messaging channels through this same process.

In these SMA communication channels, the information content of the message is encoded in the concentration of the signal compound. Because the response

modules for these signals are typically switchlike, if the concentration of the signal crosses the detection threshold then the receiver cell responds fully and does not respond otherwise. These response systems, particularly those from quorum sensing systems, tend to require an appreciable concentration of signal compound to trigger in order to avoid spurious activation [18]. Ensuring that the sender cells produce enough signal compound to cross this threshold is therefore an integral part of maintaining information integrity in SMA systems.

However, when the consortia relying on these SMA channels are deployed in environmental settings, external factors can influence the effective concentration of signal compound that the cells perceive. Experiments in artificial soils, for example, have demonstrated that altering environmental parameters such as soil particle size and the presence of organic matter can impact the bioavailability of homoserine lactones by up to three orders of magnitude [19]. Sender cells designed to synthesize a signal compound at a particular concentration might therefore find that a message intended to encode an ON signal could be interpreted by the receivers as an OFF signal depending on the current state of the environment.

Such an issue could be avoided if the information content of the message were encoded into the molecular identity of the signal substrate itself. An alternative communication architecture that takes this approach, DNA messaging, was proposed in a pioneering report by Ortiz and Endy [14]. Here, horizontal gene transfer mechanisms are co-opted into a communication channel that transmits DNA-encoded messages between cells (Figure 2.1). Because the actual content of the message is an arbitrary genetic sequence within the mobile vector itself, Ortiz and Endy coined the term "message-channel decoupling" to describe the fact that a single DNA-based communication channel can send different messages that contain different types of instructions to the recipient cells [14]. In contrast, SMA communication channels exhibit message-channel coupling because the nature of the encodable message is tied to the molecular identity of the signaling molecule. A homoserine lactone, for example, can only be used to encode the instruction to activate its cognate transcription factor, and an antibiotic can only be used to encode the instruction to kill its susceptible cell strains (Figure 2.2a).

A second important advantage of DNA communication is that a single DNA message can encode a large amount of information content, as many horizontal gene transfer systems can easily transfer several kilobases of arbitrary sequence [20–22]. In contrast, SMA channels can only modulate their activity via the concentration of

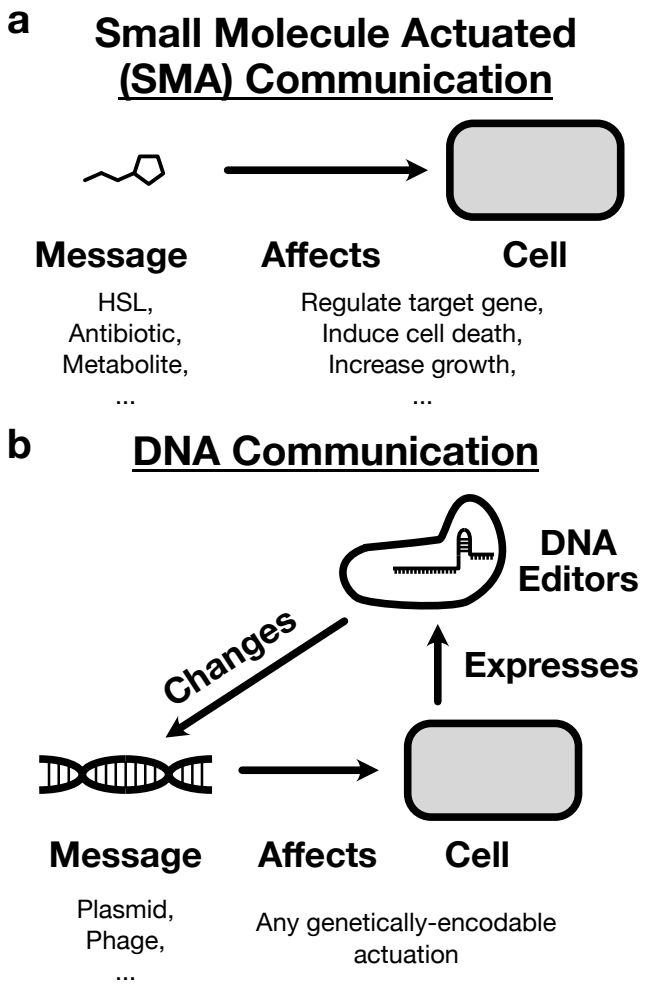

Figure 2.2: Architectures for engineered intercellular communication. (a) Small Molecule Actuated (SMA) communication systems exhibit message-channel coupling, meaning that the behavior they induce in the receiver cell is hard-coded into the molecular identity of the signaling molecule itself. This molecular identity cannot be changed without disrupting the functioning of the channel itself. (b) DNA communication systems exhibit message-channel decoupling, meaning that a given channel can transmit multiple types of messages to induce any genetically-encodable response in the receiver cell. Furthermore, the cells themselves can express molecular DNA editors to change the content of the messages *in situ*, closing the loop to enable autonomous system reconfiguration.

their signal vector, a single small molecule. This heavily constrains the information density of the message, to the point where in applications like digital computation where concentrations are interpreted binarily as either OFF or ON, a single SMA channel can only transmit a single bit of information [23].

Together, these advantages suggest that DNA messaging is an ideal communication architecture for engineering complex consortia with sophisticated information processing requirements in variable environments. But although the ten years since the Ortiz-Endy report have seen an increased use of horizontal gene transfer systems by synthetic biologists to engineer environmental microbiomes in the gut or soil [24–26], further studies of such systems' ability to act specifically as a communication framework for engineered consortia have only been performed computationally [27–29]. Thus, to our knowledge, the original Ortiz-Endy report remains the only experimental usage of DNA-based communication to date.

Why is this the case? One reason is that, though it was pioneering in its foresight, the Ortiz-Endy implementation did not demonstrate a third property of DNA communication that is critical in enabling the implementation of qualitatively new functionalities— the dynamic mutability of DNA messages. Unlike SMA channels, where the message is encoded into the structure of an immutable signal molecule, cells have the ability to express DNA editors that can make targeted changes to the content of the message *in situ* (Figure 2.2b). This ability has only expanded with the recent explosion in research on programmable DNA editors like CRISPR-Cas systems, integrases, and base editors [30, 31]. Although theoretical reports have rightly identified mutability as a key advantage of DNA messaging [27], to date this property has not been experimentally demonstrated.

We therefore set out to develop a general and scalable architecture for DNA messaging that allows users to fully take advantage of all three of its unique properties: message-channel decoupling, high information density, and dynamic message mutability. In order to ensure our framework's compatibility with arbitrary messages transferred along arbitrary horizontal gene transfer systems, we used channel-orthogonal molecular tools to implement a functionality that is required in all communication systems— the ability to address the message to a targeted set of recipients.

Our addressing framework uses CRISPR-Cas systems to internally validate each message transfer event within the consortium, enabling the targeted delivery of a given message to any subset of the strains in a population. We additionally design a

framework for using integrases to modularly update messages' recipient lists *in situ*, enabling the control of information flow through a population. This work establishes a universally-applicable framework for effective DNA-based communication that sets the stage for future efforts that expand its ability to implement previously-inaccessible functionalities into engineered consortia.

2.2 Results

Incorporating message addressability into a plasmid conjugation-based communication system

We first describe the implementation of an addressability system for our DNA messaging framework. Any such implementation requires a means for the molecular recognition of specific genetic sequences, and we chose to use the CRISPR-Cas adaptive immunity system due to its ability to programmatically target and cleave desired nucleotide sequences on genetic vectors entering the cell [32, 33]. Although multiple different Cas systems have been demonstrated to cleave and degrade DNA vectors within cells [34, 35], we specifically chose to use the *S. pyogenes* Cas9 endonuclease system because it contains the required binding, unwinding, and cleaving activities within a single protein, facilitating its use in many different host organisms [36]. Additionally, well-developed procedures exist for generating large libraries of orthogonal single-guide RNAs (gRNAs) for the Cas9 system [15, 37, 38], and the small footprint of the gRNA binding site (23 bp) means that many such sites can be incorporated onto a DNA message without significantly burdening any potential sequence length constraints from the transfer system. Together, these properties make the Cas9-gRNA system an ideal candidate for implementing a scalable, modular, and host-orthogonal addressing system for DNA messaging.

The design of our addressability framework is as follows. Each receiver cell in the consortium expresses both Cas9 and a unique gRNA that serves as a molecular signature encoding its strain identity. The sender cells themselves require no additional molecular machinery, but the DNA message must contain an array of gRNA binding sites that correspond to the receiver strains that should not receive the message. We will refer to this array as the address region because it acts as a blocklist, encoding the recipient list of the message as the set of strains whose gRNAs are not encoded in the address (Figure 2.3a). When the message is transferred to a receiver cell, the Cas9-gRNA complex checks the validity of the transfer— if the transfer is invalid, then the complex will bind to the cognate site on the address region and cleave the message, leading to its degradation. If the transfer is valid, then the Cas9-gRNA

complex is unable to interact with the message, and so the message freely propagates within the receiver cell. This process is schematized in Figure 2.3b.

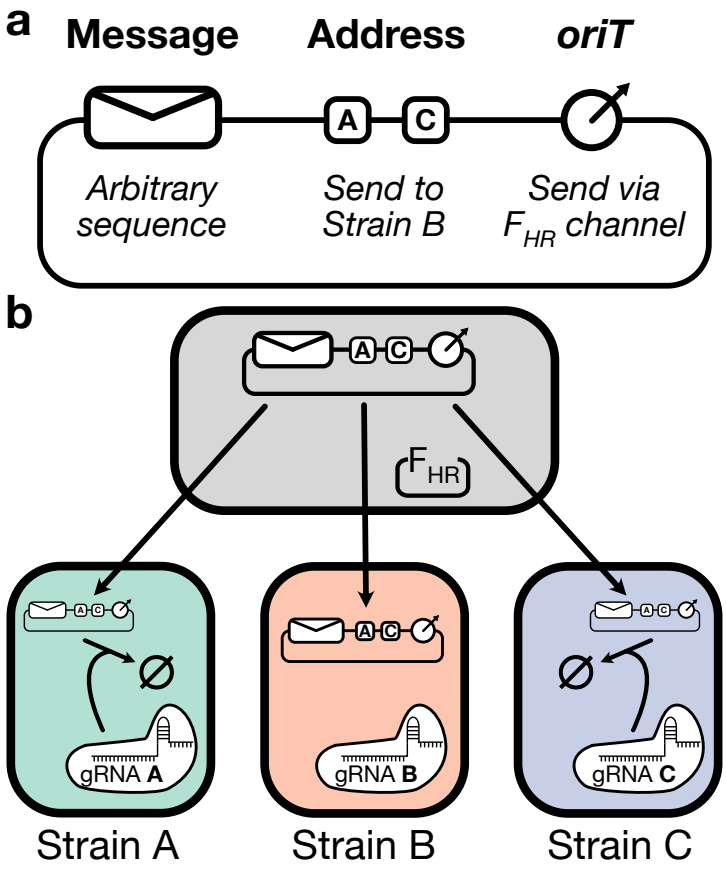

Figure 2.3: Addressable DNA messaging. (a) Schematic of an addressable DNA message. The content of the message is an arbitrary genetic sequence, and the address region uses gRNA binding sites to act as a blocklist that determines the message's recipient list by excluding transfer to all encoded strains. The origin of transfer (*oriT*) allows the message to interact with the cognate horizontal gene transfer machinery in the sender cell. (b) Schematic of transfer blocking. The DNA message is initially transferred promiscuously to all receiver strains in the population. As the message enters a receiver cell, the binding sites on the address region become exposed to cleavage by the Cas9-gRNA complex expressed within the cell. This cleavage only occurs if a binding site on the address matches the gRNA expressed in the receiver cell, thus ensuring that the message only persists within its appropriate recipients by eliminating the messages sent to invalid recipients.

An important property of this addressing framework is that the transfer validation system interacts with the message itself, rather than the transfer machinery that carries the message. This means that a single DNA channel can send messages that are addressed to different recipients. When addressability is implemented via

channel-intrinsic properties, such as in the Ortiz-Endy system's reliance on the M13 bacteriophage's narrow infection host range [14], every message that is transmitted by a channel must go to the same recipient list regardless of its content.

In demonstrating the incorporation of our message addressing framework into a DNA-based communication system, we chose to deviate from Ortiz and Endy's original choice of the filamentous bateriophage M13 and instead used a plasmid conjugation-based communication system. This is because the properties of plasmid conjugation systems are better-aligned with the advantages of DNA-based communication as a whole— plasmids can encode larger messages, with conjugative plasmids regularly reaching lengths of hundreds of kilobases [22, 39], and can transfer to taxonomically-diverse recipients [40, 41], facilitating their use in multispecies consortia. We specifically chose to use the F_{HR} system developed by Dimitriu et al. [20], which is based on the *E. coli* fertility factor F, the canonical representative of conjugative plasmids [42].

Cas9-mediated blocking of plasmid receipt is inducible and orthogonal

In order to demonstrate that Cas9-mediated cleavage can indeed block the receipt of a mobilized plasmid, we performed pairwise sender-receiver experiments in *E. coli* consortia using the F_{HR} -based communication system. Receiver cells containing a genomically-integrated spectinomycin resistance cassette were transformed with a plasmid encoding OHC14-HSL-inducible expression of Cas9 and one of two gRNAs ("A" or "B"), and sender cells containing a genomically-integrated apramycin resistance cassette were transformed with the F_{HR} helper plasmid and a pSC101 message plasmid that constitutively expresses a yellow fluorescent protein and chloramphenicol resistance gene. Two variants of this message plasmid were constructed, differing in whether their address region contained a single A binding site or a single B binding site (Figure 2.4a).

With this setup, selective plating could be used to individually isolate the senders, receivers, and transconjugants from a mixed population and calculate their densities. We performed mating experiments on all four combinations of sender-receiver pairs in the presence and absence of OHC14-HSL induction and measured the densities of each strain after 6 hours of growth in a shaken LB coculture (Figure 2.4b). The message plasmid was transferred efficiently to the receivers in this timeframe, with an average of 64% of receivers being converted to transconjugants across all transfers to on-target recipients (Figure 2.5).

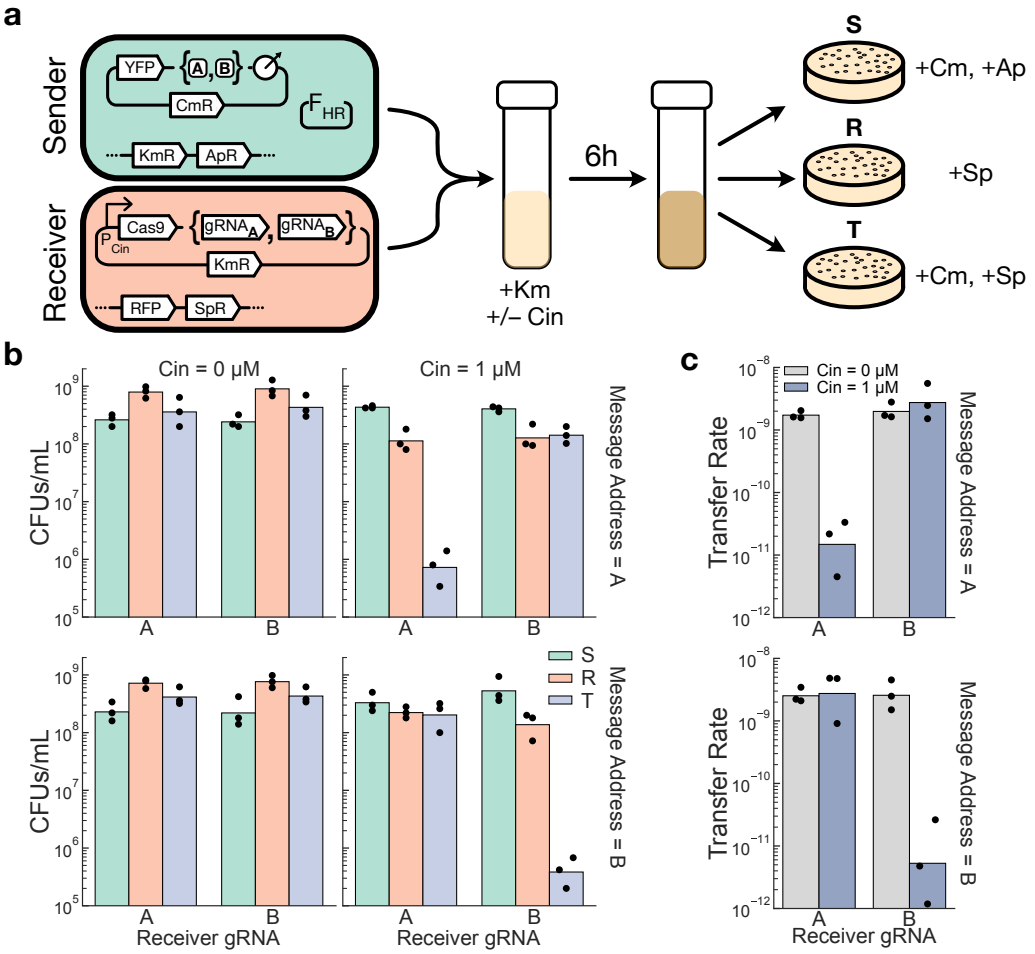

Figure 2.4: Cas9-mediated cleavage of incoming plasmids can bias their transfer to targeted recipients. (a) Schematic of the experimental setup. Senders (S) and Receivers (R) carrying one of two plasmid variants are grown together in a coculture and selective plating is used to isolate them, as well as the transconjugants (T), from the mixed culture. Note that transconjugants will appear on the receiver-selecting plates so R is the total density of receivers in the population (Methods). (b) Endpoint strain densities, measured in colony forming units (CFUs) per mL of culture. (c) Transfer rates, calculated as $T/(S * R)$, of the message plasmid in each of the conditions in (b). Dots show the values from three biological replicates measured on different days, and bars depict the geometric mean of these values. Km = kanamycin, Cm = chloramphenicol, Ap = apramycin, Sp = spectinomycin, Cin = OHC14-HSL.

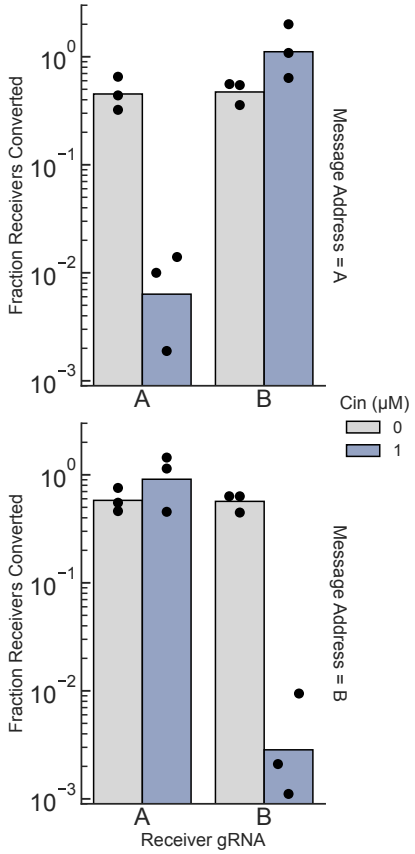

Figure 2.5: Fractional receiver conversion of the experiments from Figure 2.4. Dots represent T/R values for each of three biological replicates measured on different days, calculated from the data shown in Figure 2.4b. Bars represent the geometric mean of the replicates.

We then quantified the effectiveness of Cas9-mediated plasmid blocking by calculating the plasmid transfer rate in each experiment, defined as the transconjugant density divided by the product of the total sender and total receiver densities. We observed that when the Cas9 system was induced, the A-containing message plasmid had a 185-fold higher transfer rate to its valid recipient (the B receiver) than to its invalid recipient (the A receiver) (p = 0.03, paired t test), and that for the B-containing message plasmid the difference was 520-fold (p = 0.01, paired t test) (Figure 2.4c). When the Cas9 system was not induced in the receiver cells, this biased transfer was not observed (p = 0.28, 0.94, paired t test, for A and B message plasmids respectively) (Figure 2.4c).

Having demonstrated that our addressability system performed successfully in a two-strain population, we next asked whether our system could scale to multi-

strain populations where a given address region may need to encode several gRNA binding sites. We constructed three different receiver strains that, in addition to the spectinomycin resistance gene, each express a distinct fluorescent protein (mScarlet-I [43], sfYFP [44], or TagBFP [45]) from a genomically-integrated cassette. In this way, all three receivers could be mixed together with the sender strain in a four-strain coculture and the colors could be used to determine the density of each distinct receiver strain after selective plating. In order to further assess the generality of our Cas9-mediated blocking system, we used a set of orthogonal gRNAs developed by Didovyk et al. [37] instead of reusing the A and B gRNAs from the previous experiment. We transformed each of the colored receiver strains with a plasmid encoding Cas9 and one of three of the Didovyk gRNAs (D1, D2, or D3), and constructed sender strains containing one of eight message plasmids addressed to every possible combination of the three receiver strains (Figure 2.6a).

We found that even in the more complex setting of a four-strain population, our system was able to preferentially deliver the message to its appropriate recipients. Across all transfers to on-target recipients, the average fraction of receiver cells converted to transconjugants was 60%, and the fold change in transfer rate between valid and invalid recipients was often over 1000-fold (Figure 2.6b; Figure 2.7) Although the three gRNAs used in the receivers were previously reported to be of comparable effectiveness in a dCas9-mediated transcriptional repression assay [37], the D1 and D2 gRNAs were able to block invalid transfers much more strongly than the D3 gRNA— the geometric mean of the fold change in transfer rates between valid and invalid recipients across all conditions where the invalid recipients expressed the D3 gRNA was 79-fold, compared to 1256-fold and 1577-fold for the D1 and D2 gRNAs, respectively (Figure 2.7).

Cells can use integrases to edit DNA messages *in situ* and update their recipient list

Having demonstrated that our Cas9-mediated blocking system can successfully implement high-fidelity addressable communication between cells, we next proceeded to incorporate adaptability into the message transmission framework by enabling the programmable *in situ* editing of a message's recipient list. This can be accomplished by applying molecular DNA editors to modify the gRNA binding sites on the address region. Specifically, a system for programmable address editing should have the ability to both add a new binding site to the array and remove (or invalidate) an existing binding site from the array.

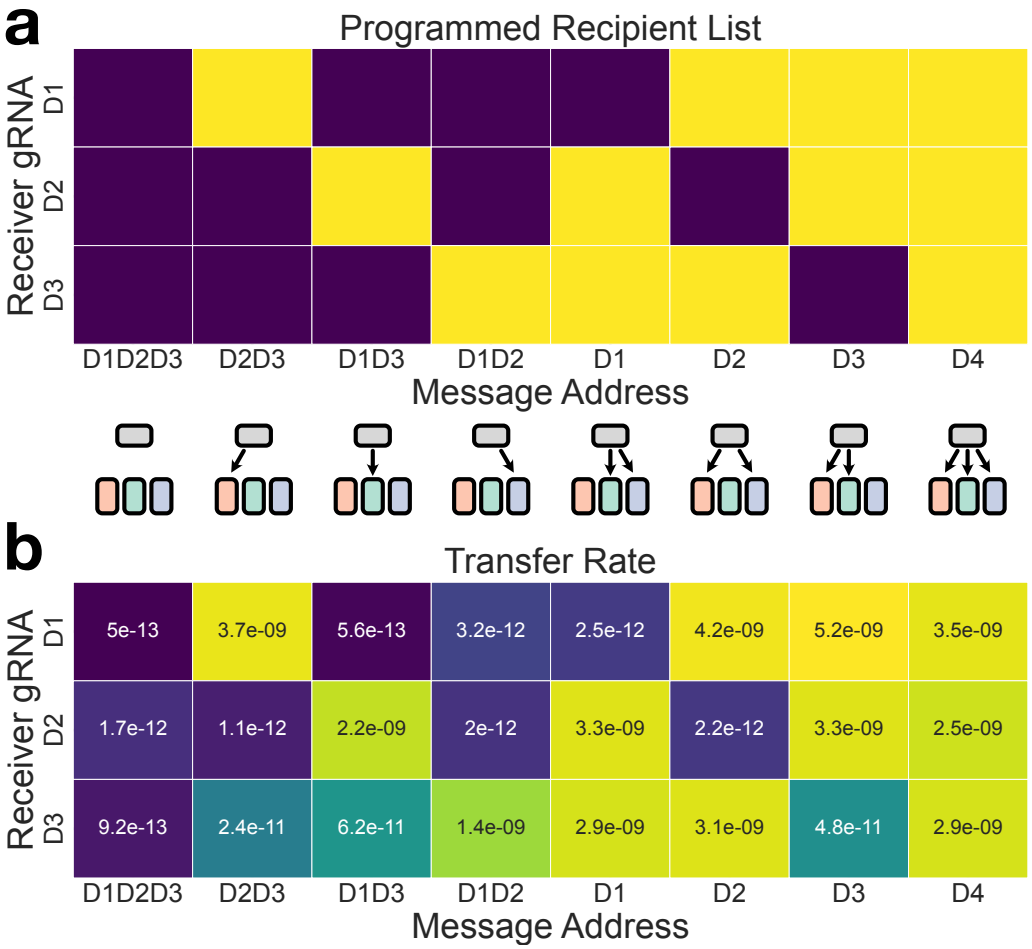

Figure 2.6: Programmable delivery of message plasmids to arbitrary subsets of a multi-strain population. (a) Schematic representation of the intended recipient list for each of the eight message plasmids. Dark squares indicate an invalid transfer and light squares indicate a valid transfer. (b) The observed geometric mean of the transfer rates to each receiver type, calculated from three biological replicates measured on different days. The color map is scaled logarithmically over four orders of magnitude. Individual transfer rate values are shown in Figure 2.7.

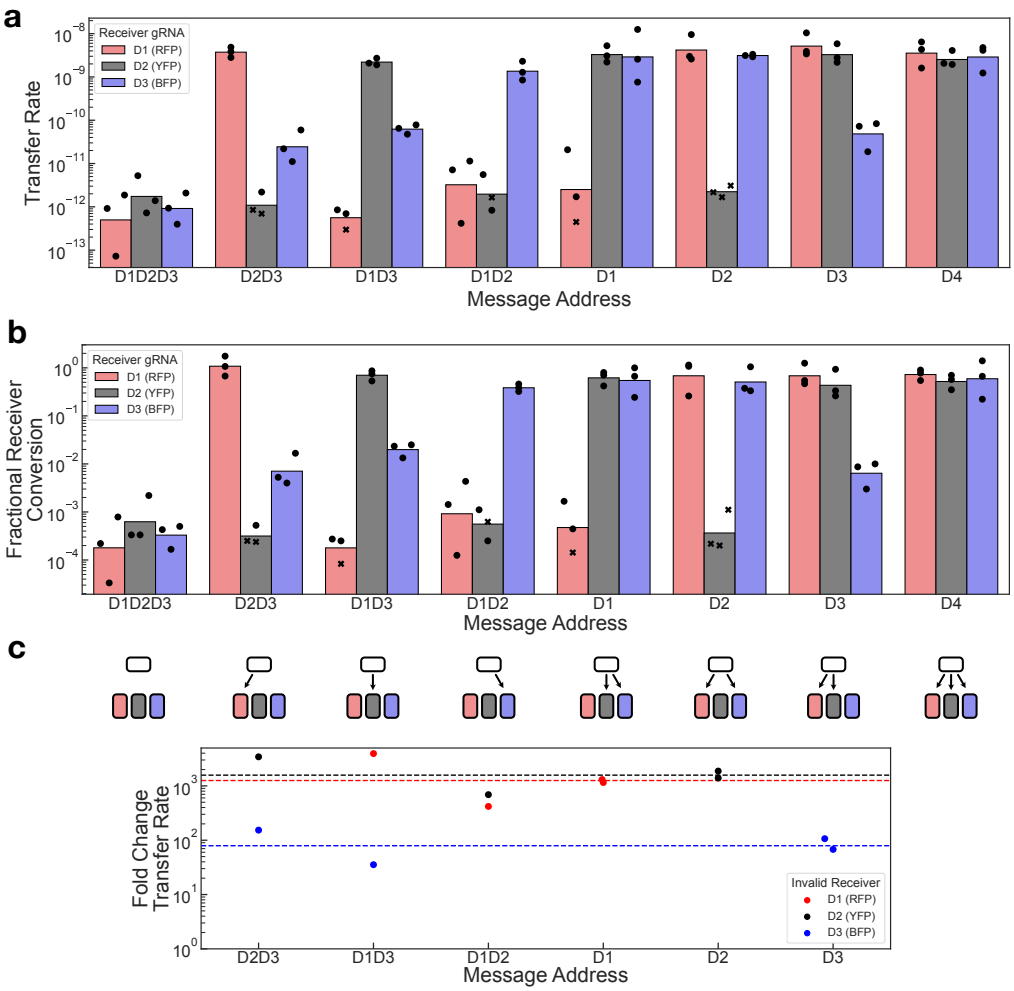

Figure 2.7: Additional data from Figure 2.6. (a) Transfer rate values and (b) Fractional receiver conversion values from the experimental conditions shown in Figure 2.6b. Dots represent the values from each of three biological replicates measured on different days, and bars represent the geometric mean of these replicates. The value of the bars in (a) are identical to those plotted in the heatmap in Figure 2.6b. (c) Fold changes in the geometric means of the transfer rates between valid and invalid recipients for each message plasmid, based on the data in (a). For each message plasmid displayed on the horizontal axis, each dot represents one of the two possible choices of pairwise comparisons between a valid-receiver transfer rate and an invalid-receiver transfer rate. For the message plasmids with two binding sites, the single valid recipient is compared against the two possible invalid recipients, while for the message plasmids with one binding site, the two possible valid recipients are compared against the single invalid recipient. Each dot is colored by the identity of the invalid recipient in the comparison, and dashed lines represent the geometric mean across all of the fold change values where the recipient participated as the invalid comparison.

Serine integrases are a class of proteins that are well-suited for this task because of their ability to bind to specific attachment sequences and add, remove, or swap the regions between these sites depending on their configuration and orientation along the DNA [46, 47]. Their efficiency and programmability have made their use ubiquitous among both molecular and synthetic biologists, and large sets of diverse and orthogonal integrases have been characterized [48, 49].

We implemented address editing by flanking each binding site on the address region with orthogonal integrase attachment sites, in such a way that the expression of the cognate integrase will swap the binding site with a different binding site contained on a separate non-mobile plasmid via a process called recombinase-mediated cassette exchange [50] (Figure 2.8a). This procedure leaves the rest of the message, including the other binding sites on the address region, unaffected.

An important property of this address editing system is that it can be executed unilaterally by the sender cell, such that a message's recipient list can be updated without any coordination with the receivers themselves. This feature is once again only possible because our framework encodes a message's recipient list on the message itself, rather than relying on channel-specific interactions between the message vector and the recipient cell.

To assess the efficacy of our address editing system, we constructed a single sender strain that contains a nonmobilizable plasmid encoding a salicylate-inducible TP901 integrase expression cassette and the B gRNA binding site flanked by TP901 attB sites, alongside a message plasmid containing the A binding site flanked by TP901 attP sites in its address region. We then performed pairwise sender-receiver mating experiments to each of the two A- or B-expressing receiver strains from the original pairwise addressing experiments (Figure 2.4), with the blocking system induced, in the presence or absence of salicylate induction (Figure 2.8b). Following expectations, transfer of the message to the A receiver was blocked 138-fold in the absence of integrase activity ($p = 0.03$, paired t test) while the blocking profile was reversed when the integrase was induced, with the transfer to the B receiver now being blocked by 75 fold ($p = 0.01$, paired t test) (Figure 2.8c).

Although the integrase system was successfully able to bias the transfer of the message plasmid to its intended recipient, we noticed that the overall efficiency of the transfer was lower, with an average receiver conversion of 30% in the pre-edit unblocked transfer dropping to 4.4% in the post-edit unblocked transfer (Figure 2.9a). In order to determine whether this decrease was due to a change in strain growth

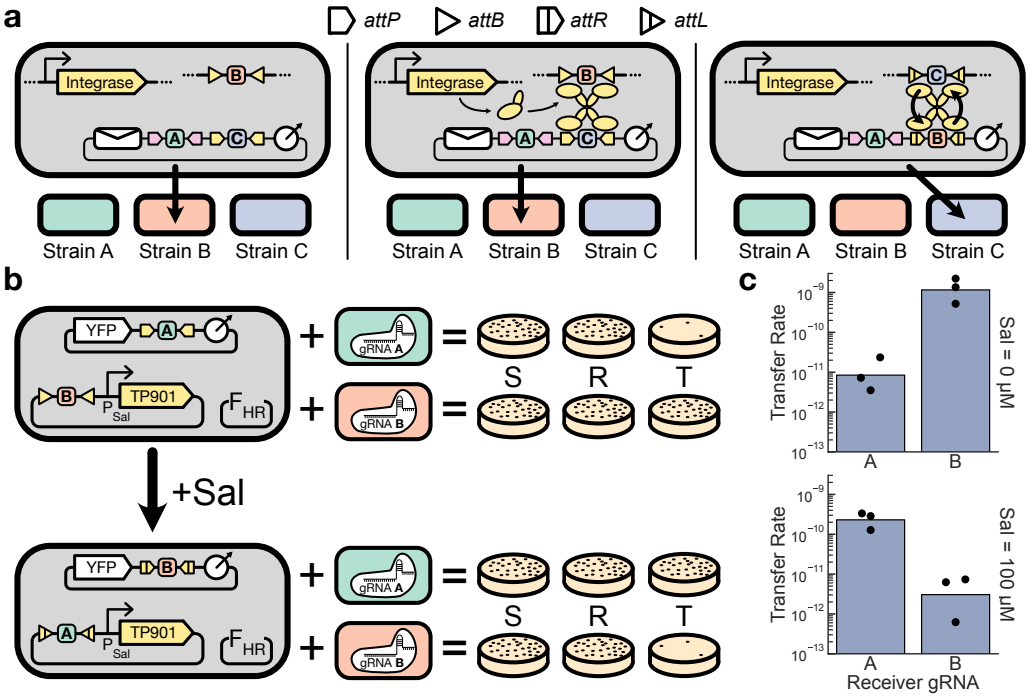

Figure 2.8: Integrase-mediated address editing. (a) Schematic of the process. In the left panel, expression of the integrase has not been induced and no editing has occurred. The message is addressed to Strain B. Orthogonal integrase attachment sites flank each binding site on the address region. In the middle panel, the integrase associated with the C site on the address region has been induced. The corresponding attachment sites for this integrase are also encoded separately on a sequence distinct from the message plasmid. In the right panel, the cassette exchange process has been completed, and the C site on the address region has been swapped with a B site, updating the message's recipient list to Strain C. The process is unidirectional as it converts the attB and attP sites into attL and attR sites that can no longer undergo exchange, making this change permanent unless the cognate reverse directionality factors are expressed to reverse the process and restore the original sequence configuration [47]. (b) Experimental schematic. A single sender strain containing an address-editable message plasmid is coupled with one of two receiver strains in pairwise transfer experiments. Prior to editing, the message is addressed only to the B receiver, but after editing, the message is addressed only to the A receiver. (c) Measured transfer rate from the experiment described in (b). Dots show the values from three biological replicates measured on different days, and bars depict the geometric mean of these values. Sal = salicylate.

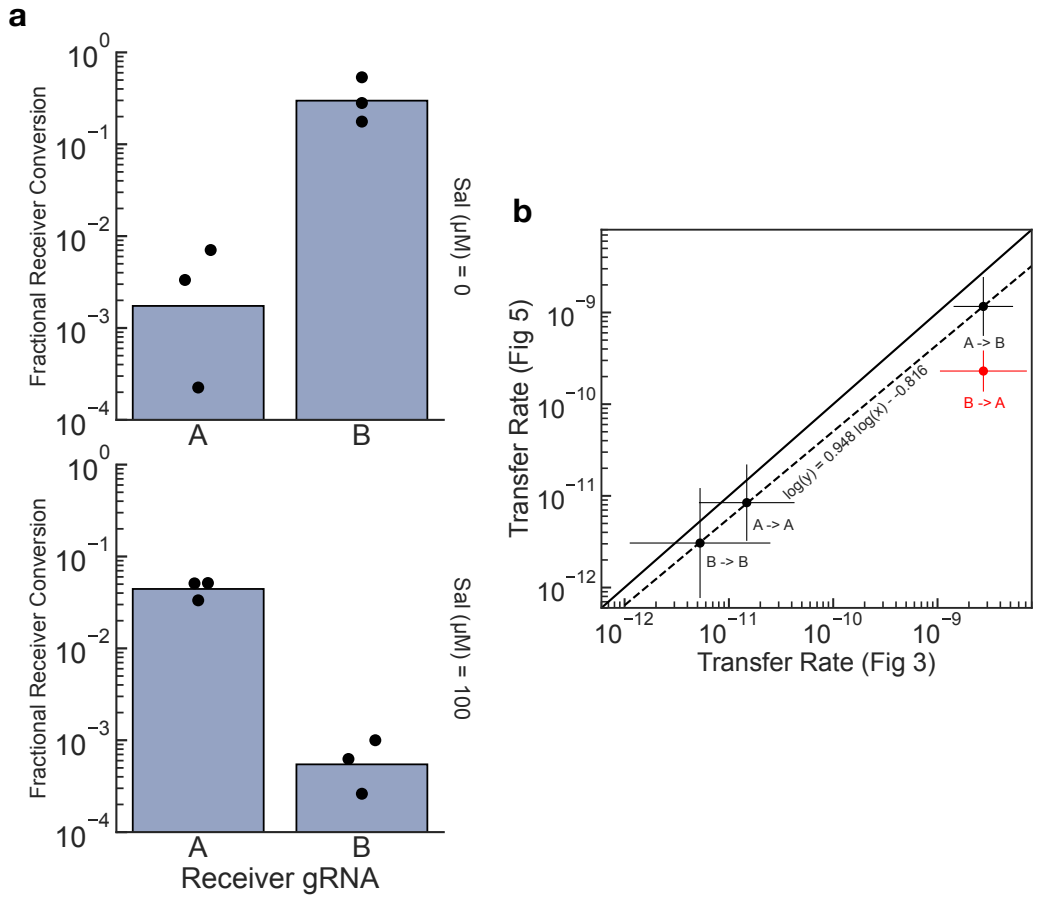

Figure 2.9: Additional data from Figure 2.8. (a) Fractional receiver conversion values from Figure 2.8. Bars represent the geometric mean of the three biological replicates. (b) Plotting transfer rates from Figure 2.4 against those from Figure 2.8. Dots represent the geometric mean and error bars show one geometric standard deviation of the three biological replicates from each experiment. The solid line shows a direct log-linear relationship $\log(y) = \log(x)$, while the dotted line is the result of a log-linear fit to the three black points. The vertical distance between the solid line and each of the black points, indicating the global drop in transfer rate in the Figure 2.8 experiments, is (from left to right) 1.7, 1.8, and 2.4-fold (mean 2.0-fold). The vertical distance between the red point and the dotted line, indicating the additional drop in transfer rate for the post-edit on-target transfer, is 5.1-fold.

dynamics or a change in the intrinsic transfer rate of the plasmid, we compared the transfer rates from the above experiment with the original pairwise transfer blocking experiments in Figure 2.4. We found that these data were nearly directly log-linearly related with the values obtained in the address editing experiment in all conditions except for the post-edit valid transfer (Figure 2.9b) This suggests that there was a global 2-fold decrease in the transfer rate of the Figure 2.8 experiments compared to the Figure 2.4 experiments that was further exacerbated by an additional 5-fold drop in the post-edit on-target transfer. It is therefore prudent to note that the integrase-mediated address editing process can reduce the transfer rate to the new recipients, and mitigating this effect will be an important part of future optimizations of this DNA messaging system.

Address editing enables control of information flow through a population

Having demonstrated that integrase-mediated cassette exchange can successfully edit the address region of a message plasmid to bias its transfer towards new recipients, we next used address editing to implement a proof-of-concept demonstration of controlled information flow through a population. Such control involves not only the selection of specific recipients for a message, as has already been demonstrated, but also the enforcing of a defined order for visiting these recipients. Enforced ordering is an essential part of coordinating multi-step processes, and its implementability is therefore a desirable property for intercellular communication systems.

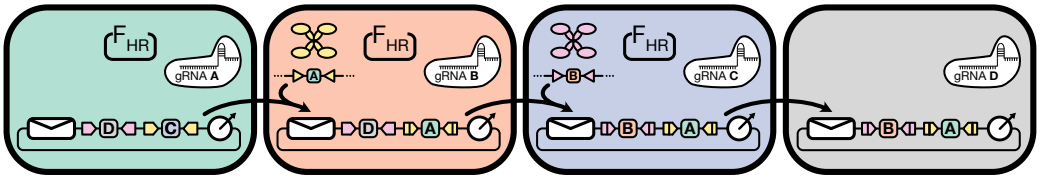

Figure 2.10: Schematic of a four-strain linear relay. This architecture is preserved for any $n \geq 4$. Each strain in the population expresses one of n orthogonal gRNAs, and the address region on the message plasmid contains $n - 2$ binding sites that block its transfer to all strains except its current strain and the next strain in the relay. Each site on the address is flanked by one of $n - 2$ orthogonal integrase attachment site pairs. All strains except the last strain in the relay contain the F_{HR} plasmid, and all strains except the first and last strains express a unique integrase that performs an address editing operation that invalidates the previous strain while validating the next strain in the sequence. Blocked transfers and intermediate message plasmid states are omitted from the diagram.

Specifically, we designed a linear message relay that forces the message to propagate in a linear sequence along a defined order of strains in a consortium, without skipping ahead or backtracking. This sequential order is enforced by ensuring the message plasmid is only addressed to the next strain in the sequence at any given time, which can be implemented by having each successive strain edit the message's address accordingly. An important but subtle property of this system is that the entire signal relay is implemented using a single communication channel that modifies its message at each step. Implementing a similar signal relay with SMA channels would require $n - 1$ orthogonal channels for an n-strain population, while the DNA-based implementation requires only a single channel regardless of the complexity of the consortium composition (Figure 2.10)

We designed the strains for a three-strain linear relay, as described in Figure 2.11a—Strain 1 contains F_{HR} and the message plasmid (initially addressed only to Strain 2) as well as the B gRNA, while Strain 2 contains F_{HR} and the machinery to edit the message plasmid, when received, to address only Strain 3. Strain 3 itself simply expresses the A gRNA. A unique antibiotic resistance gene was genomically integrated into each strain (gentamicin, apramycin, and spectinomycin, respectively) to enable its selective isolation. We then mixed the three strains together and cocultured them for 6 hours before selectively plating out each strain (three parent strains and two possible transconjugant strains) to measure their densities in the endpoint population state.

Because Strain 3's transconjugants (T3) cannot appear until Strain 2's transconjugants (T2) appear, we anticipated that the final endpoint density of T3 should be lower than that of T2. We observed that the average endpoint density of T3 was indeed 3-fold lower than that of T2, although not significantly so ($p = 0.09$, paired t test). This effect emerged despite the fact that the average density of the T3 parent strain (Strain 3) was 5-fold higher than that of the T2 parent strain (Strain 2) ($p = 0.02$, paired t test) (Figure 2.11b). In general, the slow growth of the sender strains contributed to very low receiver conversion rates within the 6 hour window (1.6% conversion of Strain 2 and 0.1% conversion of Strain 3), but these could be mitigated by designing the strains to have similar growth dynamics.

To further validate our system's ability to enforce the sequentially-ordered transmission of its message, we performed a timecourse assay for one of our replicates where we plated out the coculture every hour after the initial mixing to obtain the growth curves of each strain over the course of the experiment (Figure 2.11c). These

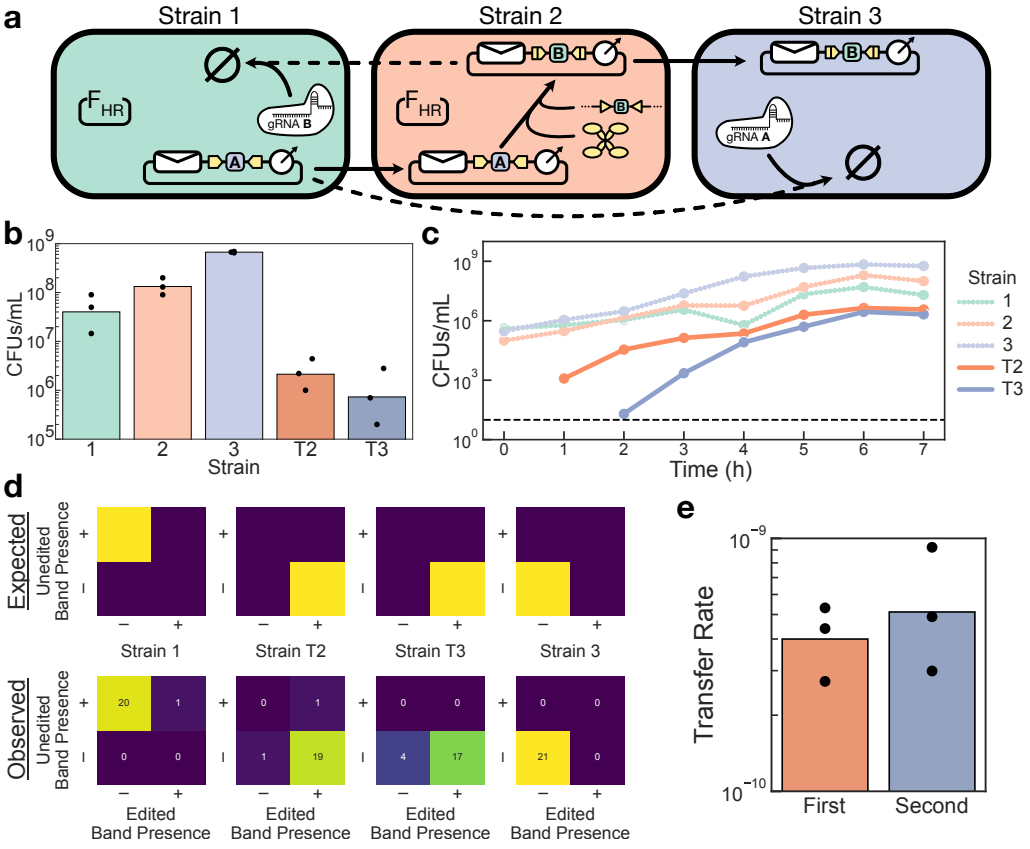

Figure 2.11: A three-strain linear message relay. (a) Schematic of the relay system. The message plasmid starts in Strain 1 and can only be transferred to Strain 2. When the message enters Strain 2, its address is edited so that it can no longer return to Strain 1 but is now allowed to continue on to Strain 3. This architecture is scalable to n strains (Figure 2.10) (b) Endpoint densities of each strain after 6 hours of coculture. c) Timecourse plating of each strain within the coculture for a single biological replicate. The dashed black line marks the limit of detection. (d) PCR assays of endpoint colonies from selected strains. (Top row) The expected plasmid types in each strain based on the relay design. (Bottom row) Results of the PCR assay from 21 colonies of each selected strain. The number of colonies that were assigned to each result condition are indicated in the heatmap. (e) Transfer rate calculated for each step in the relay, based on the data from (b). For the first transfer, Strain 1 is the sender and Strain 2 is the receiver. For the second transfer, Strain T2 is the sender and Strain 3 is the receiver. In all bar graphs, dots show the values from three biological replicates measured on different days, and bars depict the geometric mean of these values.

results are again consistent with the desired system behavior, as Strain 3's transconjugants (T3) do not appear until after Strain 2's transconjugants (T2) have become detectable.

Finally, in order to confirm that each strain only contains the desired form of the message plasmid, we performed PCRs on colonies from the endpoint cultures that selectively amplify either the edited or unedited form of the message plasmid. The results aligned almost directly with the expectation for each tested strain, with the exception of four T3 colonies showing sub-threshold amplification of both plasmid types (Figure 2.11d).

Having demonstrated that our system successfully enforced the sequential linear transfer of the message plasmid through the three-strain consortium, we next asked whether the act of editing the message plasmid imposed a penalty on its transfer rate as it did in Figure 2.8. Encouragingly, we found that the rate of the second (post-edit) transfer in the relay was not lower than the rate of the first (pre-edit) transfer ($p = 0.61$, paired t test) (Figure 2.11e). One possible reason for this discrepancy is that in the relay system, the cell performing the editing of the message plasmid only sees one message plasmid at a time as it enters the cell via conjugation, while in Figure 2.8 the editing was activated in a cell where the message plasmid had already reached its steady-state copy number. Nevertheless, the fact that editing the message plasmid did not impose a detectable decrease in its transfer rate supports the scalability of this linear relay architecture to larger numbers of strains.

Taken together, these results confirm that the address editing system can indeed be used to reliably control the flow of messages through a population.

2.3 Discussion

In this work, we have designed a modular, scalable, and adaptable message addressing framework for DNA-based communication channels and implemented it in an F-mediated plasmid conjugation system in *E. coli* consortia. Because our addressing system is built with molecular components that are orthogonal to the native horizontal gene transfer machinery, any existing DNA-based communication channel can be modified to incorporate our addressing system by expressing Cas9 and a strain-identifying gRNA in the receiver cells and encoding an address region onto the message vector.

Because our goal was to provide a proof-of-concept demonstration of an adaptable DNA communication system, there are many fruitful directions for further optimiza-

tion of this framework. For example, because we expressed our Cas9 and gRNA from a plasmid in our receiver cells, it is likely that mutation and plasmid loss created a subpopulation of receivers without a functional transfer blocking system [51, 52]. By promoting its evolutionary stability, for example by integrating it onto multiple sites on the genome, it is possible that we could improve the system's ability to block off-target transfers even further.

Another promising direction is to improve and augment the transfer properties of the original horizontal gene transfer system itself. The F_{HR} plasmid, like the M13 helper system, constitutively expresses its transfer machinery, but the master transcriptional regulators for these operons have been identified and so could be engineered to increase their expression or place them under inducible control [53]. Interfacing more with the system's channel-intrinsic properties, for example by modulating the expression of entry exclusion proteins to globally block plasmid receipt [54], could also add an additional layer of programmable functionality to the system.

Converting additional horizontally-mobile genetic vectors into new DNA-based communication channels will also be an important component of the continued development of DNA messaging. For example, the F plasmid is known to stop conjugation as the population approaches stationary phase, which limits its overall transfer rate in liquid culture experiments [55]. We observed that this property can also hold for plasmids mobilized by F_{HR} (Figure 2.12) and that this leads to a low overall transfer rate— only around 50% of the receivers in our pairwise transfer experiments were converted to transconjugants after 6 hours of coculture when transfer blocking was not induced (Figure 2.5). In contrast, Ortiz and Endy were able to achieve over 90% receiver conversion after 5 hours of coculture using their M13 bacteriophage-based system [14], despite the fact that the M13 transfer rate has been estimated to be lower than the F transfer rate in coculture conditions [56]. As different applications will be best served by systems with different transfer properties, developing a diverse and well-characterized toolbox of DNA communication channels will be important in facilitating their wider use.

One potential class of applications where the use of our addressing system may not always be appropriate, however, is in cases where a transient amount of off-target expression would be detrimental. Because our system blocks transfer by degrading the message after it has entered the recipient cell, it is possible that genes on the message could be expressed in an off-target recipient before the message is cleaved and degraded— indeed, some genes carried on the F plasmid have been observed to

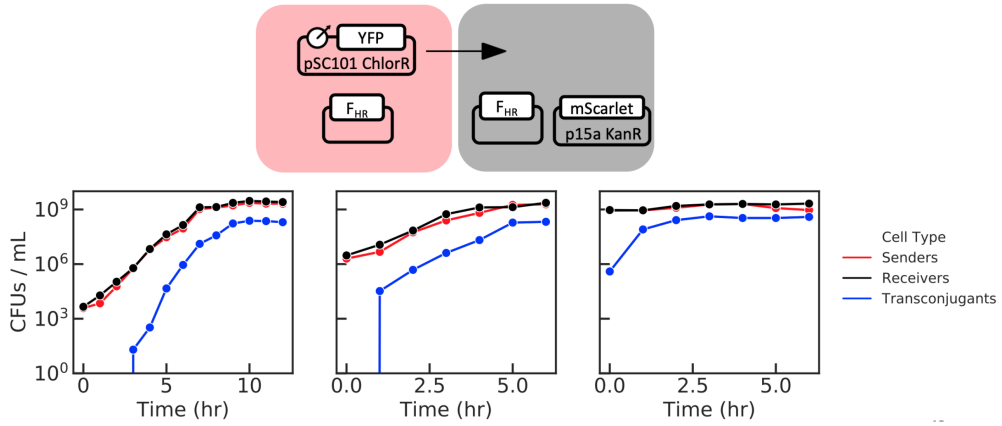

Figure 2.12: Timecourse plating results of F_{HR} -mediated mating experiments without the transfer blocking system. Selective plating with chloramphenicol alone, kanamycin alone, or both antibiotics together was used to calculate the total sender, receiver, and transconjugant density, respectively. Experiments were performed in *E. coli* MG1655 cells, conducted in shaking LB media (as described in the Methods) without antibiotics. The three graphs represent three distinct biological replicates, each one having a different initial strain density for the coculture. In each case, the transconjugant density plateaus before overtaking the entire population.

express as soon as 10 minutes after the plasmid's initial entrance into a receiver cell [57, 58]. In most cases, however, this transient expression phenomenon will likely not be problematic, as the invalid gene products will have a low concentration that is diluted out over time as the cells grow and divide (Figure 2.13a). But if these gene products are able to induce a longer-lasting change in the receiver cell's state during this transient window, then this phenomenon will become a major source of off-target transfers within the consortium (Figure 2.13b).

We therefore set out to determine whether this transient expression phenomenon led to a detectable increase in off-target transfers under conditions similar to our experiments in the main text. In order to detect the presence of transient gene expression from a blocked message plasmid, we constructed receiver cells with a genomically-integrated cassette that can be edited by the BxbI integrase to permanently and heritably activate the chloramphenicol resistance gene. As such, the presence of chloramphenicol resistance in these receiver cells indicates that at one point its ancestry, the cell experienced sufficiently high BxbI expression to activate the resistance cassette. A lack of chloramphenicol resistance in the receivers, therefore, can be used as stringent evidence for the inability of BxbI to accumulate in receiver cells to functional levels.

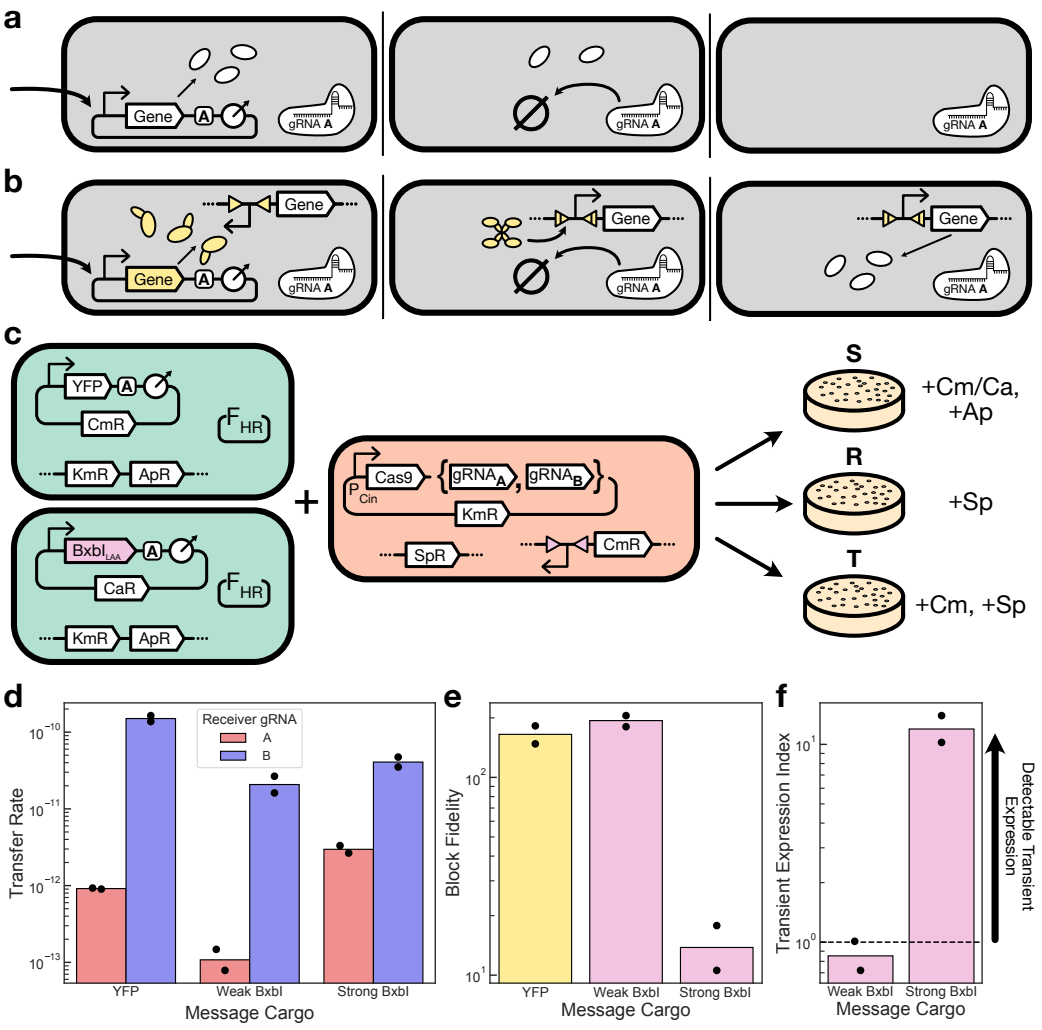

Figure 2.13: Transient Expression from blocked messages. (a) Schematic of transient expression from a blocked message. From Left to Right, an invalid message enters a receiver cell and expresses proteins before it is degraded. Eventually, the proteins themselves are removed naturally. (b) Schematic of transient expression inducing a permanent change in the receiver cell. The fate of the plasmid is identical to (a), but its cargo catalyzes a permanent genetic change in the receiver that persists after the plasmid's removal. (c) Experimental schematic. Sender cells carrying YFP or BxbI message plasmids were mixed in pairwise transfer experiments with receiver cells carrying an on- or off-target gRNA and a genomically-integrated BxbI-activatable chloramphenicol resistance cassette. Transconjugants were always selected with chloramphenicol. (d) Measured transfer rates for the YFP and two versions of the BxbI messages. (e) The Block Fidelity, defined as the ratio of the transfer rates between the valid and invalid receiver, for the data from (d). Higher values indicate better blocking. (f) The Transient Expression Index, defined as the ratio of Block Fidelities between a BxbI and YFP plasmid. A value > 1 suggests that transient expression of the BxbI occurred in the invalid receiver cells. A value ≤ 1 means that transient expression of BxbI in the invalid receiver cells was not detectable. Dots represent two biological replicates measured on different days, and bars indicate their geometric mean. Km = kanamycin, Cm = chloramphenicol, Ca = carbenicillin, Ap = apramycin, Sp = spectinomycin.

We constructed our message plasmids to express destabilized BxbI in the receiver cells by placing them under a salicylate-inducible promoter whose cognate transcription factor is only expressed in the receiver strain. We constructed two variants of these BxbI message plasmids that differ only in their ribosome binding site, so that one plasmid expresses BxbI weakly while the other expresses it strongly. We used the high-copy ColE1 origin of replication for these message plasmids, unlike the low-copy pSC101 origin used in the experiments in the main text, to ensure that the weakly-expressing BxbI plasmid could still produce a sufficient amount of BxbI to activate the chloramphenicol resistance cassette in the receivers (Figure 2.13c).

We then conducted pairwise sender-receiver experiments where we transferred these BxbI message plasmids, bearing the A address site, to receiver strains expressing either the A or B gRNA. In order to measure our system's baseline ability to block ColE1 message plasmids, we constructed another message plasmid variant that expresses YFP and the chloramphenicol resistance gene directly (Figure 2.13c). Because transconjugants were selected with chloramphenicol in all conditions, the YFP plasmid transfer rate captures only transconjugants that currently contain the message plasmid while the BxbI plasmid transfer rate captures receiver cells that at one point in their ancestry received the plasmid for sufficient time to express BxbI and activate the chloramphenicol resistance cassette.

All three message plasmids transferred successfully to the B gRNA receiver, indicating that the BxbI message plasmid, even when weakly expressing the integrase, is able to activate the chloramphenicol resistance gene in the receivers (Figure 2.13d).

We next calculated the effectiveness of the gRNA system at blocking the message plasmids by calculating what we term the Block Fidelity, which is the observed transfer rate to the valid recipient (B gRNA) divided by the transfer rate to the invalid recipient (A gRNA) (Figure 2.13e). A higher value of Block Fidelity indicates more effective blocking of the invalid message plasmid. By normalizing the Block Fidelity of each BxbI plasmid by the Block Fidelity of the YFP plasmid, we obtained a value that we call the Transient Expression Index (Figure 2.13f). If our assay was unable to detect any transient expression of BxbI in the invalid receiver cells, then the Transient Expression Index should take a value of 1. Values greater than 1 indicate that transient expression was detected by our assay.

We observed that the weakly-expressing BxbI plasmid had a Transient Expression Index near 1, while the strongly-expressing BxbI plasmid had a Transient Expression index near 10 (Figure 2.13f). This result indicates that the weakly-expressing BxbI

message plasmid was not able to transiently express enough BxbI to activate the chloramphenicol resistance gene in the receivers, while the strongly-expressing message plasmid could. We can therefore conclude that it is possible to create message plasmids for which the transient expression of their encoded genes within an invalid receiver cell will not be a significant factor. As these experiments are just preliminary, however, a thorough analysis of this phenomenon will likely require a comprehensive characterization of various transfer and blocking systems.

This transient expression phenomenon highlights the fact that DNA-based communication will not necessarily be the appropriate tool for every application. Indeed, although SMA channels do not exhibit many of the useful advantages of DNA channels, their simplicity and reliability nonetheless lets them fill a valuable niche for the efficient implementation of low-complexity communication. In contrast, the role that DNA messaging is well suited to play in the continued development of consortium engineering is to push the boundaries of achievable complexity in the space of behaviors that can be programmed into a system.

One of the most promising examples of such a development is the integration of DNA messaging with the rapidly-advancing field of DNA writing and recording [59]. By allowing cells to directly pass the contents of their recordings to other cells without compression, DNA messaging can enable consortium-level actuation based on these recordings without the drawbacks of bottlenecks from low-capacity communication channels. DNA writing technologies could also be harnessed to generate biologically-interpretable messages *de novo*, paving the way for the types of fully-autonomous self-reconfiguring systems that will enable new types of computation and actuation inaccessible to non-biological substrates [60].

By leveraging the dynamic mutability of DNA messages, alongside the message-channel decoupling and high information density already demonstrated by Ortiz and Endy, our work serves as a second step in the foundation of DNA messaging by creating a single generalizable system that embodies all three of its unique advantages. The ability to leverage a decade of intensive efforts to develop effective molecular DNA editors was critical in enabling our framework, and as these tools continue to advance, DNA messaging is itself poised to increase its functional capacity. Such future progress in DNA messaging that improves and expands upon the three advantages highlighted in our system will bring the field increasingly closer to realizing the ability to engineer autonomous, adaptive multicellular systems that rival the complexity of living systems.

2.4 Materials and methods

Strain and plasmid construction

The parent strain of the Keio single-gene knockout collection [61], *E. coli* BW25113, was used as the basis for all experiments in this study with the exception of those described in Figures 2.12 (*E. coli* MG1655) and 2.13 (*E. coli* Marionette MG1655 [62] for the receiver strains). Genomic integrations were performed using the pOSIP clonetegration system [63].

Because the F_{HR} plasmid retains a low rate of self-transfer activity and carries a tetracycline resistance gene, the plasmid could be transferred from the original F_{HR} donor strain into newly-constructed sender strains using standard mating procedures (see below) and selectively plating for transconjugants.

All new plasmids for this study were constructed via 3G assembly [64] using genetic parts from the CIDAR MoClo extension part kit [65, 66] when available. Parts not in the kit were converted to 3G-compatible parts by amplifying them from an existing source with custom primers or synthesizing the parts directly before combining them with the part plasmid backbone via Gibson assembly. The former approach was used for the inducible promoters and their cognate regulators, taken from the Marionette system [62]; the spectinomycin and apramycin resistance genes, taken from the pQCascade and pCutAmp plasmids, respectively [67]; the gentamycin resistance cassette, taken from the pJM220 plasmid [68]; and the F *oriT* sequence, taken from the mobile GFP plasmid developed by Dimitriu et al. [20].

The latter synthesis-based approach was used for the gRNAs and address regions. Because the gRNAs target sites on the address region whose sequences are fully user-specified, one can in principle choose any arbitrary 20bp sequence to serve as the recognition sequence of the gRNA. In order to avoid crosstalk with the *E. coli* genome, we chose 20bp from the synthetically-generated UNS2 sequence [69] to serve as the A site and 20bp from the sequence of the yeast endonuclease I-SceI [70] to serve as the B site. The orthogonality of both sequences to the *E. coli* genome was validated with BLAST before construction. Address regions were constructed to include approximately 100bp of spacer sequence between the actual gRNA binding site and the flanking integrase attachment site on each side. These spacer sequences were generated by taking random sequences from the ampicillin resistance gene and their orthogonality to the gRNA sequences was validated with BLAST [71]. The D1, D2, D3, and D4 gRNAs used in Figure 2.6 correspond to those labeled "sequence 1" through "sequence 4", respectively, in Figure 1 of Didovyk et al. [37].

All message plasmids in this study, with the exception of those in Figure 2.13, were constructed on a low copy pSC101-origin backbone. The message plasmids in Figure 2.13 were constructed on a high copy ColE1-origin backbone. All non-mobile plasmids used in this study were constructed on a medium copy p15a-origin backbone.

Cell culturing and plasmid transfer experiments

Strains involved in the transfer experiments were grown overnight in 2mL of LB media in a 15mL polyproylene culture tube in a shaking incubator (Thermo MaxQ 4000) set to 37C and 250rpm under antibiotic selection for each resistance present in the strain. In the morning, each culture was diluted 1:100 into 2 mL of fresh LB media containing antibiotic selection for only the plasmid-based resistances in the strain and returned to the shaking incubator until the culture reached midlog phase (approx. 1-2 hours). At this point, cultures were induced with the appropriate amount of inducer, if applicable, and continued incubating for another 1 hour.

Cultures were then removed from the incubator and their OD600 value was measured. 1 mL of the culture was then transferred into a 1.5 mL tube and spun at 1,377 g for 10 min on a tabletop centrifuge. The supernatant was removed and the cell pellet was resuspended in 1 mL of fresh LB containing only kanamycin (or no antibiotics, for Figure 2.12), alongside the appropriate concentration of inducer if applicable. Cultures were then spun again at the same settings and resuspended in fresh media as before.

Cells in the washed cultures were then diluted into a single 3 mL culture of fresh LB, containing only the appropriate inducers and kanamycin (or no antibiotics, for Figure 2.12), in a 15 mL culture tube. Cells were added such that each strain would have an OD600 value of 0.002 within the final coculture, which typically involved at least a 1:100 dilution from the original monoculture. The coculture was then placed back into the shaking incubator, marking the beginning of the 6 hour coculturing window.

The concentrations of the antibiotics in the medias, when used, were 25 µg/mL kanamycin, 12.5 µg/mL chloramphenicol, 25 µg/mL apramycin, 25 µg/mL spectinomycin, 15 µg/mL gentamicin, 50 µg/mL carbenicillin, and 10 µg/mL tetracycline.

Selective plating and measuring strain densities

After 6 hours of coculturing (or at hourly timepoints, for Figure 2.11c and Figure 2.12), the culture tube was removed from the incubator and the density of each strain was assessed by selective plating of serial dilutions of the culture. 60mm LB agar plates containing the appropriate antibiotic markers (the unique genomically-integrated resistance cassette for the strain as well as chloramphenicol to select for the message plasmid, when appropriate) were used for selection. For all experiments except those in Figure 2.11 and Figure 2.12, serial dilutions were performed with 10-fold steps in 100 µL volumes and four 5 µL spots of successive dilutions spanning the expected density were spread onto a single plate. For the remaining experiments, serial dilutions were performed with 100-fold steps in 1 mL volumes and 100 µL of one or two dilutions was spread onto individual plates. Plates were incubated at 37C until the formation of colonies (12-24 hours).

Strain densities, measured as colony forming units per mL, were calculated by counting the number of colonies on the selection plates and multiplying by the appropriate dilution factor. When multiple dilution factors displayed growth, the dilution factor with the highest number of colonies that still remained countable (i.e. colonies were clearly discernible and separable) was used to calculate the density. Colonies were counted manually.

When fluorescent proteins were used to distinguish different colonies on the same selection plate, as in Figure 2.6, plates were imaged on an Olympus MVX10 microscope using MicroManager version 2.0.0 with bandpass filters at 427/10-25 nm (TagBFP), 504/12-25 nm (sfYFP), and 589/15-25 nm (mScarlet-I).

Calculating transfer rates

The transfer rate was calculated as $T/(S * R)$, where T is the density of transconjugants, S is the density of senders, and R is the total density of receivers, which includes the receivers that have become transconjugants. Although this ratio is a standard measure of transfer rate used in the literature [72, 73], we note that some recent works use this measure in a subtly different way, calculating the transfer rate as $T/(S*R)$ but not including the transconjugant density within R term [74–76]. We chose to preserve the inclusion of the transconjugants in the R term for two reasons. First, by defining R as the total receiver density, experiments where transconjugants cannot be distinguished from receivers on receiver-selecting plates, such as those in Figure 2.6, can be analyzed in the same way as experiments where this distinc-

tion can be made. Second, if the transfer process ever went to completion and all receivers were converted into transconjugants, the value of $T/(S*R)$ would not be infinite as it would if R were allowed to go to 0.

We preserved our definition of R for the calculation of the fractional receiver conversion, T/R (Figure 2.5). This value should range between 0 and 1.

PCR assay for message plasmid identity

Colonies were picked and resuspended into 10 µL of M9 minimal media, of which 1 µL was placed into two separate 10 µL PCR reactions with primers designed to bind to the *oriT* and either the A or B gRNA binding site. Primer sequences were, for the unedited message plasmid (A site), CGCAGAATCCAAGCCG and CGGATAAAGTCACCAGAGGTG (with an annealing temperature of 64C) and for the edited message plasmid (B site), GGGATAACAGGGTAATC and GATAAAGTCACCAGAGG (with an annealing temperature of 56C).

The number of PCR cycles was adjusted for each reaction against positive control colonies (cells containing a single message plasmid with either just the A site or just the B site on its address) to reduce the probability of observing false positives in the assay. The temperature program was 5 minutes at 98C followed by N cycles of 10 seconds at 98C, 30 seconds at the annealing temperature, and 20 seconds at 72C. After the cycles were completed, the reaction was kept at 72C for an additional 5 minutes before cooling down to 4C. N was 23 for the reaction targeting the unedited address and N was 26 for the reaction targeting the edited address.

PCR samples were run on a gel and imaged on a UV imager, and the presence and absence of a band for each sample was determined by eye.

References

[1] Katherine E. Duncker, Zachary A. Holmes, and Lingchong You. “Engineered microbial consortia: strategies and applications”. *Microbial Cell Factories* 20.1 (2021), pp. 1–13.

[2] Ryan Tsoi, Zhuojun Dai, and Lingchong You. “Emerging strategies for engineering microbial communities”. *Biotechnology Advances* 37.6 (2019), p. 107372.

[3] Nicholas S. McCarty and Rodrigo Ledesma-Amaro. “Synthetic biology tools to engineer microbial communities for biotechnology”. *Trends in Biotechnology* 37.2 (2019), pp. 181–197.

[4] Sergi Regot et al. “Distributed biological computation with multicellular engineered networks”. *Nature* 469.7329 (2011), pp. 207–211.

[5] Kang Zhou et al. “Distributing a metabolic pathway among a microbial consortium enhances production of natural products”. *Nature Biotechnology* 33.4 (2015), pp. 377–383.

[6] Behzad D. Karkaria et al. “From microbial communities to distributed computing systems”. *Frontiers in Bioengineering and Biotechnology* 8 (2020), p. 834.

[7] Michael J. Liao et al. “Rock-paper-scissors: Engineered population dynamics increase genetic stability”. *Science* 365.6457 (2019), pp. 1045–1049.

[8] Rory L. Williams and Richard M. Murray. “Integrase-mediated differentiation circuits improve evolutionary stability of burdensome and toxic functions in E. coli”. *Nature Communications* 13.1 (2022).

[9] René Michele Davis, Ryan Yue Muller, and Karmella Ann Haynes. “Can the natural diversity of quorum-sensing advance synthetic biology?” *Frontiers in Bioengineering and Biotechnology* 3 (2015), p. 30.

[10] Pei Du et al. “De novo design of an intercellular signaling toolbox for multichannel cell–cell communication and biological computation”. *Nature Communications* 11.1 (2020), pp. 1–11.

[11] Spencer R. Scott and Jeff Hasty. “Quorum sensing communication modules for microbial consortia”. *ACS Synthetic Biology* 5.9 (2016), pp. 969–977.

[12] Nicolas Kylilis et al. “Tools for engineering coordinated system behaviour in synthetic microbial consortia”. *Nature Communications* 9.1 (2018), pp. 1–9.

[13] Sonja Billerbeck et al. “A scalable peptide-GPCR language for engineering multicellular communication”. *Nature Communications* 9.1 (2018), pp. 1–12.

[14] Monica E. Ortiz and Drew Endy. “Engineered cell-cell communication via DNA messaging”. *Journal of Biological Engineering* 6.1 (2012), pp. 1–12.

[15] John T. Sexton and Jeffrey J. Tabor. “Multiplexing cell-cell communication”. *Molecular Systems Biology* 16.7 (2020), e9618.

[16] Wentao Kong et al. “Designing microbial consortia with defined social interactions”. *Nature Chemical Biology* 14.8 (2018), pp. 821–829.

[17] Alex J.H. Fedorec et al. “Single strain control of microbial consortia”. *Nature Communications* 12.1 (2021), pp. 1–12.

[18] Sampriti Mukherjee and Bonnie L. Bassler. “Bacterial quorum sensing in complex and dynamically changing environments”. *Nature Reviews Microbiology* 17.6 (2019), pp. 371–382.

[19] Ilenne Del Valle et al. “Artificial soils reveal individual factor controls on microbial processes”. *Msystems* 7.4 (2022), e00301–22.

[20] Tatiana Dimitriu et al. “Genetic information transfer promotes cooperation in bacteria”. *Proceedings of the National Academy of Sciences* 111.30 (2014), pp. 11103–11108.

[21] Trine Aakvik Strand et al. “A new and improved host-independent plasmid system for RK2-based conjugal transfer”. *PLoS One* 9.3 (2014), e90372.

[22] Mitsuhiro Itaya et al. “Far rapid synthesis of giant DNA in the Bacillus subtilis genome by a conjugation transfer system”. *Scientific Reports* 8.1 (2018), pp. 1–6.

[23] Robert W. Bradley, Martin Buck, and Baojun Wang. “Recognizing and engineering digital-like logic gates and switches in gene regulatory networks”. *Current Opinion in Microbiology* 33 (2016), pp. 74–82.

[24] Jennifer A.N. Brophy et al. “Engineered integrative and conjugative elements for efficient and inducible DNA transfer to undomesticated bacteria”. *Nature Microbiology* 3.9 (2018), pp. 1043–1053.

[25] Carlotta Ronda et al. “Metagenomic engineering of the mammalian gut microbiome in situ”. *Nature Methods* 16.2 (2019), pp. 167–170.

[26] Benjamin E. Rubin et al. “Species-and site-specific genome editing in complex bacterial communities”. *Nature Microbiology* 7.1 (2022), pp. 34–47.

[27] Angel Goñi-Moreno, Martyn Amos, and Fernando de la Cruz. “Multicellular computing using conjugation for wiring”. *PLoS One* 8.6 (2013), e65986.

[28] Angel Goñi-Moreno et al. “Dynamical task switching in cellular computers”. *Life* 9.1 (2019), p. 14.

[29] David Beneš, Alfonso Rodríguez-Patón, and Petr Sosík. “Directed evolution of biocircuits using conjugative plasmids and CRISPR-Cas9: design and in silico experiments”. *Natural Computing* 16.3 (2017), pp. 497–505.

[30] Paul C.M. Fogg et al. “New applications for phage integrases”. *Journal of Molecular Biology* 426.15 (2014), pp. 2703–2716.

[31] Andrew V. Anzalone, Luke W. Koblan, and David R. Liu. “Genome editing with CRISPR–Cas nucleases, base editors, transposases and prime editors”. *Nature Biotechnology* 38.7 (2020), pp. 824–844.

[32] Luciano A. Marraffini and Erik J. Sontheimer. “CRISPR interference limits horizontal gene transfer in staphylococci by targeting DNA”. *Science* 322.5909 (2008), pp. 1843–1845.

[33] Giedrius Gasiunas et al. “Cas9–crRNA ribonucleoprotein complex mediates specific DNA cleavage for adaptive immunity in bacteria”. *Proceedings of the National Academy of Sciences* 109.39 (2012), E2579–E2586.

[34] Brian J. Caliando and Christopher A. Voigt. “Targeted DNA degradation using a CRISPR device stably carried in the host genome”. *Nature Communications* 6.1 (2015), pp. 1–10.

[35] Yu-Zhang He et al. “A transposon-associated CRISPR/Cas9 system specifically eliminates both chromosomal and plasmid-borne mcr-1 in Escherichia coli”. *Antimicrobial Agents and Chemotherapy* 65.10 (2021), e01054–21.

[36] Fuguo Jiang and Jennifer A. Doudna. “CRISPR-Cas9 structures and mechanisms”. *Annu Rev Biophys* 46.1 (2017), pp. 505–529.

[37] Andriy Didovyk et al. “Orthogonal modular gene repression in Escherichia coli using engineered CRISPR/Cas9”. *ACS Synthetic Biology* 5.1 (2016), pp. 81–88.

[38] Austin G. Rottinghaus, Steven Vo, and Tae Seok Moon. “Computational design of CRISPR guide RNAs to enable strain-specific control of microbial consortia”. *Proceedings of the National Academy of Sciences* 120.1 (2023), e2213154120.

[39] Lars Andrup et al. “Kinetics of Conjugative Transfer: A Study of the Plasmid pXO16 fromBacillus thuringiensissubsp. israelensis”. *Plasmid* 40.1 (1998), pp. 30–43.

[40] Uli Klümper et al. “Broad host range plasmids can invade an unexpectedly diverse fraction of a soil bacterial community”. *The ISME Journal* 9.4 (2015), pp. 934–945.

[41] Koji Inomata, Masanobu Nishikawa, and Kazuo Yoshida. “The yeast Saccharomyces kluyveri as a recipient eukaryote in transkingdom conjugation: behavior of transmitted plasmids in transconjugants”. *Journal of Bacteriology* 176.15 (1994), pp. 4770–4773.

[42] K.A. Ippen-Ihler and E.G. Minkley Jr. “The conjugation system of F, the fertility factor of Escherichia coli”. *Annual Review of Genetics* 20.1 (1986), pp. 593–624.

[43] Daphne S. Bindels et al. “mScarlet: a bright monomeric red fluorescent protein for cellular imaging”. *Nature Methods* 14.1 (2017), pp. 53–56.

[44] Ye Chen et al. “Emergent genetic oscillations in a synthetic microbial consortium”. *Science* 349.6251 (2015), pp. 986–989.

[45] Oksana M. Subach et al. “Conversion of red fluorescent protein into a bright blue probe”. *Chemistry & Biology* 15.10 (2008), pp. 1116–1124.

[46] Christine A. Merrick, Jia Zhao, and Susan J. Rosser. “Serine integrases: advancing synthetic biology”. *ACS Synthetic Biology* 7.2 (2018), pp. 299–310.

[47] Jerome Bonnet, Pakpoom Subsoontorn, and Drew Endy. “Rewritable digital data storage in live cells via engineered control of recombination directionality”. *Proceedings of the National Academy of Sciences* 109.23 (2012), pp. 8884–8889.

[48] Lei Yang et al. “Permanent genetic memory with >1-byte capacity”. *Nature Methods* 11.12 (2014), pp. 1261–1266.

[49] Matthew T.N. Yarnall et al. “Drag-and-drop genome insertion of large sequences without double-strand DNA cleavage using CRISPR-directed integrases”. *Nature Biotechnology* (2022), pp. 1–13.

[50] Soeren Turan et al. “Recombinase-mediated cassette exchange (RMCE): traditional concepts and current challenges”. *Journal of Molecular Biology* 407.2 (2011), pp. 193–221.

[51] Andrew D. Halleran, Emanuel Flores-Bautista, and Richard M. Murray. “Quantitative characterization of random partitioning in the evolution of plasmid-encoded traits”. *bioRxiv Preprint* (2019), p. 594879.

[52] Bin Shao et al. “Single-cell measurement of plasmid copy number and promoter activity”. *Nature Communications* 12.1 (2021), pp. 1–9.

[53] Malgorzata Zatyka and Christopher M. Thomas. “Control of genes for conjugative transfer of plasmids and other mobile elements”. *FEMS Microbiology Reviews* 21.4 (1998), pp. 291–319.

[54] M. Pilar Garcillán-Barcia and Fernando de la Cruz. “Why is entry exclusion an essential feature of conjugative plasmids?” *Plasmid* 60.1 (2008), pp. 1–18.

[55] Laura S. Frost and Jan Manchak. “F-phenocopies: characterization of expression of the F transfer region in stationary phase”. *Microbiology* 144.9 (1998), pp. 2579–2587.

[56] Zhenmao Wan and Noel L. Goddard. “Competition between conjugation and M13 phage infection in Escherichia coli in the absence of selection pressure: a kinetic study”. *G3: Genes| Genomes| Genetics* 2.10 (2012), pp. 1137–1144.

[57] Sophie Nolivos et al. “Role of AcrAB-TolC multidrug efflux pump in drug-resistance acquisition by plasmid transfer”. *Science* 364.6442 (2019), pp. 778–782.

[58] Agathe Couturier et al. “Real-time visualisation of the intracellular dynamics of conjugative plasmid transfer”. *Nature Communications* 14.1 (2023), p. 294.

[59] Fahim Farzadfard and Timothy K. Lu. “Emerging applications for DNA writers and molecular recorders”. *Science* 361.6405 (2018), pp. 870–875.

[60] Lewis Grozinger et al. “Pathways to cellular supremacy in biocomputing”. *Nature Communications* 10.1 (2019), pp. 1–11.

[61] Tomoya Baba et al. “Construction of Escherichia coli K-12 in-frame, single-gene knockout mutants: the Keio collection”. *Molecular Systems Biology* 2.1 (2006), pp. 2006–0008.

[62] Adam J. Meyer et al. “Escherichia coli “Marionette” strains with 12 highly optimized small-molecule sensors”. *Nature Chemical Biology* 15.2 (2019), pp. 196–204.

[63] François St-Pierre et al. “One-step cloning and chromosomal integration of DNA”. *ACS Synthetic Biology* 2.9 (2013), pp. 537–541.

[64] Andrew D. Halleran, Anandh Swaminathan, and Richard M. Murray. “Single day construction of multigene circuits with 3G assembly”. *ACS Synthetic Biology* 7.5 (2018), pp. 1477–1480.

[65] Sonya V. Iverson et al. “CIDAR MoClo: improved MoClo assembly standard and new E. coli part library enable rapid combinatorial design for synthetic and traditional biology”. *ACS Synthetic Biology* 5.1 (2016), pp. 99–103.

[66] Samuel Clamons et al. *CIDAR MoClo Extension Part Kit, Volume 1*. `https://www.addgene.org/kits/murray-cidar-moclo-v1/`. 2019.

[67] Yiwen Zhang et al. “Multicopy chromosomal integration using CRISPR-associated transposases”. *ACS Synthetic Biology* 9.8 (2020), pp. 1998–2008.

[68] Jeffrey Meisner and Joanna B. Goldberg. “The Escherichia coli rhaSR-PrhaBAD inducible promoter system allows tightly controlled gene expression over a wide range in Pseudomonas aeruginosa”. *Applied and Environmental Microbiology* 82.22 (2016), pp. 6715–6727.

[69] Joseph P. Torella et al. “Rapid construction of insulated genetic circuits via synthetic sequence-guided isothermal assembly”. *Nucleic Acids Research* 42.1 (2014), pp. 681–689.

[70] Leo Baumgart, William Mather, and Jeff Hasty. “Synchronized DNA cycling across a bacterial population”. *Nature Genetics* 49.8 (2017), pp. 1282–1285.

[71] Stephen F. Altschul et al. “Gapped BLAST and PSI-BLAST: A new generation of protein database search programs”. *Nucleic Acids Research* 25.17 (1997), pp. 3389–3402.

[72] Niels Kroer et al. “Effect of root exudates and bacterial metabolic activity on conjugal gene transfer in the rhizosphere of a marsh plant”. *FEMS Microbiology Ecology* 25.4 (1998), pp. 375–384.

[73] Jorge Rodriguez-Grande and Raul Fernandez-Lopez. “Measuring plasmid conjugation using antibiotic selection”. *Horizontal Gene Transfer*. Springer, 2020, pp. 93–98.

[74] Allison J. Lopatkin et al. “Antibiotics as a selective driver for conjugation dynamics”. *Nature Microbiology* 1.6 (2016), pp. 1–8.

[75] Allison J. Lopatkin et al. “Persistence and reversal of plasmid-mediated antibiotic resistance”. *Nature Communications* 8.1 (2017), pp. 1–10.

[76] Robin Tecon et al. “Cell-to-cell bacterial interactions promoted by drier conditions on soil surfaces”. *Proceedings of the National Academy of Sciences* 115.39 (2018), pp. 9791–9796.

Chapter 3

REACTION ORDER POLYTOPES CONSTRAIN BIOMOLECULAR BEHAVIOR

The work described in this chapter is currently being prepared for publication under the attribution

> Fangzhou Xiao and John P. Marken. "Polytopal constraints govern the behavior of biomolecular reaction systems" (*In preparation*).
> F.X. and J.P.M. jointly conceived and developed the project and performed the analyses.

3.1 Introduction

Since the inception of the field, synthetic biology has understood the essential role of mathematical models in guiding the design process for genetic circuits [1, 2]. Because the nonlinear, stochastic, and multidimensional nature of biomolecular reaction systems permit many possible behaviors and configurations, it is simply not feasible to fully understand the behavior of even a simple genetic circuit without the aid of mathematical models.

This complexity increases significantly when the models expand their scope to incorporate the cellular context of their host organism. Even when this is done in an abstracted way, for example by representing the host's metabolic capacity as a limited resource pool [3], qualitatively new types of behaviors can emerge for even the simplest systems. Conventional mathematical models, therefore, while necessary for enabling the design process for engineered biomolecular systems, are also insufficient to offer a true holistic understanding of these systems' behaviors across all possible conditions [4, 5]

However, the challenge of environmental synthetic biology necessitates that we design our systems in order to withstand such variability, including unknown unknowns. There are two ways to resolve this. On one hand, one could design the circuits to incorporate autonomous control systems that perform dynamic error correction to maintain their desired performance in the face of variability [6]. The other approach is to find a mathematical framework that can tractably represent the

entirety of a system's behavior, and use this as the basis for the design. In this section, we develop a framework for the analysis of biomolecular reaction systems that can, for a certain class of responses of a certain class of systems, indeed represent all possible system behaviors in a tractable way.

Specifically, our framework addresses **binding networks**, which are networks of reversible reactions that only involve the formation and dissociation of molecular complexes, and do not represent their creation or destruction. We analyze these binding networks by calculating the reaction order of its activity to its species concentrations and binding affinities. The **reaction order** of a quantity $f(x)$ to a variable x is a measure of $f(x)$'s sensitivity to x– specifically, it is $\frac{\partial \log f(x)}{\partial \log x}$, the slope of the relationship on a log-log plot. While initially this concept may seem obtuse, the reaction order is actually a natural representation of many biomolecular behaviors useful for synthetic biologists. The robustness of a quantity to a parameter corresponds to a reaction order of 0, for example, while an ultrasensitive response corresponds to a reaction order with magnitude greater than 1.

We find that the reaction order of all species in a binding network with respect to their concentrations and binding affinities lie within a polytope (an n-dimensional polygon) in reaction order space. These polytopes define the bounds constraining the space of the system's possible behaviors, so that any behavior outside of the polytope is fundamentally unachievable by the system. This insight forms the basis of our analysis framework.

In Section 3.2, we introduce the central concepts of reaction order analysis. In Section 3.3, we describe a procedure to generate the reaction order polytope for any arbitrary binding network and illustrate this procedure on a simple model of enzyme-substrate binding. In Section 3.4, we apply reaction order analysis to a simple model of cooperativity to investigate the functional benefits provided by incorporating cooperativity into a system. In Section 3.5, we apply reaction order analysis to a simple model of transcriptional regulation and identify functional differences between activators and repressors which to our knowledge have not previously been observed. Finally, we conclude in Section 3.6 by discussing the next steps for the development of this framework.

3.2 Interpreting biomolecular behavior through reaction order

In order to illustrate the use of the reaction order to analyze the behavior of a biomolecular reaction system, we will consider a simple model of a single enzymatic

reaction. Here, an enzyme E binds with a substrate S to form a complex C before converting that substrate into a product P. The reactions governing this process are

$$E + S \rightleftharpoons C \rightarrow E + P, \tag{3.1}$$

where we will say that the reversible reactions occur with forward and reverse rates k_+ and k_-, respectively, and the irreversible catalysis reaction occurs at rate k_c.

If we are interested in how the steady-state concentration of the product species P changes as various relevant system parameters are tuned, we note that because

$$\frac{\mathrm{d}P}{\mathrm{d}t} = k_c C, \tag{3.2}$$

the influence of all system variables other than k_c will affect P exclusively through their influence on C. Therefore, we can analyze the simpler system

$$E + S \rightleftharpoons C \tag{3.3}$$

in order to determine these influences. Unlike Model 3.1, Model 3.3 is a binding network because all of the reactions are reversible and only depict the formation and dissociation of various types of complexes (i.e. no species are created or destroyed).

There are three system variables that affect C in Equation 3.3. First, there is the binding affinity between E and S, which can be represented by the dissociation constant $K = k_-/k_+$. The remaining two variables are the concentrations of the enzyme and substrate. While at first glance these may appear to correspond to the variables E and S, these variables only represent the *unbound* concentrations of enzyme and substrate. The actual biologically-relevant variables are the total enzyme and substrate concentrations, $t_E = E + C$ and $t_S = S + C$.

We emphasize that for Model 3.3, and for any binding network in general, that the totals and the binding affinities capture all possible impacts on the value of the species concentration C. This means that characterizing the functional relationship between C and these system variables will include the impact of all possible environmental perturbations on the system, as these impacts, regardless of their source, will manifest as a change in the values of the totals or the binding affinities. The only type of environmental impact that is not captured by these quantities would be a change to the fundamental stoichiometry of the reactions themselves, which would invalidate the validity of the entire model itself. We posit that such impacts are unlikely to occur through environmental variation, however, and are relevant only at the long-term timescales of protein evolution.

We will therefore assume for the remainder of this chapter that variations in the totals and the binding affinities constitute all possible variations in the system's state. Specifically, for Model 3.3, we are interested in calculating how the steady-state concentration of C changes as a function of K, t_E, t_S. This can be solved analytically as

$$C = \frac{1}{2}\left(t_E + t_S + K - \sqrt{(t_E + t_S + K)^2 - 4t_E t_S}\right), \tag{3.4}$$

where we have taken the smaller root of the binomial because the larger one implies the nonphysical situation where the value of a total is less than the value of its component species.

While Equation 3.4 gives the exact relationship between the system variables and C, its functional form does not lend itself easily to insights. More importantly, Equation 3.4 is the solution to a polynomial equation, and closed-form solutions do not exist for polynomials of degree ≥ 5. Therefore analytical solutions cannot be found for systems that even have a moderate increase in complexity to reaction network 3.3.

This dilemma is usually resolved by applying approximations to simplify the system. The Michaelis-Menten approximation is a canonical example, which when applied to reaction network 3.3 invokes the assumption that the substrate concentration is much greater than the enzyme, i.e. $t_S \gg t_E$. This implies that $t_S \approx S$, which allows for the simplified relation

$$C \approx t_E \frac{S}{S + K}. \tag{3.5}$$

While the functional form of Equation 3.5 is much more interpretable than that of Equation 3.4, and the Michaelis-Menten approximation can always be applied to a reaction network to obtain a closed-form solution, the approximation is nonetheless not valid unless its fundamental assumptions are satisfied. When designing biomolecular systems to behave in unpredictable environments, it should be expected that there will be situations where these assumptions are not satisfied, in which case the system behavior will deviate from predictions obtained through approximations.

It is therefore desirable to have an exact mathematical representation of the influence of the system control variables that does not rely on assumptions about their values. However, as was demonstrated by Equation 3.4, such a representation cannot capture

the exact influence of the control variables on C itself. It is possible, however, to exactly capture the reaction order relationship between the control variables and C.

The reaction order is calculated via the mathematical operation of the log derivative, as it ignores additive and multiplicative factors to only preserve the exponent of a variable (Appendix A). The log derivative can also be conceptualized as the slope of a function on a log-log plot.

For a binding network, we are interested in calculating the log derivatives of each species x with respect to each total t and binding affinity k. In other words, we would like to determine the matrix

$$\boldsymbol{H} := \begin{bmatrix} \frac{\partial \log \boldsymbol{x}}{\partial \log \boldsymbol{t}} & \frac{\partial \log \boldsymbol{x}}{\partial \log \boldsymbol{k}} \end{bmatrix}.$$

For any binding network, the vector of species $\boldsymbol{x}$ and the vector of conserved quantities (or total species concentrations) $\boldsymbol{t}$ can be determined directly by inspection of the network. These can then be used to calculate a conservation law matrix $\boldsymbol{L}$ via

$$\boldsymbol{t} = \boldsymbol{L}\boldsymbol{x}. \tag{3.6}$$

The stoichiometric matrix $\boldsymbol{N}$ can also be calculated by visual inspection, where each row of $\boldsymbol{N}$ encodes the stoichiometry of each species in the reverse direction of each binding reaction. Specifically, $\boldsymbol{N}$ satisfies the steady-state relation

$$\log \boldsymbol{k} = \boldsymbol{N} \log \boldsymbol{x}. \tag{3.7}$$

These quantities can be used to calculate the reaction order matrix $\boldsymbol{H}$ directly. By applying the implicit function theorem and the properties of the log derivative, we can obtain the relation

$$\boldsymbol{H} := \frac{\partial \log \boldsymbol{x}}{\partial \log \boldsymbol{t}, \boldsymbol{k}} = \begin{bmatrix} \boldsymbol{\Lambda}_{\boldsymbol{t}}^{-1} \boldsymbol{L} \boldsymbol{\Lambda}_{\boldsymbol{x}} \\ \boldsymbol{N} \end{bmatrix}^{-1}, \tag{3.8}$$

where $\boldsymbol{\Lambda}_{\boldsymbol{y}}$ is the diagonalization of the vector $\boldsymbol{y}$. A detailed derivation of Equation 3.8 is given as Theorem 3.5.1 in Fangzhou Xiao's thesis [7].

The matrix on the right hand side of Equation 3.8 can be written down directly from the structure of the binding network. We will now illustrate this procedure using Model 3.3.

First, we note that our species and conserved quantities are

$$\boldsymbol{x} = \begin{bmatrix} E \\ S \\ C \end{bmatrix},$$
$$\boldsymbol{t} = \begin{bmatrix} t_E \\ t_S \end{bmatrix}.$$

Because $t_E = E + C$ and $t_S = S + C$, we can collect these quantities into our conservation law matrix

$$\boldsymbol{L} = \begin{bmatrix} 1 & 0 & 1 \\ 0 & 1 & 1 \end{bmatrix},$$

where the columns are ordered according to the ordering of $\boldsymbol{x}$.

Finally, our single reaction $E + S \rightleftharpoons C$ yields the stoichiometric matrix

$$\boldsymbol{N} = \begin{bmatrix} 1 & 1 & -1 \end{bmatrix},$$

where the columns are ordered as in $\boldsymbol{L}$.

These four components, $\boldsymbol{x}$, $\boldsymbol{t}$, $\boldsymbol{L}$, and $\boldsymbol{N}$, are sufficient to calculate the matrix on the right hand side of Equation 3.8,

$$\begin{bmatrix} \boldsymbol{\Lambda_t L \Lambda_x} \\ \boldsymbol{N} \end{bmatrix} = \begin{bmatrix} \frac{\partial \log \boldsymbol{t}}{\partial \log \boldsymbol{x}} \\ \frac{\partial \log \boldsymbol{k}}{\partial \log \boldsymbol{x}} \end{bmatrix} = \begin{bmatrix} \frac{E}{t_E} & 0 & \frac{C}{t_E} \\ 0 & \frac{S}{t_S} & \frac{C}{t_S} \\ 1 & 1 & -1 \end{bmatrix}.$$

Inverting the above matrix gives the reaction order matrix,

$$\boldsymbol{H} = \frac{1}{1+e+s} \begin{bmatrix} (1+e)(1+s) & -s(1+e) & s \\ -e(1+s) & (1+e)(1+s) & e \\ 1+s & 1+e & -1 \end{bmatrix}, \tag{3.9}$$

where $e \equiv E/K$ and $s \equiv S/K$. Recall that the entries of $\boldsymbol{H}$ have the interpretation

$$\boldsymbol{H} = \begin{bmatrix} \frac{\partial \log E}{\partial \log t_E} & \frac{\partial \log E}{\partial \log t_S} & \frac{\partial \log E}{\partial \log K} \\ \frac{\partial \log S}{\partial \log t_E} & \frac{\partial \log S}{\partial \log t_S} & \frac{\partial \log S}{\partial \log K} \\ \frac{\partial \log C}{\partial \log t_E} & \frac{\partial \log C}{\partial \log t_S} & \frac{\partial \log C}{\partial \log K} \end{bmatrix}.$$

Equation 3.9 provides the following information: for a given point in concentration space (defined by specific values of E, S, K, which uniquely determine a specific

value of E, S, C via the relation $C = ES/K$), we can know the sensitivity of any of the species to any of the system control parameters t_E, t_S, K.

We are specifically interested in knowing the sensitivity of the active species C with respect to the total enzyme and total substrate concentrations t_E and t_S, because these are the variables that a cell is easily able to dynamically control in order to achieve a particular aim. We will consider the dissociation constant K to be a parameter that will vary across different environmental contexts (for example pH or salt concentration), but is more difficult to actively control at the same timescale as t_E and t_S.

Looking at the relevant entries of $\boldsymbol{H}$ in Equation 3.9, we can see that the value of $\frac{\partial \log C}{\partial \log t_E, t_S}$ is fully bounded within a polytope (Figure 3.1). Because Equation 3.9 holds for all possible values of $\boldsymbol{x}$, the significance of this result is that the region depicted in Figure 3.1 captures the entirety of C's possible reaction order relations to t_E and t_S.

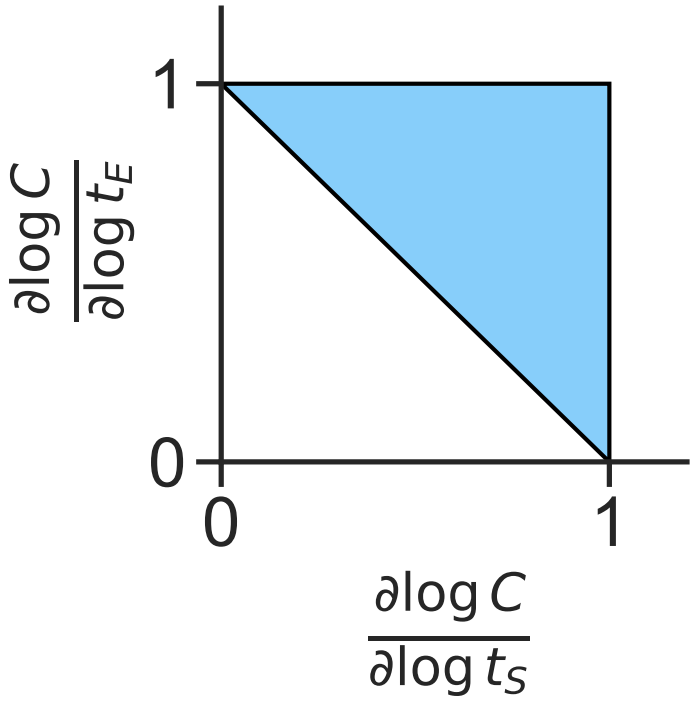

Figure 3.1: The reaction order of C with respect to the total enzyme concentration t_E and total substrate concentration t_S is bounded within the shaded region for all possible system states $\boldsymbol{x}$ in Model 3.3.

In order to gain some intuition about how this polytope should be interpreted, we can first look to its vertices. Here, the values of the reaction orders take integer

values, meaning the system can be approximated by a simple birth-death system (Section 4.2). At the $(1, 1)$ vertex, $C \propto t_E^1 t_S^1$ so the system's activity responds linearly to changes in t_E and t_S. At the $(0, 1)$ vertex, however, $C \propto t_E^1 t_S^0$, meaning the system's activity has saturated and no longer responds to changes in t_S, although it still responds linearly to changes in t_E.

By making these interpretations of the vertices, one can immediately see that it is impossible for the system's activity to be saturated to both t_E and t_S simultaneously, as that would correspond to the $(0, 0)$ point which lies outside of the polytope. Because the polytope bounds all possible system behaviors, this visual observation constitutes a proof– the reaction order framework's ability to directly and visually enable such insights is a major advantage over conventional approximation-based methods.

To further illustrate the consequences of approximation-based analysis, we will return to the Michaelis-Menten approximation (Equation 3.5), reproduced below.

$$C \approx t_E \frac{t_S}{t_S + K} \tag{3.5}$$

The functional form of the Michaelis-Menten approximation ensures that the reaction order relation of C to t_E is always 1, meaning that invoking this approximation reduces the scope of the analysis to a subset of the reaction order space, as depicted in Figure 3.2.

Taking this view makes it clear that any insights drawn from the approximation cannot be assumed to hold to the system as a whole, particularly when those insights are claims about the system's inability to exhibit a particular behavior.

Given that this system is typically studied through the lens of the Michaelis-Menten approximation, we may be curious about the $(1, 0)$ vertex which is not captured by the approximation. Here, the system's activity is saturated against the total enzyme concentration t_E but remains sensitive to the total substrate t_S. Examining the functional forms of the relevant entries of $\boldsymbol{H}$ in Equation 3.9 reveals that this vertex is achieved when $e \gg 1$ and $s \ll 1$, or in other words, $E \gg K \gg S$. This is equivalent to $E \gg C \gg S$, which in turn is equivalent to the statement that $t_E \approx E$ and $t_S \approx C$. Thus we can conclude that when the system is in a regime where almost all of its enzyme is free and almost all of its substrate is bound (which in turn implies that there is an excess of enzyme), that the system is saturated against additional enzyme concentration but does respond linearly to the addition of more substrate.

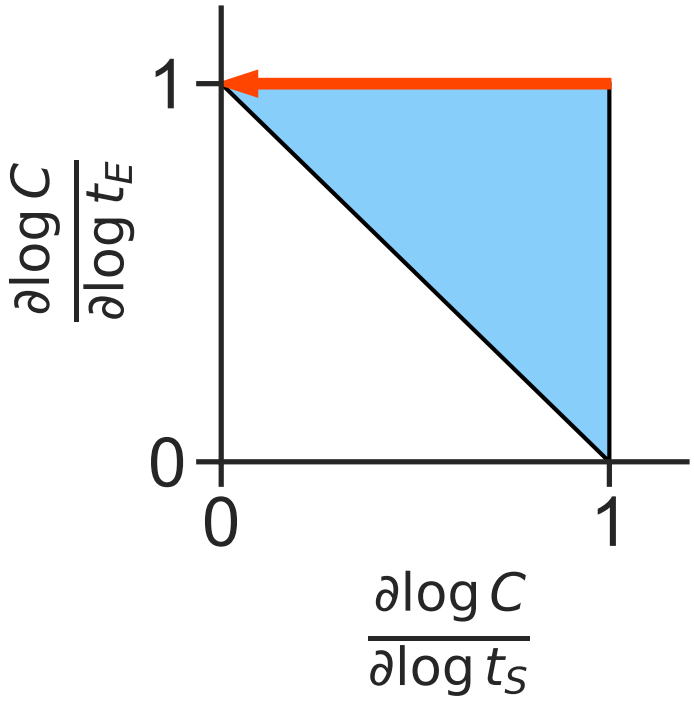

Figure 3.2: The Michaelis-Menten approximation for Model 3.3, $C \approx t_E \frac{t_S}{t_S+K}$, overlaid on the reaction order polytope of C from Figure 3.1 as a red arrow. The direction of the arrow indicates the movement of the system in reaction order space as t_S increases.

This situation operates under the identical intuition to the conventional notion of enzyme saturation that occurs at the $(0, 1)$ vertex (and when the Michaelis-Menten approximation enters a regime where t_S is large). Considering that our model treats the enzyme and substrate identically, so that swapping their labels does not impact the model's behavior, this result is unsurprising. However, it does suggest the connection between vertices in reaction order space and regimes in concentration space, which we will exploit in the next section.

3.3 A scalable procedure for finding the reaction order polytope

While Equation 3.8 is always technically solvable for systems of any size, the inversion of a large matrix is not realistically feasible to perform manually. Even with computerized assistance from symbolic algebraic packages, the resulting functional forms for the log derivatives can quickly become uninterpretable. However, the analysis presented in Section 3.2 shows that many of the insights that arise from the reaction order framework arise from the geometric object of the polytope itself as their basis, rather than the exact functional forms of the log derivatives. We therefore

reasoned that if we could find a more practical procedure to exactly generate the polytope, specifically its vertices and edges, then our framework could be easily applied to more complex systems.

Based on our analysis of model 3.3 in the previous section, we conjectured that the vertices of the reaction order polytope would correspond to extreme regions of concentration space, where each of the totals is dominated by a single component species. By finding all such 'dominance regimes' in concentration space for a given system and mapping those regimes into reaction order space, we predicted that we would find all of the vertices of the reaction order polytope. From there, we could map the connections that exist naturally between the dominance regimes in concentration space into connections in reaction order space in order to obtain the edges of the reaction order polytope.

The procedure to generate the vertices and edges in this way is given below. A derivation and more thorough explanation for this procedure is given in Appendix B.

Calculating reaction order vertices and edges

1. **Write down the system's architecture.** Based on the given network of binding reactions, write down the conservation law matrix $\boldsymbol{L}$ and the stoichiometric matrix $\boldsymbol{N}$.

2. **Find the dominance regimes.** Generate all possible candidate dominance regimes by converting $\boldsymbol{L}$ to $\widetilde{\boldsymbol{L}}$ by setting all nonzero elements to 1, and then calculating the set of all $\widetilde{\boldsymbol{L}}$ variants where all but one of its nonzero entries is set to zero in each row. Call this set of matrices $\{\boldsymbol{A}\}$.

    - For each dominance matrix $\boldsymbol{A}$, check that it does not imply an internally inconsistent ordering of the species concentrations. This can occur if e.g. two rows of $\boldsymbol{L}$ share two species ($t_i = x_1+x_2+x_3$ and $t_j = x_2+x_3+x_4$) and $\boldsymbol{A}$ has different choices of dominant species within this shared set ($t_i \approx x_2$ and $t_j \approx x_3$, implying both $x_2 \gg x_3$ and $x_3 \gg x_2$ simultaneously). Throw out such inconsistent $\boldsymbol{A}$ matrices.

3. **Find the edges between dominance regimes.** For the remaining $\boldsymbol{A}$ matrices, find all pairs of matrices that differ only by a rank-1 change, i.e. differ only in a single row. Call the matrices within such a pair connected.

4. **Find the finite reaction order vertices.** Now append $\boldsymbol{N}$ onto the bottom rows of each $\boldsymbol{A}$ matrix to create a set of $\boldsymbol{M}$ matrices. Invert all invertible $\boldsymbol{M}$ matrices to obtain the corresponding finite reaction order vertices $\boldsymbol{H}$.

5. **Find the infinite reaction order vertices.** If $\boldsymbol{M}$ is not invertible, then its corresponding reaction order vertex $\boldsymbol{H}$ will be a point at infinity. We will therefore represent $\boldsymbol{H}$ as the endpoint of an infinite ray that points in the direction $\boldsymbol{R}$.

   For each noninvertible $\boldsymbol{M}$ matrix, solve the equation $\boldsymbol{M}\widetilde{\boldsymbol{R}} = \boldsymbol{0} = \widetilde{\boldsymbol{R}}\boldsymbol{M}$ to obtain a candidate ray matrix $\widetilde{\boldsymbol{R}}$. Then find an invertible dominance matrix $\boldsymbol{M}_f$ that is connected to the noninvertible matrix $\boldsymbol{M}$. Check whether the sign of $\det\left(M_f^{-1} + \tau\widetilde{\boldsymbol{R}}\right)$ is equal to the sign of $\det\begin{bmatrix}\boldsymbol{L}\\ \boldsymbol{N}\end{bmatrix}$ for a positive value of τ. If so, then $\widetilde{\boldsymbol{R}}$ and the true ray matrix $\boldsymbol{R}$ share the same direction, and the reaction order vertex associated with $\boldsymbol{M}$ is $\boldsymbol{H} = \lim_{\tau\to\infty}\left(\boldsymbol{M}_f^{-1} + \tau\widetilde{\boldsymbol{R}}\right)$. If not, then $\widetilde{\boldsymbol{R}}$ points in the opposite direction to the true ray matrix $\boldsymbol{R}$ so the reaction order vertex associated with $\boldsymbol{M}$ is $\boldsymbol{H} = \lim_{\tau\to\infty}\left(\boldsymbol{M}_f^{-1} - \tau\widetilde{\boldsymbol{R}}\right)$.

6. **Find the reaction order edges.** Linearly connect all reaction order vertices $\boldsymbol{H}$ according to the connectivity of their associated dominance matrices $\boldsymbol{M}$, as determined in step 3.

Illustrative example: Substrate inhibition

We will now walk through the above procedure for the simple single-enzyme single-substrate system, Model 3.3, reproduced below:

$$E + S \rightleftharpoons C \tag{3.3}$$

Recall that the conservation law matrix is

$$\boldsymbol{L} = \begin{matrix} \\ t_E \\ t_S. \end{matrix}\!\!\begin{matrix} \begin{matrix} E & S & C \end{matrix} \\ \begin{bmatrix} 1 & 0 & 1 \\ 0 & 1 & 1 \end{bmatrix} \end{matrix}$$

Then the dominance regimes are given by

$$\{\boldsymbol{A}_1, \boldsymbol{A}_2, \boldsymbol{A}_3, \boldsymbol{A}_4\} = \left\{\begin{bmatrix}1&0&0\\0&1&0\end{bmatrix}, \begin{bmatrix}0&0&1\\0&1&0\end{bmatrix}, \begin{bmatrix}1&0&0\\0&0&1\end{bmatrix}, \begin{bmatrix}0&0&1\\0&0&1\end{bmatrix}\right\}.$$

Note that none of these matrices are internally inconsistent.

Since the $\boldsymbol{A}$ matrices are small, we can determine their connectivity via rank-1 changes by visual inspection. The edges between these matrices are indicated by

$$\begin{matrix} \boldsymbol{A}_1 & \dots & \boldsymbol{A}_2 \\ \vdots & & \vdots \\ \boldsymbol{A}_3 & \dots & \boldsymbol{A}_4 \end{matrix}$$

with no connection between $(\boldsymbol{A}_1, \boldsymbol{A}_4)$ or between $(\boldsymbol{A}_2, \boldsymbol{A}_3)$.

It now remains to map the dominance regimes to reaction order space. By appending $\boldsymbol{N} = \begin{bmatrix} 1 & 1 & -1 \end{bmatrix}$ onto each $\boldsymbol{A}$ matrix, we obtain

$$\{\boldsymbol{M}_1, \boldsymbol{M}_2, \boldsymbol{M}_3, \boldsymbol{M}_4\} = \left\{ \begin{bmatrix} 1 & 0 & 0 \\ 0 & 1 & 0 \\ 1 & 1 & -1 \end{bmatrix}, \begin{bmatrix} 0 & 0 & 1 \\ 0 & 1 & 0 \\ 1 & 1 & -1 \end{bmatrix}, \begin{bmatrix} 1 & 0 & 0 \\ 0 & 0 & 1 \\ 1 & 1 & -1 \end{bmatrix}, \begin{bmatrix} 0 & 0 & 1 \\ 0 & 0 & 1 \\ 1 & 1 & -1 \end{bmatrix} \right\}.$$

Only $\boldsymbol{M}_4$ is singular, so for $\boldsymbol{M}_1, \boldsymbol{M}_2, \boldsymbol{M}_3$ we can simply invert them to obtain $\boldsymbol{H}_1, \boldsymbol{H}_2, \boldsymbol{H}_3$.

In order to determine $\boldsymbol{H}_4$, we will first find an invertible dominance vertex that is connected to $\boldsymbol{M}_4$. We will choose $\boldsymbol{M}_3$, although $\boldsymbol{M}_2$ would work equivalently. By solving $\boldsymbol{M}_4 \widetilde{\boldsymbol{R}} = \boldsymbol{0} = \widetilde{\boldsymbol{R}} \boldsymbol{M}_4$, we obtain

$$\widetilde{\boldsymbol{R}} = \begin{bmatrix} 1 & -1 & 0 \\ -1 & 1 & 0 \\ 0 & 0 & 0 \end{bmatrix},$$

as a valid solution to this equation, noting that any scalar multiple of $\widetilde{\boldsymbol{R}}$ would also be a valid solution.

We will now perform the sign check on $\widetilde{\boldsymbol{R}}$. Since $\det \begin{bmatrix} \boldsymbol{L} \\ \boldsymbol{N} \end{bmatrix} = -3$, we must have $\operatorname{sgn} \det \left(\boldsymbol{M}_3^{-1} + \tau \widetilde{\boldsymbol{R}} \right) < 0$ for $\tau > 0$. Setting $\tau = 1$, we obtain

$$\det \left(\boldsymbol{M}_3^{-1} + \widetilde{\boldsymbol{R}} \right) = \det \begin{bmatrix} 2 & -1 & 0 \\ -2 & 2 & 1 \\ 0 & 1 & 0 \end{bmatrix} = -2.$$

Since the signs of the determinants are consistent, we can take our true ray matrix $\boldsymbol{R}$ to be $\widetilde{\boldsymbol{R}}$ directly.

The final set of vertices for the reaction order polytope is therefore

$$\{\boldsymbol{H}_1, \boldsymbol{H}_2, \boldsymbol{H}_3\} = \left\{ \begin{bmatrix} 1 & 0 & 0 \\ 0 & 1 & 0 \\ 1 & 1 & -1 \end{bmatrix}, \begin{bmatrix} 1 & -1 & 1 \\ 0 & 1 & 0 \\ 1 & 0 & 0 \end{bmatrix}, \begin{bmatrix} 1 & 0 & 0 \\ -1 & 1 & 1 \\ 0 & 1 & 0 \end{bmatrix} \right\},$$

$$\boldsymbol{H}_4 = \lim_{\tau \to \infty} \boldsymbol{H}_2 + \tau \begin{bmatrix} 1 & -1 & 0 \\ -1 & 1 & 0 \\ 0 & 0 & 0 \end{bmatrix} = \lim_{\tau \to \infty} \boldsymbol{H}_3 + \tau \begin{bmatrix} 1 & -1 & 0 \\ -1 & 1 & 0 \\ 0 & 0 & 0 \end{bmatrix},$$

and the edges between them are indicated by the diagram

$$\begin{array}{ccc} \boldsymbol{H}_1 & - & \boldsymbol{H}_2 \\ | & & | \\ \boldsymbol{H}_3 & - & \boldsymbol{H}_4 \end{array}$$

Recall that the entries of these $\boldsymbol{H}$ matrices have the interpretation

$$\boldsymbol{H} = \begin{bmatrix} \frac{\partial \log E}{\partial \log t_E} & \frac{\partial \log E}{\partial \log t_S} & \frac{\partial \log E}{\partial \log K} \\ \frac{\partial \log S}{\partial \log t_E} & \frac{\partial \log S}{\partial \log t_S} & \frac{\partial \log S}{\partial \log K} \\ \frac{\partial \log C}{\partial \log t_E} & \frac{\partial \log C}{\partial \log t_S} & \frac{\partial \log C}{\partial \log K} \end{bmatrix}.$$

We can now plot these vertices and edges directly, which we do for the reaction order of C and E in Figure 3.3.

The reaction order polytopes for C and E differ in their properties, including whether they are bounded and the number of finite vertices. This is a common property of the reaction order polytopes, where slicing out a row of the $\boldsymbol{H}$ matrices to look at the sensitivity of a particular active species collapses different $\boldsymbol{H}$ matrices onto the same point in the projection. For the E polytope, the $\boldsymbol{H}_1$ and $\boldsymbol{H}_3$ vertices both occupy the same point. For the C polytope, the ray matrix associated with the infinite vertex $\boldsymbol{H}_4$ has zero direction, meaning it does not move. This means that $\boldsymbol{H}_4$ simultaneously occupies two positions in reaction order space: it is coincident with both $\boldsymbol{H}_2$ and $\boldsymbol{H}_3$, which are distinct points. Interestingly, this means that in the C polytope, there is in practice a direct connection between $\boldsymbol{H}_2$ and $\boldsymbol{H}_3$ via $\boldsymbol{H}_4$ despite the fact that the associated dominance matrices $\boldsymbol{M}_2$ and $\boldsymbol{M}_3$ are not connected by a rank-1 change.

3.4 Functional benefits of cooperativity

Having demonstrated the underlying procedures associated with performing reaction order analysis, we will now demonstrate its utility in revealing biological insights.

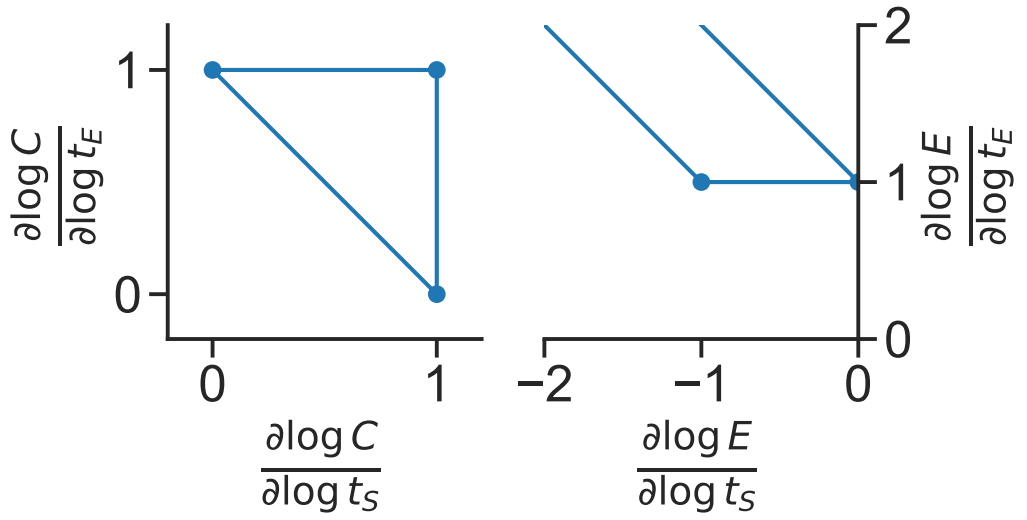

Figure 3.3: Exact calculation of the vertices and edges of the reaction order polytope obtained from Model 3.3. (Left) the polytope for C, corresponding to the third row of the $\boldsymbol{H}$ matrices. (Right) the polytope for E, corresponding to the first row of the $\boldsymbol{H}$ matrices. The $\boldsymbol{H}_4$ vertex lies at infinity in the $[-1, +1]$ direction from the finite vertices.

We will first ask the question of what functional benefits are gained when a system exhibits cooperativity.

Consider a slight modification to our single-enzyme single-substrate model that now allows two copies of the substrate to bind to the enzyme. Our system will therefore be governed by the reactions

$$\begin{aligned} E + S &\rightleftharpoons C_1 \\ C_1 + S &\rightleftharpoons C_2, \end{aligned} \tag{3.10}$$

where for simplicity we do not distinguish between the two sites on the enzyme. Because this system consolidates two possible molecular states into a single C_1 species, we will write the dissociation constant of the first reaction as $2K_1$ and the dissociation constant of the second reaction as $K_2/2$ in order to properly account for the stoichiometry [8].

Model 3.10 exhibits cooperativity when the affinities of the two reactions are not equal, i.e. $4K_1 \neq K_2$. Specifically, this cooperativity is negative when $4K_2 > K_2$, indicating that the binding of the first substrate molecule inhibits the binding of the second. When $4K_1 > K_2$, this cooperativity is positive, as the binding of first substrate molecule promotes the binding of the second. In fact, in the limit of infinite

positive cooperativity, the system simplifies to

$$E + 2S \rightleftharpoons C_2, \tag{3.11}$$

where the affinity of the second binding event is so high that it occurs instantaneously alongside the first. An analogous reduced system for infinitely negative cooperativity is not well-defined, as that would mean the occurrence of the first binding event would preclude the occurrence of the second, preventing the system from ever reaching its active state C_2.

In 2016, Ha and Ferrell published a study that analyzed the system presented in network 3.10, and found that the concentration of C_2 can respond ultrasensitively with reaction order > 2 to the total substrate concentration when the system exhibits negative cooperativity [8]. The shocking significance of this work is that, despite the fact that many mathematical biologists (including Ferrell) had spent decades studying ultrasensitivity and cooperativity in biomolecular reaction systems [9–12], it was not until 2016 that this behavior was noticed, let alone arising from such a simple model.

The reason this behavior was overlooked for so long is because the impact of total species concentrations, rather than free species concentrations, is extremely difficult to analyze directly, as illustrated in Section 3.2. Ha and Ferrell had to invoke a number of simplifying assumptions in order to obtain expressions for C_2 as a tractable function of $t_S = S+C_1+2C_2$. As a consequence, although they were able to demonstrate that negatively-cooperative systems can exhibit strong ultrasensitivity, their analysis does not rule out the possibility of positively-cooperative systems also exhibiting such strong ultrasensitivity, but outside of the regimes where their approximations are valid.

Because ultrasensitivity is a system property that is very naturally expressed in the language of reaction order (in fact, the definition of ultrasensitivity is having reaction order > 1), we applied our reaction order analysis framework to this system. Doing so just involves following the procedure described in section 3.3, with the additional step of confirming that the initial set of dominance regimes do not contradict the K constraints associated with a particular cooperativity condition. Briefly, the process is as follows.

First, we write down our two conserved quantities $t_E = E + C_1 + C_2$ and $t_S =$

$S + C_1 + 2C_2$ and collect them in a conservation law matrix

$$\boldsymbol{L} = \begin{array}{c} \begin{matrix} E & S & C_1 & C_2 \end{matrix} \\ \begin{bmatrix} 1 & 0 & 1 & 1 \\ 0 & 1 & 1 & 2 \end{bmatrix} \end{array} \begin{matrix} t_E \\ t_S. \end{matrix}$$

We also write down our stoichiometric matrix

$$\boldsymbol{N} = \begin{array}{c} \begin{matrix} E & S & C_1 & C_2 \end{matrix} \\ \begin{bmatrix} 1 & 1 & -1 & 0 \\ 0 & 1 & 1 & -1 \end{bmatrix} \end{array} \begin{matrix} K_1 \\ K_2. \end{matrix}$$

Since the two conserved quantities share two species (C_1 and C_2), some of the $\boldsymbol{A}$ matrices generated from $\boldsymbol{L}$ will be internally inconsistent. Removing these, we have the set

$$\{\boldsymbol{A}\} = \left\{ \begin{bmatrix} 1 & 0 & 0 & 0 \\ 0 & 1 & 0 & 0 \end{bmatrix}, \begin{bmatrix} 1 & 0 & 0 & 0 \\ 0 & 0 & 1 & 0 \end{bmatrix}, \begin{bmatrix} 1 & 0 & 0 & 0 \\ 0 & 0 & 0 & 1 \end{bmatrix}, \right.$$
$$\left. \begin{bmatrix} 0 & 0 & 1 & 0 \\ 0 & 1 & 0 & 0 \end{bmatrix}, \begin{bmatrix} 0 & 0 & 1 & 0 \\ 0 & 0 & 1 & 0 \end{bmatrix}, \begin{bmatrix} 0 & 0 & 0 & 1 \\ 0 & 1 & 0 & 0 \end{bmatrix}, \begin{bmatrix} 0 & 0 & 0 & 1 \\ 0 & 0 & 0 & 1 \end{bmatrix} \right\}.$$

Note that the 2 in the bottom-right entry of $\boldsymbol{L}$ has become a 1 value for the $\boldsymbol{A}$ matrices because this entry in the $\boldsymbol{A}$ matrices represents the asymptotic relation $t_S \approx C_2$.

If we assign each $\boldsymbol{A}$ matrix above with an integer label corresponding to the order in which it appears above, then we can visualize their connectivity as

$$\begin{array}{ccccc} \boldsymbol{A}_4 & \cdots & \boldsymbol{A}_5 & \cdots & \boldsymbol{A}_2 \\ \vdots & \ddots & & \iddots & \vdots \\ \vdots & & \boldsymbol{A}_1 & & \vdots \\ \vdots & \iddots & & \ddots & \vdots \\ \boldsymbol{A}_6 & \cdots & \boldsymbol{A}_7 & \cdots & \boldsymbol{A}_3 \end{array}$$

From this set $\{\boldsymbol{A}\}$, each cooperativity condition will imply an additional set of $\boldsymbol{A}$ matrices that must be removed. For example, the dominance regime $\boldsymbol{A}_3$ corresponds to $(t_E, t_S) \approx (E, C_2)$ and is not feasible for the noncooperative regime. This is because $t_E \approx E$ implies $K \gg S$ and because $t_S \approx C_2$ implies $S \gg K$, which cannot simultaneously be true. However, this contradiction disappears when the K_1 and K_2 values are allowed to vary independently in the conditions with nonzero cooperativity.

When a particular matrix $\boldsymbol{A}_i$ is removed, all of its neighbors become directly connected to each other, so as not to allow isolated vertices from existing. For example, if $\boldsymbol{A}_3$ were removed as above, then new direct connections would form between $(\boldsymbol{A}_2, \boldsymbol{A}_7)$ and between $(\boldsymbol{A}_1, \boldsymbol{A}_7)$.

Once $\{\boldsymbol{A}\}$ has been fully pruned for each cooperativity condition, the rest of the procedure given in Section 3.3 can be followed directly. Doing so and plotting the C_2 polytope yields the following result.

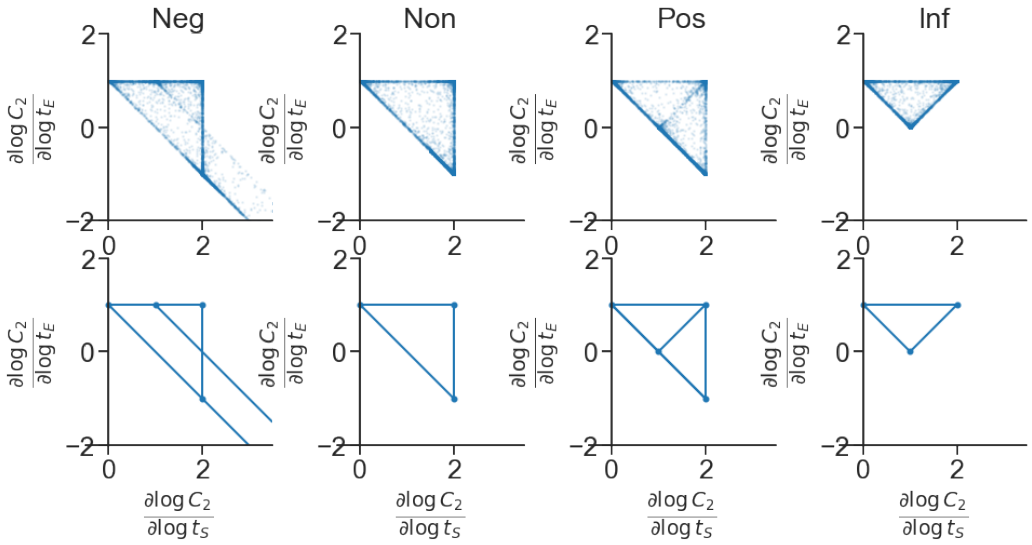

Figure 3.4: Reaction order polytopes for C_2 from Model 3.10 for Negative Cooperativity ($4K_1 < K_2$), Noncooperativity ($4K_1 = K_2$), Positive Cooperativity ($4K_1 > K_2$), and Infinite Positive Cooperativity. (Top row) Numerical solution obtained by sampling 10,000 log-uniformly distributed values of E, S, K_1, K_2 between 10^{-6} and 10^{6} (subject to the appropriate cooperativity constraints) and directly calculating the specific $\boldsymbol{H}$ value from inversion of the matrix in Equation 3.8. (Bottom row) Exact calculation of the reaction order vertices and edges.

Visual inspection of Figure 3.4 immediately reveals that the negatively-cooperative system can indeed exhibit ultrasensivity to t_S with order > 2, reproducing the result of Ha and Ferrell. Furthermore, because the reaction order polytopes capture every possible system state, Figure 3.4 shows that negative cooperativity is *necessary* for ultrasensitivity of order > 2. We additionally find that the ultrasensitivity of negatively-cooperative systems can become arbitrarily large, since the polytope stretches towards a vertex that lies at infinity, while Ha and Ferrell's approximate model only exhibited ultrasensitivity up to order 8.

Ha and Ferrell also noted that all system variants except those with infinite positive cooperativity (including the noncooperative condition) could experience a biphasic response to t_E, where the concentration of C_2 first rises with increasing t_E but then shifts to falling when additional t_E is added [8]. The authors note that this is a general phenomenon that emerges from increasing t_E driving mass from the active C_2 state into the inactive C_1 state, and has been observed in the prozone effect for antigen-antibody interactions and transcriptional squelching [13]. Visual inspection of Figure 3.4 also demonstrates this possibility, as inhibition of C_2 by t_E is represented by a negative reaction order. By transitioning from a vertex with $\frac{\partial \log C_2}{\partial \log t_E} > 0$ to one with $\frac{\partial \log C_2}{\partial \log t_E} < 0$, the system would undergo such a biphasic response.

Finally, a key implication of the Ha and Ferrell study is that all of these behaviors only emerge when the system responds to total substrate concentration, rather than free substrate concentration. Representing the system as responding to free substrate concentration is equivalent to assuming that the substrate is in great excess compared to the enzyme [8], which itself implies that the signal will exist predominantly in the forms where it is not bound to enzyme. Because the only such form is the free form S, this is equivalent to the assumption $t_S \approx S$.

We can use the reaction order framework to analyze our model again, this time under the global constraint of satisfying the excess-substrate assumption $t_S \approx S$. We can implement this by using a modified $\boldsymbol{L}$ matrix where the conserved quantity $t_S = S + C_1 + 2C_2$ is replaced by $t_S = S$, via

$$\boldsymbol{L}_S = \begin{bmatrix} 1 & 0 & 1 & 1 \\ 0 & 1 & 0 & 0 \end{bmatrix}$$

at the beginning of our analysis procedure.

After performing the analysis, we can see that both the ability for ultrasensitivity to S of order > 2 and the ability for C_2 to be inhibited by t_E disappear in all cooperativity conditions (Figure 3.5).

While it is encouraging to demonstrate that our reaction order framework can easily and visually reproduce and generalize the results from the sophisticated analyses performed by Ha and Ferrell, we can additionally reveal novel insights into the functional benefits of cooperativity. Returning to Figure 3.4, we see that all conditions with a nonzero cooperativity contain a vertex at $\frac{\partial \log C_2}{\partial \log t_S} = 1$. Because all of the possible dominance regimes map to reaction order vertices, the absence of a vertex

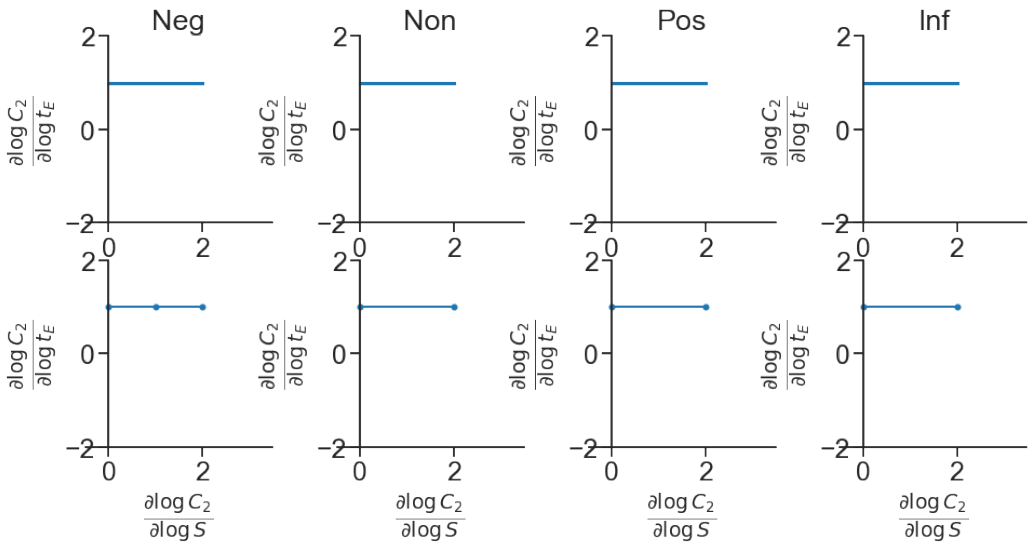

Figure 3.5: Reaction order polytopes for C_2 from Model 3.10 for Negative Cooperativity ($4K_1 < K_2$), Noncooperativity ($4K_1 = K_2$), Positive Cooperativity ($4K_1 > K_2$), and Infinite Positive Cooperativity, this time assuming $t_S \approx S$ in all cases. (Top row) Numerical solution obtained by sampling 10,000 log-uniformly distributed values of E, S, K_1, K_2 between 10^{-6} and 10^6 (subject to the appropriate cooperativity constraints) and directly calculating the specific $\boldsymbol{H}$ value from inversion of the matrix in Equation 3.8. (Bottom row) Exact calculation of the reaction order vertices and edges.

at $\frac{\partial \log C_2}{\partial \log t_S} = 1$ in the noncooperative condition implies that the system cannot achieve linear sensitivity to t_S by pushing its own state into a dominance regime– instead, the system must stably hold its configuration at an intermediate position between two dominance regimes.

We argue that, in general, it is easier to control a biomolecular system to maintain its state at a dominance regime than it is to maintain its state at some other region of concentration space. This is because dominance regimes are robust to 'overshooting' the goal– because they are defined by asymptotic relations, whether the inequalities hold by e.g. 100-fold or 1000-fold does not significantly affect the system's position in reaction order space.

As such, we can claim that an additional functional property conferred by cooperativity, regardless of its sign, is the ability for the system to reliably maintain linear sensitivity to its substrate. This confers a flexibility onto the system, allowing it to change its configuration to choose between responding with either order-2 sensitivity or order-1 sensitivity. In contrast, the noncooperative system only has reaction

order vertices corresponding to zero sensitivity to substrate or order-2 sensitivity to the substrate, providing an 'all-or-none' type behavior in the order of its response to substrate.

We can therefore summarize our results about the functional consequences of cooperativity:

- All systems can respond with order-2 sensitivity to t_S at a dominance regime, but nonzero cooperativity, regardless of the sign, additionally allows the system to achieve order-1 sensitivity to t_S at a dominance regime. Thus, cooperativity provides flexibility in how the system responds to its substrate.
- When this cooperativity is negative, the system is able to achieve an ultrasensitive (order > 2) response to t_S. However, the regimes that generate this ultrasensitive response must necessarily also exhibit inhibition by t_E. The order of this inhibition increases proportionally to the order of the t_S response.
- More generally, inhibition by t_E is a property of all cooperative systems that is only alleviated in the limit of infinite positive cooperativity.

3.5 Activators and repressors can achieve unique behaviors

Having demonstrated that reaction order analysis can successfully reproduce and generalize insights from a previously-studied system, we will now demonstrate that reaction order analysis can generate wholly novel insights into biomolecular system behavior. To do this, we will focus on another classic question in systems biology, which is the distinction between activators and repressors in allosteric transcriptional regulation.

To implement a transcriptional regulation system that will activate gene expression in response to a signal molecule, a cell has two broad categories of options. It could either regulate its gene with an activator whose activity is enabled by the presence of the signal, or it could regulate its gene with a repressor whose activity is inhibited by the signal. The question of why some genes are regulated by the former motif and some genes are regulated by the latter has been a long-standing question.

A notable hypothesis was put forward by Michael Savageau in the 1970s, called the Demand Theory [14–17]. The Demand Theory uses an evolutionary selection argument to suggest that genes in high demand (genes that are actively expressed most of the time) should be regulated by activators, while genes in low demand

(genes that are expressed infrequently) should be regulated by repressors. The rationale is that under this regulation scheme, loss-of-function mutations in the regulators would have immediate fitness consequences to the mutant cells, quickly pruning them from the population. In contrast, under the converse regulation scheme where high-demand genes are regulated by repressors and low-demand genes are regulated by activators, a mutation in e.g. an activator would have minimal fitness effect because the low-demand genes are generally not being activated anyway. This allows the mutants to propagate within the population under standard conditions, making the population as a whole less able to withstand the rare events when the regulation is actually needed.

While follow-up work by other authors [18] has demonstrated that this evolutionary argument can, depending on the specific parameter values involved, lead to either the Demand Rule or its opposite prescription, this negative selection mindset has remained prominent in the field's thinking. Even alternative hypotheses that invoke different molecular mechanisms, such as reducing erroneous, nonspecific binding to operator sites [19], still take the same fundamental assumption that the two architectures differ in how they fail, rather than in any potential distinctions in the types of behaviors each can perform. To our knowledge, such a 'positive selection' hypothesis to explain the different usage patterns of the two architectures has not yet been proposed.

Because reaction order analysis reveals a system's possible behaviors across all possible system configurations, our framework is well-placed to determine whether such a distinction exists between activators and repressors. We first wrote down a simple model of inducible transcriptional regulation, where a regulator R can bind to both its target gene G and its signal S.

$$\begin{aligned} G + R &\rightleftharpoons G_R, \\ R + S &\rightleftharpoons R_S, \\ G + R_S &\rightleftharpoons G_{RS}, \\ G_R + S &\rightleftharpoons G_{RS}. \end{aligned} \tag{3.12}$$

Different choices of regulatory architecture correspond to different choices of active species in model 3.12. For a repressor architecture, the active species is the unbound gene, G. There are two possible implementations of the activator architecture: in an action-modulated system, the transcriptional activation comes specifically from the signal-regulator complex R_S and so the active species is G_{RS}. An example

of such a system is the E. coli arabinose operon regulator AraC, which does not activate transcription when bound to its target gene unless it is bound to its inducer arabinose [20]. In a binding-modulated system, the mechanism of transcriptional activation is intrinsic to the regulator, and the signal's role is just to incentivize the regulator's binding to its target gene. If the regulator did bind to the gene without the signal bound, however, it would still activate transcription, so the system's activity is the sum of the activity from two states, $G_R + G_{RS}$. The quorum sensing activator LuxR [21] could potentially operate in this way, as the generation of LuxR mutants that activate transcription in the absence of inducer suggest the possibility that the inducer might act to encourage, rather than enable, transcriptional activation in the natural system [22, 23].

In addition to the choices of active species, the different architectures carry different constraints on their binding affinities in order to ensure that the regulatory logic is consistent. In all cases, it should be the case that the system's activity increases with the addition of signal– otherwise, it is not fulfilling its fundamental purpose as a signal response system. In the case of the repressor architecture, this means that the signal must act as an antagonist for regulator-gene binding, meaning that R_S should be less likely to bind to G than R. This manifests as a constraint $K_{R+G} < K_{R_S+G}$. For both activator architectures, the signal must act as an agonist for receptor-gene binding, corresponding to the condition $K_{R+G} > K_{R_S+G}$.

Having specified our definitions for each architecture, we are now ready to analyze Model 3.12 using reaction order analysis. There are three conserved quantities in this system, which yield the $\boldsymbol{L}$ matrix

$$\begin{array}{c} \\ \boldsymbol{L} = \end{array} \begin{array}{c} \begin{array}{cccccc} G & R & S & G_R & R_S & G_{RS} \end{array} \\ \begin{bmatrix} 1 & 0 & 0 & 1 & 0 & 1 \\ 0 & 1 & 0 & 1 & 1 & 1 \\ 0 & 0 & 1 & 0 & 1 & 1 \end{bmatrix} \end{array} \begin{array}{c} t_G \\ t_R \\ t_S. \end{array}$$

Model 3.12 also contains a cycle, so one of the four K values is dependent on the other three. We will designate K_{G_R+S} as this redundant variable, and obtain

$$\begin{array}{c} \\ \boldsymbol{N} = \end{array} \begin{array}{c} \begin{array}{cccccc} G & R & S & G_R & R_S & G_{RS} \end{array} \\ \begin{bmatrix} 1 & 1 & 0 & -1 & 0 & 0 \\ 0 & 1 & 1 & 0 & -1 & 0 \\ 1 & 0 & 0 & 0 & 1 & -1 \end{bmatrix} \end{array} \begin{array}{c} K_{G+R} \\ K_{R+S} \\ K_{G+R_S}. \end{array}$$

From these matrices we can calculate the reaction order polytopes by following the procedure outlined in Section 3.3, and applying the vertex removal procedure described in Section 3.4 for the inducer agonism constraints associated with each architecture.

Having obtained the reaction order vertices $\{\boldsymbol{H}\}$, one simply needs to plot the appropriate rows to obtain the reaction order polytopes for the Repressor (active species G) and the Action-modulated Activator (active species G_{RS}). For the Binding-modulated Activator, however, where the active species is the sum G_R+G_{RS}, it is necessary to take a weighted sum of two rows of $\boldsymbol{H}$. Based on the general formula for the log derivative of a sum (Appendix A), we have that

$$\frac{\partial \log(G_R + G_{RS})}{\partial \log \boldsymbol{t}, \boldsymbol{k}} = \frac{G_R}{G_R + G_{RS}} \frac{\partial \log G_R}{\partial \log \boldsymbol{t}, \boldsymbol{k}} + \frac{G_{RS}}{G_R + G_{RS}} \frac{\partial \log G_{RS}}{\partial \log \boldsymbol{t}, \boldsymbol{k}}. \tag{3.13}$$

The implication of Equation 3.13 is that, when the active state is a sum of more than one species, a single dominance regime can map to multiple points in reaction order space– specifically, it maps to a line segment connecting two vertices (the G_R vertex and the G_{RS} vertex) and the relative dominance of G_R and G_{RS} determines whether the system is in one vertex or the other. However, we note that some dominance regimes will constrain the relationship between G_R and G_{RS}, either by directly specifying that one dominates the other, or by generating an internal contradiction when a particular $G_R \sim G_{RS}$ dominance is asserted. In these cases the reaction order is not free to vary and remains fixed at the valid vertex.

With this final consideration addressed, we are now able to visualize the reaction order polytopes for our three regulatory architectures (Figure 3.6). We immediately notice that the repressor architecture is able to exhibit ultrasensitivity to t_S, while neither activator architecture can. We can additionally see that both activator architectures are able to respond with order-1 sensitivity to t_S while being robust to t_G (i.e. $\frac{\partial \log G^*}{\partial \log t_G} = 0$, with G^* the active species), while the repressor can never have a sensitivity to t_G lower than 1. These represent biologically-useful behaviors that are uniquely accessible by each regulatory architecture.

By simply looking at the reaction order polytopes, we have already obtained the basis for a potential positive selection hypothesis for why some genes are regulated by repressors and some by activators. A natural follow-up question is to ask how these behaviors arise. By tracing back the dominance vertices associated with the relevant reaction order vertices, we can determine the conditions on $\boldsymbol{x}$ that push the system into the regimes that exhibit the relevant behaviors.

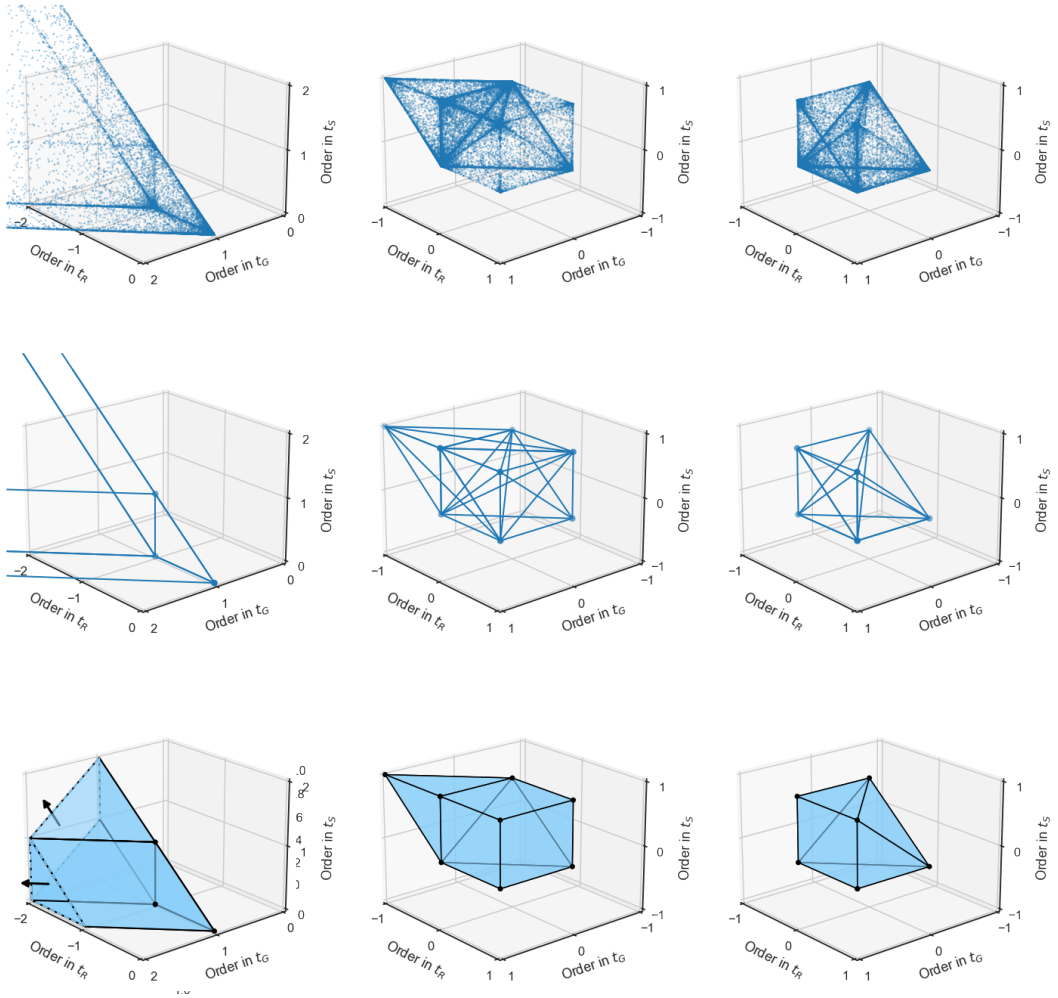

Figure 3.6: Reaction order polytopes for Repressor (left column), Action-modulated Activator (middle column), and Binding-modulated Activator (right column) architectures based on Model 3.12. (Top row) Numerical solution based on 10,000 log-uniformly sampled values of $E, R, S, K_{G+R}, K_{R+S}, K_{G+R_S}$ that were then pruned to remove points that violated the inducer (ant)agonism constraints associated with each architecture. (Middle row) Exact calculations of the reaction order vertices and edges. (Bottom row) A visual representation of the three-dimensional space occupied by the reaction order polytope. To reduce visual clutter, not all edges between vertices are shown.

Gene copy number robustness in the activators

Figure 3.6 shows that both activator architectures can exhibit order-1 sensitivity to t_S while simultaneously being robust to t_G. These reaction order vertices are, with the syntax $[O_G, O_R, O_S]$ to represent the reaction order values with respect to t_G, t_R, t_S respectively, $[0, 0, 1]$ for the binding-modulated activator and $[0, 0, 1]$, $[0, 1, 1]$ for the action-modulated activator.

By backing out the dominance regimes $\boldsymbol{M}$ associated with each of these reaction order vertices $\boldsymbol{H}$, we can determine the conditions in concentration space that lead to this behavior. For the binding-modulated activator, only a single dominance regime generates the $[0, 0, 1]$ vertex, and it is $(t_G, t_R, t_S) \approx (G, R, G_{RS})$. This implies that the binding affinity of the non-inducer-bound regulator to the DNA, K_{R+G}, is very weak, as free G and free R must both be in excess without coming together to form G_R. Given that G is in excess, changing the gene copy number would not affect the concentration of G_{RS} or G_R, while the fact that all of the signal is bound in G_{RS} form means that it is limiting for G_{RS} formation– increasing the total signal t_S would therefore increase the system's activity via G_{RS} formation.

Similarly, the $[0, 0, 1]$ vertex is obtained in the action-modulated activator by the dominance regimes $(t_G, t_R, t_S) \approx (G, R, G_{RS})$, (G, G_R, G_{RS}), and (G_R, R, G_{RS}). These latter two regimes follow the same intuition– the gene is in excess, so changes to its concentration do not affect the concentration of G_{RS}. Meanwhile, the signal is the limiting factor for G_{RS} formation, so the system responds linearly to changes in t_S. The $[0, 1, 1]$ vertex, which also involves linear sensitivity to t_R and is not attainable by the binding-modulated activator, is obtained by the $(t_G, t_R, t_S) \approx (G, G_R, S)$ regime. Although S is in excess, in this regime the affinities of G_{RS} formation are very low, so changes in t_S still affect the concentration of G_{RS} linearly.

Inhibition by an action-modulated activator

In addition to the $[0, 1, 1]$ vertex, the action-modulated activator also possess a vertex at $[1, -1, 1]$ that is not shared by the binding-modulated activator. Here, the regulator acts with the opposite logic and inhibits the system's activity– this property is unique to the action-modulated activator as the repressor architecture never has positive sensitivity to t_R.

The $[1, -1, 1]$ vertex is generated by a single dominance regime, $(t_G, t_R, t_S) \approx (G_R, R, R_S)$. This dominance regime corresponds to very large t_R, and is always accessible as long as t_R is sufficiently large. This regime, in the binding-modulated

activator architecture, maps to the reaction order vertex $[1, 0, 0]$, meaning it is insensitive to both t_R and t_S there.

In order to better understand how the activator could inhibit G_{RS} at high concentration, we solved the system numerically to obtain the steady-state concentration of each species for various values of t_R (Figure 3.7).

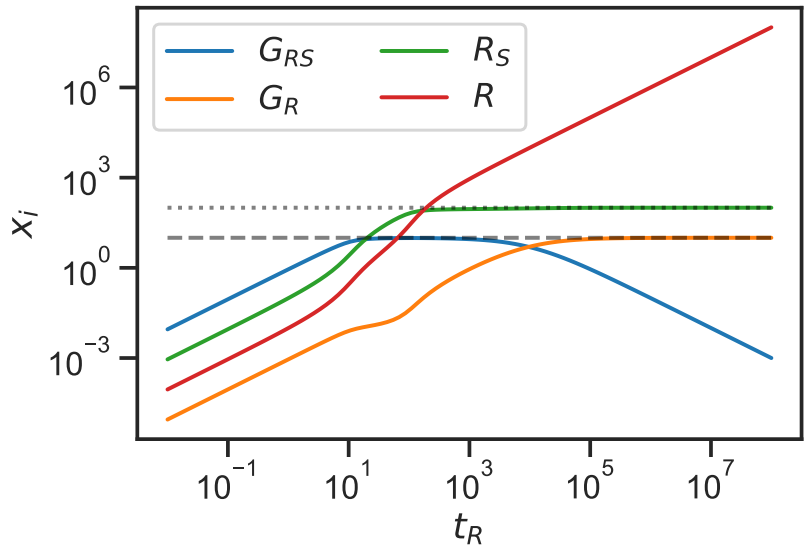

Figure 3.7: Steady-state solution of Model 3.12 as a function of t_R, calculated numerically with arbitrarily-chosen parameters $K_{R+G} = 100$, $K_{R+S} = 10$, $K_{R_S+G} = 1$, $t_G = 10$, $t_S = 100$ that place the system into the appropriate dominance regime. The values of t_G and t_S are marked with dashed and dotted lines, respectively.

We can see that once t_G and t_S both become saturated, any additional t_R entering the system must flow into the free R state. This causes the steady-state concentration of G_{RS} to start decreasing, because when it dissociates into either $G + R_S$ or $G_R + S$, the monomer created is more likely to complex with a free R to form G_R or R_S rather than re-forming G_{RS} because the concentration of R is so high. This tendency is proportional to the concentration of free R, so as it continues to increase with increasing t_R, the steady-state concentration of G_{RS} decreases correspondingly. This is likely a similar situation to the prozone effect-like phenomenon observed for the cooperativity system in Section 3.4 [8, 13].

Figure 3.7 also shows why activity of the binding-modulated activator architecture is robust to t_R in this large t_R regime. Because G_R stays constant, the contribution of G_{RS} to the activity $G_R + G_{RS}$ becomes minuscule, so even though G_{RS} changes with t_R the total activity remains essentially constant.

An interesting coincidence is that action-modulated prokaryotic activators like AraC or NahR tend to act as repressors of their target genes in the absence of their inducer signal [20, 24]. While it is not immediately clear whether the existence of this reaction order vertex is related to this behavior, further investigation into this relationship might be fruitful.

Ultrasensitivity in the repressor

The ultrasensitive response to t_S in the repressor architecture is achieved as the system tends towards the infinite vertex that lies in the $[0, -1, +1]$ direction. This vertex is associated with the dominance regime $(t_G, t_R, t_S) \approx (G_R, R_S, R_S)$.

Ultrasensitive responses are generally associated with 'latch'-like situations, where a signal that was being tightly sequestered into an inactive complex saturates its buffer. This is the situation occurring here, where signal molecules that were being sequestered by free repressors into R_S complexes finally overcome the threshold of t_R and start driving the conversion of G_R into G_{RS} species, which themselves preferentially dissociate into $G + R_S$ rather than $G_R + S$, allowing the concentration of free G (the active species) to rise sharply. This can be seen in the numerical solution given in Figure 3.8.

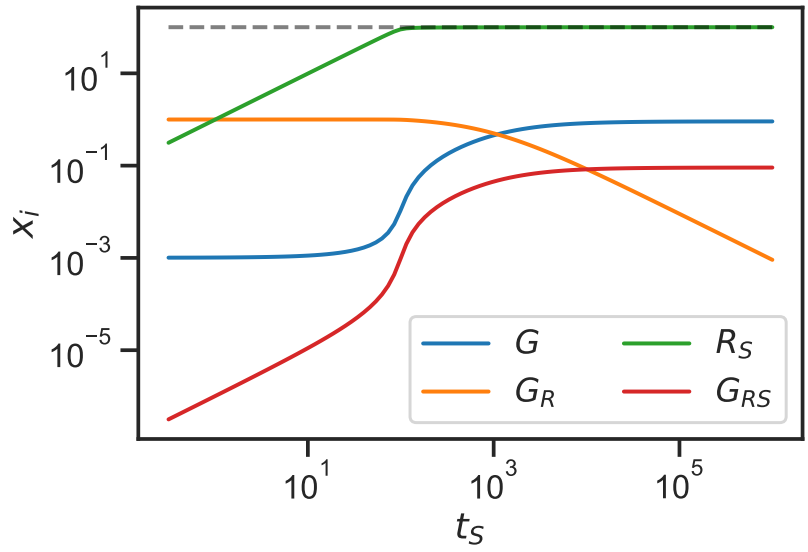

Figure 3.8: Steady-state solution of Model 3.12 as a function of t_S, calculated numerically for $K_{R+G} = 0.1$, $K_{R+S} = 1$, $K_{R_S+G} = 1000$, $t_G = 1$, $t_R = 100$. The value of t_R is marked with a dashed line.

The Michaelis-Menten regime

Given that Model 3.12 is a relatively simple system, a natural question is to ask why (to our knowledge) no previous work had identified these functional distinctions between the behavior of repressors and activators. One potential explanation is that conventional analysis methods use approximations to make the system tractable, and that these approximations do not exhibit these functional distinctions. To assess this claim, we repeated our analysis while constraining the system to stay within the region of concentration space associated with the Michaelis-Menten approximation.

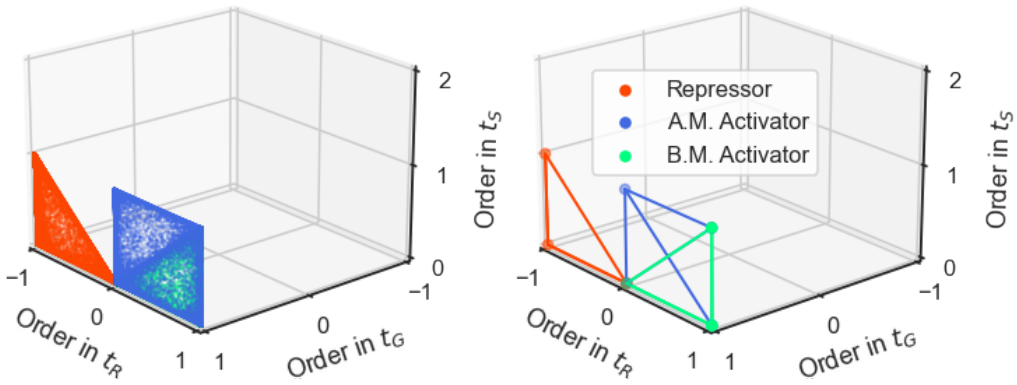

Figure 3.9: Reaction order polytopes for the Repressor, Action-modulated Activator, and Binding-modulated Activator architectures when the Michaelis-Menten assumptions are applied. (Left) Numerical solution from 10,000 log-uniformly distributed values of $G, R, S, K_{G+R}, K_{R+S}, K_{G+R_S}$ subject to the relevant constraints for each architecture. (Right) Exact calculation of the vertices and edges of the reaction order polytopes.

The two major assumptions of the Michaelis-Menten approximation are that the signal exists predominantly in its free state ($t_S \approx S$) and that the regulator exists predominantly in its non-DNA-bound state ($t_R \approx R + R_S$). By writing a new conservation law matrix that takes these approximations as the definitions of these conserved quantities,

$$\boldsymbol{L}_{MM} = \begin{array}{c} \begin{matrix} G & R & S & G_R & R_S & G_{RS} \end{matrix} \\ \begin{bmatrix} 1 & 0 & 0 & 1 & 0 & 1 \\ 0 & 1 & 0 & 0 & 1 & 0 \\ 0 & 0 & 1 & 0 & 0 & 0 \end{bmatrix} \end{array} \begin{matrix} t_G \\ t_R \\ t_S, \end{matrix}$$

we can perform the same analysis procedure and obtain reaction order polytopes that are constrained to always satisfy the Michaelis-Menten assumptions. Doing so

yields the polytopes shown in Figure 3.9.

One can clearly see that the space of functional behaviors for all architectures is heavily reduced under the Michaelis-Menten approximation, and that the interesting behaviors we identified (ultrasensitivity, robustness to gene copy number) are not attainable by these models.

Even more strikingly, we can see that if we plot these polytopes using the absolute value of their sensitivity to t_R (so that activators and repressors can be directly compared despite the differences in their regulatory logic), we see that the polytopes align almost perfectly with each other (Figure 3.10). The only difference is that the Action-modulated Activator has a vertex at $[O_G, O_R, O_S] = [1, 0, 1]$, corresponding to robustness to t_R while maintaining sensitivity to t_S, that is not present in the other two architectures.

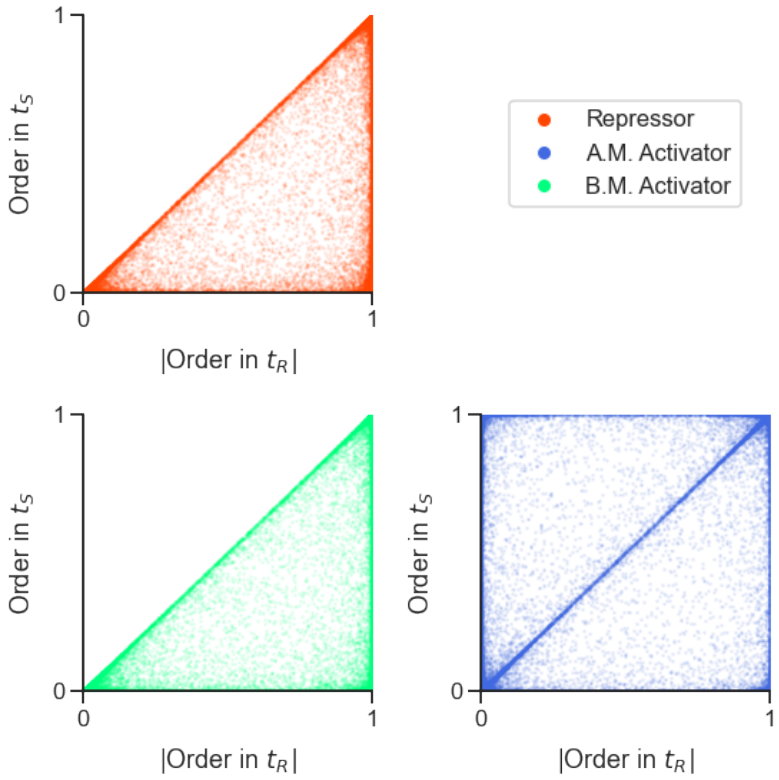

Figure 3.10: Numerically-calculated reaction order polytopes for the Repressor, Action-modulated Activator, and Binding-modulated Activator architectures from Figure 3.9, plotted using the absolute value of the sensitivity to t_R. Polytopes are projected onto a two-dimensional plane because their sensitivity to t_G is always 1 under these conditions.

Figures 3.9 and 3.10 concisely capture the importance of holistic analysis methods that capture the entire range of a system's possible behaviors. The assumptions that lead to algebraically-tractable approximations such as the Michaelis-Menten approach necessarily constrain the operating space of the system in question, which is why the reaction order polytopes in Figures 3.9 and 3.10 are subsets of the polytopes in Figure 3.6.

Even though the assumptions associated with popular approximations are often justified in many biological contexts, the underlying philosophy of environmental synthetic biology necessitates that we cannot assume that such conditions will remain justified across all possible deployment scenarios for our system of interest. Developing the reaction order analysis framework further, as well as other holistic analysis frameworks, will therefore be an essential part of advancing this emerging field of research.

Summary of findings

To summarize, our analysis has revealed the following insights about the intrinsic functional capacity of different transcriptional regulatory architectures:

- The activity of a repressed gene can exhibit an ultrasensitive response to total signal concentration. Activated genes cannot do this.
- The activity of an activated gene can remain sensitive to signal while being robust to gene copy number. Repressed genes cannot do this.
- A gene regulated by an action-modulated activator, specifically, can exist in a regime where its activity is inhibited by the concentration of the activator.

We emphasize that all of these properties are properties intrinsic to the simple model of gene regulation we presented in 3.12. Importantly, this model only captures the activity of a single gene, and does not capture the possibility of this gene being only one component of a larger genetic circuit whose final output is the true 'activity' of the system. In such a case, the ability to incorporate feedbacks and other circuit motifs can confer on these larger systems the same functional behaviors described above– for example, incorporating an incoherent feedback loop has been shown to enable gene copy number robustness from a repressed gene [25].

Nonetheless, we feel that these distinctions between the intrinsic functional capacities of these minimal models are valuable in characterizing the fundamental nature of these regulatory architectures in their simplest form.

3.6 Further research questions in reaction order analysis

The results presented in this section indicate that reaction order analysis can be a powerful tool to reveal insights about biomolecular system behavior. Because reaction order polytopes define bounds which constrain the system's behavior across all possible parametrizations, the framework is particularly apt at classifying architectures according to functional differences, as we saw in sections 3.4 and 3.5.

However, the two types of functional behaviors that we examined in this chapter, ultrasensitivity and robustness, are both naturally expressed in the language of reaction order: ultrasensitivity corresponds to a response of order > 1, and and robustness corresponds to a response of order 0. While these properties are considered to be important components of functional complexity in biomolecular systems [26], it is nonetheless not immediately clear how to translate an arbitrary functional property into the reaction order framework in order to benefit from this analysis approach. A major priority for the continued development of reaction order analysis will therefore be to determine how to perform such a translation.

In addition to representing more types of functional behaviors in the language of reaction orders, it would also be valuable to expand the scope of this log derivative analysis beyond binding networks to accommodate more types of biomolecular reaction systems. Currently, the binding networks covered by our framework do not permit the inclusion of catalysis reactions, which are irreversible reactions that create or destroy a species (such as the conversion reaction $E+S \rightarrow E+P$). These represent a large and important class of biomolecular systems, and determining whether they can also be analyzed holistically to capture all possible system behaviors through the lens of reaction orders would be extremely valuable to the field.

The first step in expanding the reaction order framework to other classes of systems, however, is to ensure that it truly applies to all examples of binding networks. Currently, some key steps in the vertex-edge calculation procedure described in Section 3.3 are not formally proven. In particular, many of the assumptions about the mapping between properties in dominance regime space to reaction order space, such as convexity and edge connectivity, need to be examined more thoroughly to ensue their generality.

Once these steps are taken, reaction order analysis will be on the requisite solid foundations to serve as a practical design tool for biomolecular systems designed to operate in unpredictable environmental contexts. In addition to ruling out architectures that cannot display desired behaviors, the geometric mindset of the reaction order polytopes could also be used to design architectures that are more biased towards desired regions in reaction order space. The polytope of the binding-modulated activator in Section 3.5, for example, is a strict subset of the polytope for the action-modulated activator, despite the fact that they share the same concentration-space domain. We also saw that enforcing a particular dominance condition, such as the free S assumption in Section 3.4 or the Michaelis-Menten assumptions in Section 3.5, yielded subsets of their original unconstrained polytopes. Generalizing this notion of polytope subsetting to narrow the space of possible behaviors down to a compact region that includes the desired target behavior could potentially be a viable strategy for designing biomolecular systems that can more reliably function in unpredictable environments.

References

[1] Michael B. Elowitz and Stanislas Leibler. "A synthetic oscillatory network of transcriptional regulators". *Nature* 403.6767 (2000), pp. 335–338.

[2] Timothy S. Gardner, Charles R. Cantor, and James J. Collins. "Construction of a genetic toggle switch in Escherichia coli". *Nature* 403.6767 (2000), pp. 339–342.

[3] Domitilla Del Vecchio, Alexander J. Ninfa, and Eduardo D. Sontag. "Modular cell biology: retroactivity and insulation". *Molecular Systems Biology* 4.1 (2008), p. 161.

[4] Katherine Ilia and Domitilla Del Vecchio. "Squaring a circle: to what extent are traditional circuit analogies impeding synthetic biology?" *GEN Biotechnology* 1.2 (2022), pp. 150–155.

[5] Domitilla Del Vecchio et al. "Future systems and control research in synthetic biology". *Annual Reviews in Control* 45 (2018), pp. 5–17.

[6] Victoria Hsiao, Anandh Swaminathan, and Richard M. Murray. "Control theory for synthetic biology: recent advances in system characterization, control design, and controller implementation for synthetic biology". *IEEE Control Systems Magazine* 38.3 (2018), pp. 32–62.

[7] Fangzhou Xiao. "Biocontrol of Biomolecular Systems: Polyhedral Constraints on Binding's Regulation of Catalysis from Biocircuits to Metabolism". PhD thesis. California Institute of Technology, 2022.

[8] Sang Hoon Ha and James E. Ferrell Jr. “Thresholds and ultrasensitivity from negative cooperativity”. *Science* 352.6288 (2016), pp. 990–993.

[9] Jacque Monod, Jeffries Wyman, and Jean-Pierre Changeux. “On the nature of allosteric transitions: A plausible model”. *Journal of Molecular Biology* 12.1 (1965), pp. 88–118.

[10] D. E. Koshland, G. Némethy, and D. Filmer. “Comparison of Experimental Binding Data and Theoretical Models in Proteins Containing Subunits”. *Biochemistry* 5.1 (1966), pp. 365–385.

[11] A. Goldbeter and D. E. Koshland. “An amplified sensitivity arising from covalent modification in biological systems.” *Proceedings of the National Academy of Sciences* 78.11 (1981), pp. 6840–6844.

[12] James E. Ferrell. “Tripping the switch fantastic: how a protein kinase cascade can convert graded inputs into switch-like outputs”. *Trends in Biochemical Sciences* 21.12 (1996), pp. 460–466.

[13] Sang Hoon Ha, Sun Young Kim, and James E. Ferrell. “The prozone effect accounts for the paradoxical function of the cdk-binding protein suc1/cks”. *Cell Reports* 14.6 (2016), pp. 1408–1421.

[14] Michael A. Savageau. “Design of molecular control mechanisms and the demand for gene expression.” *Proceedings of the National Academy of Sciences* 74.12 (1977), pp. 5647–5651.

[15] Michael A. Savageau. “Regulation of differentiated cell-specific functions.” *Proceedings of the National Academy of Sciences* 80.5 (1983), pp. 1411–1415.

[16] Michael A. Savageau. “Demand Theory of Gene Regulation. I. Quantitative Development of the Theory”. *Genetics* 149.4 (1998), pp. 1665–1676.

[17] Michael A. Savageau. “Demand Theory of Gene Regulation. II. Quantitative Application to the Lactose and Maltose Operons of Escherichia coli”. *Genetics* 149.4 (1998), pp. 1677–1691.

[18] Ulrich Gerland and Terence Hwa. “Evolutionary selection between alternative modes of gene regulation”. *Proceedings of the National Academy of Sciences* 106.22 (2009), pp. 8841–8846.

[19] Guy Shinar et al. “Rules for biological regulation based on error minimization”. *Proceedings of the National Academy of Sciences* 103.11 (2006), pp. 3999–4004.

[20] Robert Schleif. “AraC protein, regulation of the l-arabinose operon in Escherichia coli, and the light switch mechanism of AraC action”. *FEMS Microbiology Reviews* 34.5 (2010), pp. 779–796.

[21] William Nasser and Sylvie Reverchon. “New insights into the regulatory mechanisms of the LuxR family of quorum sensing regulators”. *Analytical and Bioanalytical Chemistry* 387.2 (2006), pp. 381–390.

[22] Kristi A. Poellinger et al. “Intragenic suppression of a luxR mutation: Characterization of an autoinducer-independent LuxR”. *FEMS Microbiology Letters* 129.1 (1995), pp. 97–101.

[23] D. M. Sitnikov, G. S. Shadel, and T. O. Baldwin. “Autoinducer-independent mutants of the LuxR transcriptional activator exhibit differential effects on the twolux promoters of Vibrio fischeri”. *Molecular and General Genetics* 252.5 (1996), pp. 622–625.

[24] Sarah E. Maddocks and Petra C. F. Oyston. “Structure and function of the LysR-type transcriptional regulator (LTTR) family proteins”. *Microbiology* 154.12 (2008), pp. 3609–3623.

[25] Thomas H. Segall-Shapiro, Eduardo D. Sontag, and Christopher A. Voigt. “Engineered promoters enable constant gene expression at any copy number in bacteria”. *Nature Biotechnology* 36.4 (2018), pp. 352–358.

[26] James E. Ferrell and Sang Hoon Ha. “Ultrasensitivity part III: cascades, bistable switches, and oscillators”. *Trends in Biochemical Sciences* 39.12 (2014), pp. 612–618.

Chapter 4

STRUCTURALLY-ENCODED BEHAVIORS OF GENE REGULATORY CIRCUITS

This chapter presents a new narrative framing for some of the results initially presented in

> John P. Marken, Fangzhou Xiao, and Richard M. Murray. "A geometric and structural approach to the analysis and design of biological circuit dynamics: a theory tailored for synthetic biology". *bioRxiv Preprint* (2020). DOI: 10.1101/2020.02.18.953620.
> J.P.M. and F.X. jointly developed the project and performed the analysis. J.P.M. wrote the manuscript with input from F.X.

4.1 Introduction

The results presented in the previous chapter highlight how reaction order analysis can be a powerful tool for revealing insights about system behavior. However, as pointed out in the concluding section (Section 3.6), the framework is currently only applicable to a specific class of biomolecular systems that we term binding networks and it is still unclear how to use the framework to draw insights about functional properties that are not directly expressable in the language of reaction order, such as robustness or ultrasensitivity.

In this chapter, we present initial progress towards an analysis framework that expands the class of applicable biomolecular systems to those described by arbitrary systems of ordinary differential equations (ODEs), and use it to draw insights about system behaviors that include stability and even temporal dynamics.

This framework is based on a theorem proved by Fangzhou Xiao [1] that shows that under certain conditions, the reaction order matrix provides sufficient information to fully determine the stability of a fixed point. However, for a system described by arbitrary functions $\boldsymbol{f}(\boldsymbol{x})$, calculating the reaction order matrix by taking the log derivatives $\frac{\partial \log \boldsymbol{f}(\boldsymbol{x})}{\partial \log \boldsymbol{x}}$ does not necessarily yield any advantage over obtaining the Jacobian matrix $\frac{\partial \boldsymbol{f}(\boldsymbol{x})}{\partial \boldsymbol{x}}$ directly, which can always give the stability of a fixed point.

When $f(\boldsymbol{x})$ takes the form of a monomial $k x_1^{\alpha_1} x_2^{\alpha_2} \dots x_n^{\alpha_n}$, however, the log derivative *is* significantly simpler than the standard derivative. The derivative of a monomial

is still a monomial, so $\frac{\partial f(\boldsymbol{x})}{\partial x_i} = k x_1^{\alpha_1} x_2^{\alpha_2} \ldots \alpha_i x_i^{\alpha_i - 1} \ldots x_n^{\alpha_n}$. In contrast, the reaction order is simply the constant value $\frac{\partial \log f(\boldsymbol{x})}{\partial \log x_i} = \alpha_i$ (Appendix A).

Unfortunately, most models of biomolecular processes are not monomials. Even if the models are not written using sophisticated functional forms such as those involved in Hill functions, simply adding a constant leak term to an otherwise-regulated process creates a polynomial, rather than monomial, function. The second insight that forms the basis of our framework is therefore the observation that the ODE systems that describe biomolecular reaction systems can be approximated by monomials in certain regions of the system's state space, and that the behavior of these monomial approximations can, when taken together, describe the behavior of the system as a whole.

In section 4.2 we will begin by introducing the core concepts of this analysis framework, culminating in the notion of approximating a system's holistic behavior via the behaviors of a collection of simpler monomial approximations. In section 4.3, we will then walk through the analysis procedure for a simple case study, showing how the approximations' reaction orders can reveal the conditions required for bistability in a leaky positive autoactivation motif. In section 4.4, we will then apply our analysis framework to a model of the synthetic transcriptional oscillator, the Repressilator, to show how the reaction order framework can inform the presence of dynamic system behaviors like oscillations. Finally, we will conclude in section 4.5 with a discussion of the framework's applicability to the design of genetic circuits.

4.2 Preliminary concepts

Approximating a system's dynamics with monomials

The core premise of our analysis framework is that the dynamics of a biomolecular reaction system $\frac{\mathrm{d}\boldsymbol{x}}{\mathrm{d}t} = \boldsymbol{f}(\boldsymbol{x})$ can be approximated by a system of monomials in certain regions of state space. To be precise, for a function $f(x)$ we will define a region of x values to be a **saturation regime** if $f(x)$ can be approximated by a monomial function there. We use the term 'saturation' here to invoke the fact that biomolecular reactions tending to saturate is an essential property of biomolecular, as opposed to other types of physical, systems that enables this type of analysis to provide fruitful insights.

To illustrate this concept, consider the standard Hill-type activation function, given by

$$\text{Hill}(x) = \beta \frac{x^n}{K^n + x^n}. \tag{4.1}$$

We can see that $\text{Hill}(x)$ can be approximated by simpler functions depending on whether x is saturating the expression or not:

$$\begin{aligned} &\text{when } x \ll K, \quad \text{Hill}(x) \approx \beta \frac{x^n}{K^n} = \frac{\beta}{K^n} x^n, \\ &\text{when } x \gg K, \quad \text{Hill}(x) \approx \beta \frac{x^n}{x^n} = \beta. \end{aligned} \tag{4.2}$$

Note that each of the approximations for $\text{Hill}(x)$ above are in monomial form, i.e. they can be written as

$$f(\boldsymbol{x}) = k\boldsymbol{x}^{\boldsymbol{\alpha}} = k x_1^{\alpha_1} x_2^{\alpha_2} \dots x_n^{\alpha_n}.$$

In the case of Equation 4.2, when $x \ll K$ we have $k = \frac{\beta}{K^n}$ and $\alpha = n$, while when $x \gg K$ we have $k = \beta$ and $\alpha = 0$. This means that the saturation regimes for this system are $x \ll K$ and $x \gg K$. The nature of how the approximations align with the true function is shown in Figure 4.1a,b.

Importantly, the notion of a saturation regime generalizes beyond functions which are conventionally thought of as saturatable. Consider the additive function

$$\text{Add}(x) = \beta x + \alpha. \tag{4.3}$$

We can see that this function, too, can be partitioned into saturation regimes to approximate it with monomial functions:

$$\begin{aligned} &\text{when } x \ll \alpha/\beta, \quad \text{Add}(x) \approx \alpha, \\ &\text{when } x \gg \alpha/\beta, \quad \text{Add}(x) \approx \beta x. \end{aligned} \tag{4.4}$$

Figure 4.1c,d depicts the linear addition function, Eq (4.3), in linear space and log-log space. Note that this generalized notion of saturation for the addition function only becomes apparent in log-log space, as here the function can be seen asymptotically approaching the monomials, which become straight lines in the log-log plot.

Now that we have presented the concept of saturation regimes for individual functions, we can move on to describing how they apply to full systems. We will say that a system consists of n system variables governed by a set of n ordinary differential equations (ODEs) which can be written in the form

$$\frac{\mathrm{d}x_i}{\mathrm{d}t} = f_i^+(\boldsymbol{x}) - f_i^-(\boldsymbol{x}), \tag{4.5}$$

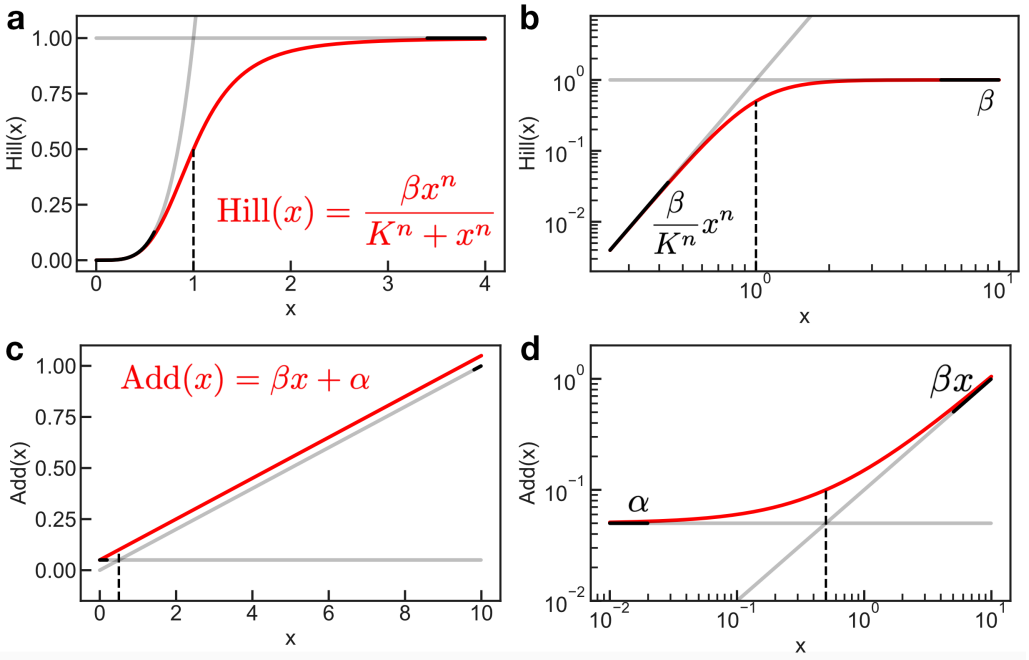

Figure 4.1: An illustration of generalized saturation and its associated regimes, applied to (**a,b**) a Hill activation function and (**c,d**) a linear addition function. The full functions are shown in red and their monomial approximations are plotted in black. The monomials are only valid approximations of the original function within particular windows of x, which are the saturation regimes– these are schematically depicted by the boldness of the black lines. The dashed line indicates the border separating the saturation regimes– for (**a,b**) the line separates $x \ll K$ and $x \gg K$, while for (**c,d**) the line separates $x \ll \alpha/\beta$ and $x \gg \alpha/\beta$. Functions are plotted with (**a,b**) $n = 4$, $K = 1$, $\beta = 1$, and (**c,d**) $\beta = 0.1$, $\alpha = 0.05$.

where $f_i^{\pm}(\boldsymbol{x})$ can be arbitrary sums of arbitrary rational functions. Although this constraint excludes the use of exotic functional forms, we assert that any reasonable model of a biomolecular reaction system can be represented by functions of this category.

At a saturation regime, every $f_i^{+}(\boldsymbol{x})$ and $f_i^{-}(\boldsymbol{x})$ will individually be approximated by monomial functions, meaning the dynamics of a specific species x_i will be the difference of two monomials,

$$\frac{\mathrm{d}x_i}{\mathrm{d}t} \approx k_i^{+}\boldsymbol{x}^{\alpha_i^{+}} - k_i^{-}\boldsymbol{x}^{\alpha_i^{-}}. \tag{4.6}$$

We will say that a system that takes the form of Eq. (4.6) is called a **simple birth-death system**. These systems are notable because they are easy to analyze, particularly in terms of finding their fixed points. Much of the pioneering work that

applied simple birth-death systems to the analysis of biochemical systems, notably the work of Michael Savageau [2], focused on this property. However, we emphasize a different property of these systems– that much of their functional properties can be determined simply from the exponents $\boldsymbol{\alpha}_{\boldsymbol{i}}^{\pm}$, without considering the values of the rate constants $k_i^{\pm}$. We will call such properties the system's **structural properties** in order to invoke the fact that these exponents are typically determined by the functional form, or structure, of the system. For example, in mass-action kinetics, $\boldsymbol{\alpha}_{\boldsymbol{i}}^{\pm}$ directly correspond to the stoichiometric contributions of each x_i to the formed product.

Obtaining the structural stability of a fixed point

An important property of a simple birth-death system is that it will always have a fixed point $\boldsymbol{x}^*$ as long as the system is full-rank [2]. We can therefore always ask whether the stability of $\boldsymbol{x}^*$ can be determined solely by considering the exponents $\boldsymbol{\alpha}_i^{\pm}$.

Recall from Section 4.1 that the reaction order matrix could be used to determine this stability under certain conditions. We will state this theorem here.

First, we define the reaction order matrix $\boldsymbol{H}$ for a system ODE $\frac{\mathrm{d}x_i}{\mathrm{d}t}$ as defined in Equation 4.5, to be

$$\boldsymbol{H} := \boldsymbol{H}^+ - \boldsymbol{H}^-, \tag{4.7}$$

where

$$\begin{aligned}
\boldsymbol{H}^+ &:= \begin{bmatrix} \frac{\partial \log f_1^+(\boldsymbol{x})}{\partial \log x_1} & \frac{\partial \log f_2^+(\boldsymbol{x})}{\partial \log x_1} & \cdots & \frac{\partial \log f_n^+(\boldsymbol{x})}{\partial \log x_1} \\ \frac{\partial \log f_1^+(\boldsymbol{x})}{\partial \log x_2} & \frac{\partial \log f_2^+(\boldsymbol{x})}{\partial \log x_2} & \cdots & \frac{\partial \log f_n^+(\boldsymbol{x})}{\partial \log x_2} \\ \vdots & \vdots & \ddots & \vdots \\ \frac{\partial \log f_1^+(\boldsymbol{x})}{\partial \log x_n} & \frac{\partial \log f_2^+(\boldsymbol{x})}{\partial \log x_n} & \cdots & \frac{\partial \log f_n^+(\boldsymbol{x})}{\partial \log x_n} \end{bmatrix} \\
\boldsymbol{H}^- &:= \begin{bmatrix} \frac{\partial \log f_1^-(\boldsymbol{x})}{\partial \log x_1} & \frac{\partial \log f_2^-(\boldsymbol{x})}{\partial \log x_1} & \cdots & \frac{\partial \log f_n^-(\boldsymbol{x})}{\partial \log x_1} \\ \frac{\partial \log f_1^-(\boldsymbol{x})}{\partial \log x_2} & \frac{\partial \log f_2^-(\boldsymbol{x})}{\partial \log x_2} & \cdots & \frac{\partial \log f_n^-(\boldsymbol{x})}{\partial \log x_2} \\ \vdots & \vdots & \ddots & \vdots \\ \frac{\partial \log f_1^-(\boldsymbol{x})}{\partial \log x_n} & \frac{\partial \log f_2^-(\boldsymbol{x})}{\partial \log x_n} & \cdots & \frac{\partial \log f_n^-(\boldsymbol{x})}{\partial \log x_n} \end{bmatrix}.
\end{aligned} \tag{4.8}$$

When $\boldsymbol{H}$ is applied to a simple birth-death system, the (i, j) entry of $\boldsymbol{H}^{\pm}$ is the $\alpha_i^{\pm}$ value from $f_j^{\pm}(\boldsymbol{x})$.

We can now state the Theorem:

Theorem 4.2.1 (Xiao) *For a system* $\frac{\mathrm{d}\boldsymbol{x}}{\mathrm{d}t} = \boldsymbol{f}^{+}(\boldsymbol{x}) - \boldsymbol{f}^{-}(\boldsymbol{x})$*, the reaction order matrix* $\boldsymbol{H} = \boldsymbol{H}^{+} - \boldsymbol{H}^{-}$ *is diagonally stable if and only if the Jacobian* $\boldsymbol{J}(\boldsymbol{x}) := \frac{\partial \boldsymbol{f}^{+}(\boldsymbol{x})}{\partial \boldsymbol{x}} - \frac{\partial \boldsymbol{f}^{-}(\boldsymbol{x})}{\partial \boldsymbol{x}}$ *is diagonally stable.*

A matrix $\boldsymbol{A}$ *is* ***diagonally stable*** *if there exists a positive diagonal matrix* $\boldsymbol{P}$ *such that* $\boldsymbol{P}\boldsymbol{A} + \boldsymbol{A}^{\intercal}\boldsymbol{P}$ *is negative definite.*

A fixed point $\boldsymbol{x}^{*}$ *of* $\boldsymbol{f}(\boldsymbol{x})$ *is stable if* $\boldsymbol{J}(\boldsymbol{x}^{*})$ *is diagonally stable.*

We will refer to stability obtained through satisfying this condition on $\boldsymbol{H}$ as **structural stability**, because the entries of $\boldsymbol{H}$ for simple birth-death systems are invariant to the value of the rate constants $\boldsymbol{k}$. Note that a fixed point $\boldsymbol{x}^{*}$ can be stable without being structurally stable, which occurs when the other parameters that appear in $f(x)$ (namely the rate constants) contribute to the fixed point's stability.

Verifying the existence of $\boldsymbol{P}$ can be done even for large systems by numerically solving the linear matrix inequality $\boldsymbol{P}\boldsymbol{A} + \boldsymbol{A}^{\intercal}\boldsymbol{P} < \boldsymbol{0}$. There are additionally a number of simpler conditions where the diagonal stability of $\boldsymbol{H}$ is assured [1]. These include:

- If $\boldsymbol{H}$ is triangular with negative diagonal entries.
- If $\boldsymbol{H}$ is symmetric and negative definite.
- If $\frac{1}{2}(\boldsymbol{H} + \boldsymbol{H}^{\intercal})$ is negative definite.

For a 1-dimensional system where $\boldsymbol{H}$ is a scalar, the above conditions apply so a fixed point x^{*} is always structurally stable if $H < 0$.

4.3 Case study: bistability in a leaky positive autoregulation motif

Now that we have demonstrated the core concepts associated with the structural dynamics mindset, we will illustrate their application to the analysis of a simple circuit, the leaky positive autoactivation motif. We will specifically determine the requirements for the system to exhibit bistability, the property of having an unstable fixed point in between two stable fixed points.

This circuit consists of a single gene x which is produced at some leaky rate α and removed at some rate γ. x also activates its own production with Hill kinetics. The

model for the circuit is

$$\frac{\mathrm{d}x}{\mathrm{d}t} = \alpha + \frac{\beta x^n}{K^n + x^n} - \gamma x. \tag{4.9}$$

We will begin by finding the system's saturation regimes and determining its structural regimes there– in other words, we will saturate the system's birth and death terms until they are both monomials.

Since the death term, $f^-(x) = \gamma x$, is already a monomial, we do not need to perform any saturations there. We instead focus on the birth term $f^+(x) = \alpha + \frac{\beta x^n}{K^n + x^n}$. The Hill component is a good place to begin– we can see that if $x \ll K$ or if $x \gg K$, we can approximate the system with simpler functions. In particular,

$$\begin{aligned} &\text{when } x \ll K, \quad f^+(x) \approx \alpha + \frac{\beta}{K^n} x^n. \\ &\text{when } x \gg K, \quad f^+(x) \approx \alpha + \beta. \end{aligned} \tag{4.10}$$

While $\alpha + \beta$ is a monomial, $\alpha + \frac{\beta}{K^n} x^n$ is not, meaning there is still a saturation to be found there. This term is saturated when $\alpha \gg \frac{\beta}{K^n} x^n$, i.e. when $x \ll \left(\frac{\alpha}{\beta}\right)^{\frac{1}{n}} K$. Incorporating this second saturation, we now obtain the full set of the system's saturation regimes:

$$\begin{aligned} \text{when } x \ll K \text{ and } x \ll \left(\frac{\alpha}{\beta}\right)^{\frac{1}{n}} K, \quad & \frac{dx}{dt} \approx \alpha - \gamma x. \\ \text{when } x \ll K \text{ and } x \gg \left(\frac{\alpha}{\beta}\right)^{\frac{1}{n}} K, \quad & \frac{dx}{dt} \approx \frac{\beta}{K^n} x^n - \gamma x. \\ \text{when } x \gg K, \quad & \frac{dx}{dt} \approx \alpha + \beta - \gamma x. \end{aligned} \tag{4.11}$$

These are depicted in Figure 4.2.

Note that the second saturation regime in Eq (4.11) contradicts itself unless $\alpha \ll \beta$. Therefore this saturation regime can only exist when this parameter condition is satisfied, i.e. when the leaky production rate is smaller than the saturated production rate from the Hill term.

The next step in our analysis is to compute the log-derivative transformation H (Eq (4.7)) at each structural regime to determine its structural stability. We will also set the ODEs of each structural regime to steady state in order to find the fixed points associated with each saturation regime, which we call the **saturation fixed points**.

Because each $f^+(x)$ and $f^-(x)$ are monomials in each approximation, we can simply read off the exponents of x and subtract them for each saturation regime, to obtain

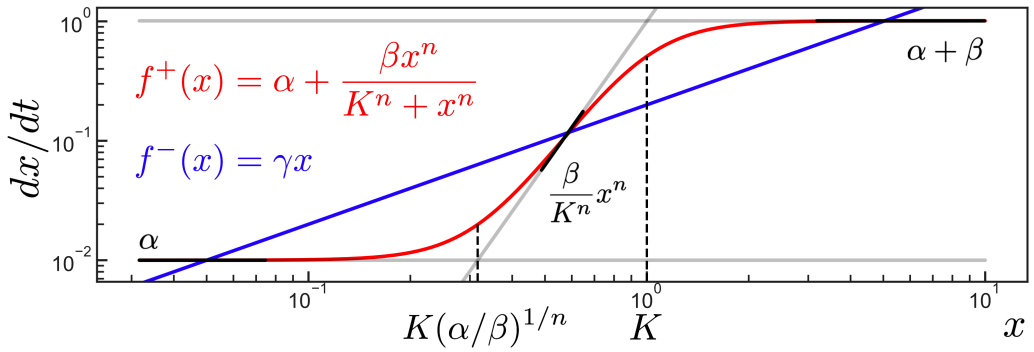

Figure 4.2: The structural regimes of the leaky positive autoregulation motif, Eq (4.9). The birth term and death term of the original model are plotted in red and blue, respectively. The model's structural regimes are plotted in black, as in Figure 4.1.

the value of H. The fixed points are also found easily because each approximation is a simple birth-death system. We obtain

$$\begin{aligned}
&\text{when } \frac{dx}{dt} \approx \alpha - \gamma x, \quad H = -1 \text{ and } x^* = \frac{\alpha}{\gamma}. \\
&\text{when } \frac{dx}{dt} \approx \frac{\beta}{K^n} x^n - \gamma x, \quad H = n - 1 \text{ and } x^* = \left(\frac{K^n \gamma}{\beta}\right)^{\frac{1}{n-1}}. \\
&\text{when } \frac{dx}{dt} \approx \alpha + \beta - \gamma x, \quad H = -1 \text{ and } x^* = \frac{\alpha + \beta}{\gamma}.
\end{aligned} \tag{4.12}$$

Note that if $n < 1$, all of the saturation fixed points in this system are structurally stable. Therefore, in order for the system to exhibit structural bistability, we require $n > 1$ so that the middle saturation fixed point can be unstable.

For the final step in our analysis, we must recall that these saturation fixed points are not necessarily the fixed points of our original system– they are the fixed points associated with the monomial approximations, which are only valid when the system is inside the associated saturation regime. Therefore, these saturation fixed points are only valid descriptions of the system's behavior if they actually lie within their associated saturation regimes.

The conditions required for the fixed points to lie within their saturation regimes, which we will call the **regime consistency conditions**, can be determined in a straightforward way by plugging in the expression for the saturation fixed point into the conditions that define the saturation regime. For our system, our regime

consistency conditions are

$$\begin{aligned}
&\text{when } x \ll K \text{ and } x \ll \left(\frac{\alpha}{\beta}\right)^{\frac{1}{n}} K, \quad x^* = \frac{\alpha}{\gamma}, \quad \text{so } \frac{\alpha}{\gamma} \ll K \text{ and } \frac{\alpha}{\gamma} \ll \left(\frac{\alpha}{\beta}\right)^{\frac{1}{n}} K. \\
&\text{when } x \ll K \text{ and } x \gg \left(\frac{\alpha}{\beta}\right)^{\frac{1}{n}} K, \quad x^* = \left(\frac{K^n \gamma}{\beta}\right)^{\frac{1}{n-1}}, \quad \text{so } \left(\frac{\alpha}{\beta}\right)^{\frac{1}{n}} \ll \left(\frac{K\gamma}{\beta}\right)^{\frac{1}{n-1}} \ll 1. \\
&\text{when } x \gg K, \quad x^* = \frac{\alpha+\beta}{\gamma}, \quad \text{so } \frac{\alpha+\beta}{\gamma} \gg K.
\end{aligned} \tag{4.13}$$

We can see that in order to satisfy each of these individual consistency conditions, the system must satisfy additional parameter constraints. For example, we see that the middle regime requires both $\beta \gg \alpha$ (which was already required in order for this saturation regime to exist at all) and $\beta \gg K\gamma$ (a new constraint).

Now, in order to show that that the system exhibits structural bistability, we must show that none of the regime consistency conditions contradict each other, so that all three saturation fixed points can simultaneously coexist within their respective saturation regimes. We see that the conditions for the first two regimes above are internally consistent, as they can be written in the form

$$\frac{\alpha}{\gamma K} \ll \left(\frac{\alpha}{\beta}\right)^{\frac{1}{n}} \ll \left(\frac{K\gamma}{\beta}\right)^{\frac{1}{n-1}} \ll 1. \tag{4.14}$$

The final regime consistency condition can be written as

$$1 \ll \frac{\alpha}{\gamma K} + \frac{\beta}{\gamma K}. \tag{4.15}$$

Since Eq (4.14) implies that $\beta/\gamma K \gg 1$, we can see that there is no contradiction between Eq (4.14) and Eq (4.15). Thus all three regime conditions can coexist without contradiction, so all three steady states are able to coexist as long as these parameter conditions are satisfied.

Thus we have determined that in order for the leaky positive autoactivation motif (Eq (4.9)) to exhibit structural bistability, we need the leaky production rate to be small compared to the activated producction rate ($\alpha \ll \beta$), we need cooperativity in the Hill term ($n > 1$), and we need strong production ($\beta \gg K\gamma$). In addition, the regime consistency conditions Eq ((4.14) and (4.15)) must be satisfied, providing the additional constraint that $\alpha < \gamma K$. Table 4.1 compiles the results of our analysis.

In addition to enabling the pipeline above, the conceptual tools we have described can be used in an exploratory manner to reveal insights and intuition about a system's dynamics. We will develop this point further in the next section.

System	$\frac{dx}{dt} = \alpha + \frac{\beta x^n}{K^n + x^n} - \gamma x$		
Saturation Regimes	$x \ll \min\left\{\left(\frac{\alpha}{\beta}\right)^{\frac{1}{n}} K, K\right\}$	$\left(\frac{\alpha}{\beta}\right)^{\frac{1}{n}} K \ll x \ll K$	$\max\left\{\left(\frac{\alpha}{\beta}\right)^{\frac{1}{n}} K, K\right\} \ll x$
Monomial Approximations	$\frac{dx}{dt} \approx \alpha - \gamma x$	$\frac{dx}{dt} \approx \frac{\beta}{K^n} x^n - \gamma x$	$\frac{dx}{dt} \approx \alpha + \beta - \gamma x$
Reaction Order	$H = -1$	$H = n - 1$	$H = -1$
Structural Stability	Stable	Stable when $n < 1$	Stable
Saturation Fixed Point	$x^* = \frac{\alpha}{\gamma}$	$x^* = \left(\frac{K^n \gamma}{\beta}\right)^{\frac{1}{n-1}}$	$x^* = \frac{\alpha+\beta}{\gamma}$
Regime Consistency Conditions	$\frac{\alpha}{K\gamma} \ll \left(\frac{\alpha}{\beta}\right)^{\frac{1}{n}} \ll 1$	$\left(\frac{\alpha}{\beta}\right)^{\frac{1}{n}} \ll \left(\frac{K\gamma}{\beta}\right)^{\frac{1}{n-1}} \ll 1$	$1 \ll \frac{\alpha}{\gamma K} + \frac{\beta}{\gamma K}$

Table 4.1: The concepts involved in the analysis of structural bistability in the leaky positive autoactivation circuit, Eq (4.9).

4.4 Structural oscillations in the Repressilator

Now that we have demonstrated how to analyze structural bistability in a system, we will now proceed to use the framework to analyze structural oscillations in a simple model of the well-known Repressilator circuit [3]. The key distinction between this analysis and our previous analysis of the leaky positive autoactivation motif is that here we will actively find that the regime consistency conditions are not satisfied. Instead of the system's fixed points coexisting within their respective saturation regimes, as occurred in the case for multistability, we will instead find that each fixed point exists inside another saturation regime, such that one saturation regime will "point" to another. This pointing will create a structurally stable oscillatory cycle (Figure 4.3).

To begin our analysis, we will construct a simple model of the Repressilator where each component is modeled symmetrically with no leaky production, and where mRNA and protein dynamics are merged together. Then we have

$$\begin{aligned} \frac{dx_1}{dt} &= \frac{\alpha}{1+x_3^n} - x_1, \\ \frac{dx_2}{dt} &= \frac{\alpha}{1+x_1^n} - x_2, \\ \frac{dx_3}{dt} &= \frac{\alpha}{1+x_2^n} - x_3. \end{aligned} \tag{4.16}$$

Each species x_i has two possible saturation regimes depending on the value of its repressor x_j. If we specify the ordering of indices as $i = 1, 2, 3$ and $j = 3, 1, 2$, then the structural regimes for x_i (and their associated fixed points) are

$$\begin{aligned} &\text{when } x_j \ll 1, && \frac{dx_i}{dt} = \alpha - x_i, && x_i^* = \alpha \\ &\text{when } x_j \gg 1, && \frac{dx_i}{dt} = \frac{\alpha}{x_j^n} - x_i, && x_i^* = \frac{\alpha}{x_j^{*n}}. \end{aligned} \tag{4.17}$$

We now investigate the conditions under which this model exhibits structural oscillations. We will do this by first finding conditions for the existence of structurally stable consistent fixed points, and then negating those conditions.

Consider the fixed point in the saturation regime where $x_1, x_2, x_3 \ll 1$, which is $(x_1^*, x_2^*, x_3^*) = (\alpha, \alpha, \alpha)$. The $\boldsymbol{H}$ associated with this saturation regime is $\boldsymbol{H} = \begin{bmatrix} -1 & 0 & 0 \\ 0 & -1 & 0 \\ 0 & 0 & -1 \end{bmatrix}$, which is diagonally stable, so the fixed point is structurally stable.

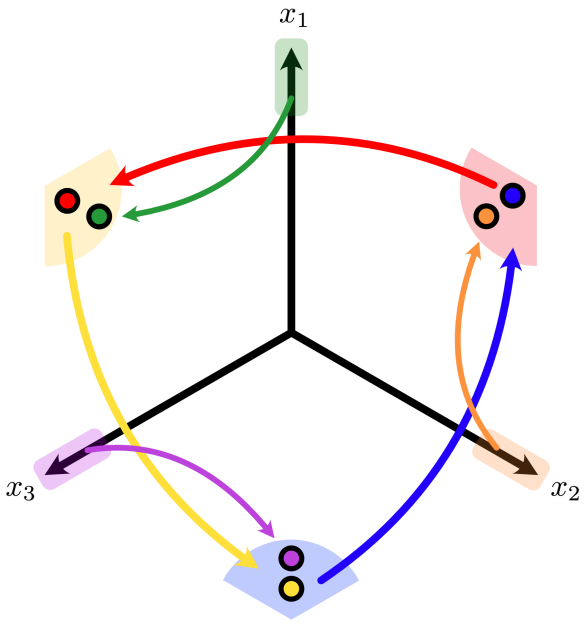

Figure 4.3: Part of the saturation polytope for the repressilator model in Eq (4.16), with $\alpha \gg 1$ and $n \geq 2$. When the system is in one of the saturation regimes shown above, it moves towards the stable fixed point associated with its structural regime. Because this fixed point lies in different saturation regime, once the system gets close to the point, it becomes attracted to another stable fixed point that is in a yet-again different saturation regime. This cycle forms an oscillation. The two saturation regimes corresponding to all species being low concentration and all species being high concentration are not shown here.

In order for this fixed point to exist inside the saturation regime, i.e. $(x_1^*, x_2^*, x_3^*) \ll (1, 1, 1)$, it must be the case that $\alpha \ll 1$. Therefore, in order to make this structurally stable fixed point inconsistent with its saturation regime, we must satisfy $\alpha \gg 1$. Doing so ensures that when the system is in the $x_1, x_2, x_3 \ll 1$ saturation regime, it will tend towards a stable attractor that lies outside of the regime. Thus the system will stay in this saturation regime for only a transient period of time.

Now consider the fixed point in the saturation regime where $x_1, x_2, x_3 \gg 1$, which is $(x_1^*, x_2^*, x_3^*) = (\alpha^{\frac{1}{n+1}}, \alpha^{\frac{1}{n+1}}, \alpha^{\frac{1}{n+1}})$. Since we have already claimed $\alpha \gg 1$, this fixed point can exist inside the saturation regime without contradictions. We therefore need to ensure that this fixed point is not structurally stable in order to enable long-term structural oscillations in this system.

Note that the value of $\boldsymbol{H}$ in this saturation regime is $\boldsymbol{H} = \begin{bmatrix} -1 & 0 & -n \\ -n & -1 & 0 \\ 0 & -n & -1 \end{bmatrix}$, which has

eigenvalues $-(n+1)$ and $-\frac{1}{2}\left(n-2\pm i\sqrt{3}n\right)$. Recall that if $(\boldsymbol{H}+\boldsymbol{H}^{\intercal})/2$ is negative definite, then $\boldsymbol{H}$ is diagonally stable. The unique eigenvalues of $(\boldsymbol{H}+\boldsymbol{H}^{\intercal})/2$ are $(n-2)/2$ and $-(n+1)$, meaning that $n<2$ is a sufficient condition for structural stability in this regime. In order for this fixed point to be unstable, therefore, it is necessary that we have $n\geq 2$.

Hence we now have two parameter conditions that are necessary for structural oscillations in this system: $\alpha \gg 1$ and $n \geq 2$. For the six remaining regimes, we will see that no further constraints on the parameters are needed, and these regimes contain an oscillatory cycle.

For the remaining six structural regimes, it can be easily shown that H is Hurwitz and triangular, meaning that their fixed points will be structurally stable. Thus we will analyze the location of these fixed points, to see if they lie inside their associated saturation regimes or not. For convenience, in this section we will adopt the notation of $(\uparrow,\downarrow,\uparrow)$ to represent the saturation regime where $x_1 \gg 1$, $x_2 \ll 1$, and $x_3 \gg 1$.

We will begin with the $(\uparrow,\downarrow,\uparrow)$ saturation regime. The fixed point associated with this saturation regime is $(x_1^*,x_2^*,x_3^*) = (\alpha^{-(n-1)},\alpha^{n(n-1)+1},\alpha)$, which lies in the saturation regime given by $(\downarrow,\uparrow,\uparrow)$. The fixed point associated with this saturation regime is $(x_1^*,x_2^*,x_3^*) = (\alpha^{n(n-1)+1},\alpha,\alpha^{-(n-1)})$, which lies in saturation regime $(\uparrow,\uparrow,\downarrow)$. This regime in turn has fixed point in the saturation regime we started with, $(\uparrow,\downarrow,\uparrow)$. This completes a cycle among the saturation regimes that proceeds indefinitely (Figure 4.3).

Starting at one of the three remaining saturation regimes results in convergence to this same cycle. Consider one of them, say $(\uparrow,\downarrow,\downarrow)$. Then the fixed point associated with this saturation regime is $(x_1^*,x_2^*,x_3^*) = (\alpha,\alpha^{1-n},\alpha)$. Since $\alpha \gg 1$, we see that this fixed point lies in the $(\uparrow,\downarrow,\uparrow)$ saturation regime, which is one of the three regimes in the cycle. The remaining two saturation regimes can be shown to converge to the cycle in the same way (Fig. 4.3).

We note that this conceptualization of the structural oscillations is qualitatively distinct from the conventional dynamical systems approach used in the original analysis of the Repressilator [3, 4]. There, requirements for oscillations were determined by first determining that the system contains a single unique steady state, and then determining conditions under which that steady state becomes unstable. The oscillations are then assumed to exist in the form of a limit cycle, based on the assumption that there must be at least one stable attractor within the phase space.

In contrast, our structural mindset sees the Repressilator's oscillations as a linked series of three stable fixed points, each of which point to each other by lying outside of their associated saturation regimes. As the system tends towards one fixed point, it will eventually enter a new saturation regime, causing the system's structural regime to change. This invalidates the original fixed point the system was approaching, and creates a new stable fixed point (in yet another saturation regime) that the system now follows. When this loop closes, the cycle forms an oscillation. We argue that the structural mindset yields a much more intuitive conceptualization of the Repressilator's dynamics, as it is much more closely tied to the circuit's structure of three interlinked repressors and does not need to invoke a limit cycle to explain its oscillations.

However, we must emphasize that we have not yet determined a formal proof that oscillations can indeed emerge from such a scenario. The main point of potential concern is that we do not guarantee that once a system leaves one saturation regime by approaching its associated saturation fixed point that lies in a different saturation regime, that it will continue to proceed in that direction until it reaches the new saturation regime. Indeed, once the system leaves this initial saturation regime, the saturation fixed point is no longer a valid approximation so there is no guarantee that the system's true dynamics will proceed toward it. Nonetheless, we feel that this potentially new mechanistic explanation for biomolecular oscillators is sufficiently intriguing to merit further investigation.

4.5 Discussion

The case studies that we analyzed above illustrate how our theory is tailored towards the specific properties of genetic circuits as biological systems. The distinction between our theory's conceptual framework and the more conventional dynamical systems approach to analyzing genetic circuit behavior is best highlighted in the case of the Repressilator, where instead of the conventional notion of a stable limit cycle as a singular entity we frame its oscillations as a set of stable fixed points pointing at each other. This conceptualization is much more grounded in the biological reality of the system being studied. Similarly, the insights gained from the analysis of the leaky positive autoactivation motif, by being framed in the language of saturation and structural dynamics rather than in the specific parameters of a particular model implementation, are easily generalizable to a larger class of systems beyond this specific circuit. Such generalizable insights will be essential for gaining the deep understanding of the structure-function relationship in genetic

systems that is required for the predicable engineering of complex circuits.

Furthermore, our analysis approach is algorithmic, in that the same procedure is applied to analyze any circuit: First, the system is saturated until all its structural regimes are found. Then, the saturation fixed points are calculated, along with their stability. Finally, the regime consistency conditions are used to determine the location of these fixed points. Each individual step is simple to perform and understand, regardless of the complexity of the circuit being analyzed. Furthermore, although our saturation procedure is distinct from the recasting procedure developed by Voit and Savageau [5] for converting generalized mass-action systems into S-System form, it is still similar in many respects, and the successful computerized automation of the recasting procedure [6–8] bodes well for the ability to eventually automate our own saturation procedure.

The algorithmic nature of our analysis contrasts with conventional dynamical systems approaches to genetic circuit analysis, which focus on phase diagram representations of the system's dynamics– these often require numerical solution of the ODEs and a complex intuition about how changes in parameters will affect changes in objects in the phase plane. The end result is a system that does not scale well to analyzing large, complex circuits– each such circuit must essentially be analyzed from scratch with an *ad hoc* approach.

Despite the advantages of our approach, there are still a number of points which need to be developed. The main drawback is the lack of rigorous mathematical proofs and justifications for the various assumptions we make, and specifically how the dynamics of these monomial approximations connect back to the original system. In particular, the monomial approximations capture the dynamics of the original system only when the system is far from the border of a saturation regime– closer to this border, the approximation breaks down. Currently we assume that the system dynamics transition smoothly from one monomial approximation to another, but this must be proven rigorously. Furthermore, the utility of the monomial approximations themselves must still be expanded further– continued efforts to expand the scope of structural stability by further investigating the connection between the reaction order matrix $\boldsymbol{H}$ and the Jacobian matrix $\boldsymbol{J}$ are ongoing.

When using this framework to aid in the design of circuits, however, this lack of rigor becomes less of an issue because the predictions of our theory can be assessed directly by experiment without relying on mathematical guarantees. Furthermore, the fact that the theory frames the dynamical properties directly through structural

concepts also aids in the experimental interrogation of these systems– when designing circuits, it is often much easier to discretely add or remove structural components than it is to predictably tune parameters precisely.

In conclusion, we hope that the advantages of this framework will not only prove useful to synthetic biologists in designing more complex circuits, but will also inspire more groups to follow the strategy of developing conceptual languages that are tailored to the needs of biological systems rather than relying on the conceptual language of other disciplines. Such an approach, when taken in complement with existing efforts to make biological systems more amenable to analysis by theoretical tools from the engineering sciences, will hopefully lead to a more holistic and fundamental understanding of the design principles governing biological systems.

References

[1] Fangzhou Xiao, Mustafa Khammash, and John C. Doyle. "Stability and control of biomolecular circuits through structure". *2021 American Control Conference (ACC)*. IEEE. 2021, pp. 476–483.

[2] Michael A. Savageau. "Introduction to S-systems and the underlying power-law formalism". *Mathematical and Computer Modelling* 11 (1988), pp. 546–551.

[3] Michael B. Elowitz and Stanislas Leibler. "A synthetic oscillatory network of transcriptional regulators". *Nature* 403.6767 (2000), pp. 335–338.

[4] Olguţa Buşe, Alexey Kuznetsov, and Rodrigo A. Pérez. "Existence of limit cycles in the repressilator equations". *International Journal of Bifurcation and Chaos* 19.12 (2009), pp. 4097–4106.

[5] Michael A. Savageau and Eberhard O. Voit. "Recasting nonlinear differential equations as S-systems: a canonical nonlinear form". *Mathematical Biosciences* 87.1 (1987), pp. 83–115.

[6] Rick A. Fasani and Michael A. Savageau. "Automated construction and analysis of the design space for biochemical systems". *Bioinformatics* 26.20 (2010), pp. 2601–2609.

[7] Jason G. Lomnitz and Michael A. Savageau. "Design space toolbox V2: Automated software enabling a novel phenotype-centric modeling strategy for natural and synthetic biological systems". *Frontiers in Genetics* 7 (2016), p. 118.

[8] Miguel Á Valderrama-Gómez et al. "Mechanistic modeling of biochemical systems without a priori parameter values using the design space toolbox v. 3.0". *iScience* 23.6 (2020), p. 101200.

Chapter 5

TRANSCRIPTIONAL RESPONSE FUNCTIONS IN CARBON-LIMITED GROWTH ARREST

The work described in this chapter is unpublished.

5.1 Introduction

Modular and reliable part characterization is a central tenet of synthetic biology. By being able to trust that the measured performance of a genetic part will remain consistent in a larger genetic context, we can wire these parts together in order to create complex genetic circuitry. This is the basis for reliable design in mature engineering disciplines, and the rapid progress on this front was a central factor in advancing synthetic biology to the stage it is at today.

However, much of synthetic biology's existing design process has occurred within the well-contained environments of laboratory settings. This means that the fundamental modularity assumption (whether measurements from a spec sheet will still hold true in a different context) has not been evaluated in the context of natural environments.

One class of genetic parts for which this concern is particularly relevant to environmental applications is that of transcriptional regulation modules. Each such module is defined by a cognate pair of a promoter and its transcription factor. Many such modules activates gene expression in the presence of an induction signal, which could be a specific chemical compound or an environmental variable like temperature or pH. These inducible modules are therefore a central component of engineered microbial sense-and-response systems, which are a major focus of current environmental synthetic biology efforts [1]. For such 'sentinel cells', the reliability of the induction curve's behavior is fundamental to the performance of the entire system. It is therefore of great immediate interest for synthetic biologists to determine whether existing characterization information for such inducible modules, obtained through laboratory settings, are actually predictive of system performance in more natural environmental settings.

In this chapter, we describe preliminary efforts towards addressing the question of whether the various properties of the transcriptional response curve for different

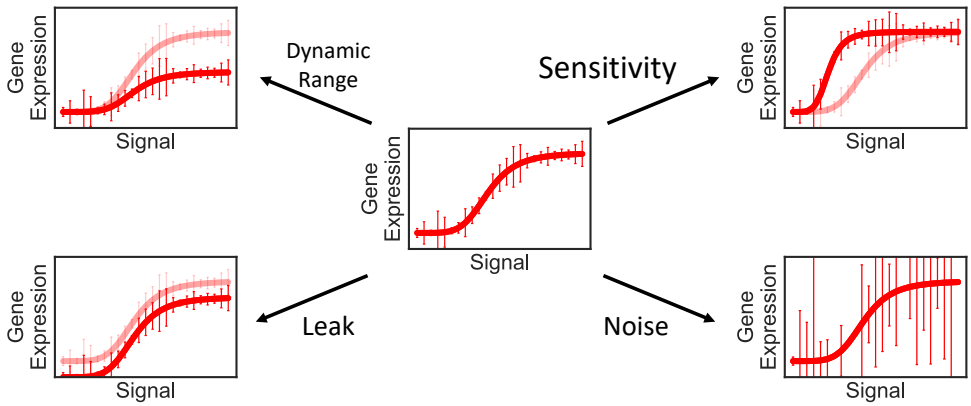

Figure 5.1: Schematic of how various properties of an induction curve measured in a well-controlled laboratory environment (dark red, center) could shift to a new behavior in a different environmental condition (light red curves, outer plots). Not shown is the possibility that the curve could be come more switchlike or graded. In realistic settings, most or all of these properties would likely shift, simultaneously, in different ways.

promoters shift in consistent ways when cells experience nutrient limitation (Figure 5.1). The experimental setup described here could be used to screen a large library of different promoters, in order to determine whether there are consistent trends in these shifts that could be used as a basis to predict post-deployment part function based on laboratory-derived part characterization. Furthermore, such a screen could be used to examine whether different categories of promoters exhibit different characteristic shift profiles, which would both enable more reliable engineering of genetic circuits for environmental applications and also advance our understanding of how physiological responses to nutrient limitation affect microbial transcriptional activity.

We begin in Section 5.2 by briefly reviewing the existing literature on microbial gene expression under growth arrested conditions, with a particular emphasis on active transcriptional regulation. In Section 5.3 we present the experimental design for our assay to measure the shifts in transcription factor induction properties from exponential phase to carbon-limited growth arrest. We present and discuss the preliminary results from our assay in Section 5.4, and propose a future direction of focusing specifically on the response curves of transcriptional repressors in Section 5.5.

5.2 Background: Inducible gene expression during growth arrest

Because different natural environments can differ widely in the nature and magnitude of the environmental variables, we will begin by narrowing the focus of our study to a particular type of environmental stressor. We will specifically investigate the impact of nutrient limitation on gene induction curves, so that our results can interface with an existing body of literature studying the physiology of growth arrest.

Understanding cellular physiology under nutrient limitation is critical for environmental applications of microbiology, as microbes are thought to be experiencing at least some kind of nutrient limitation the vast majority of the time in natural environments [2]. As a consequence, the growth rates of these environmental microbes are often much lower than their maximal capacity at exponential phase, and the cells could even be in a fully growth-arrested, quiescent state [3]. Such physiological states are associated with a number of well-documented changes in their internal states [2–4].

For our research focus, the most relevant properties are those associated with gene expression. While some specific genes have been identified to be upregulated during long-term nutrient limitation [5, 6], in general bacteria heavily downregulate their global gene expression levels under growth-arrested conditions, such that the general rate of new protein synthesis is believed to be 1500-fold lower than during exponential growth, being driven from a pool of approximately 100 ribosomes per cell rather than the 62,000 estimated to exist during rapid growth conditions [7].

Despite the fact that the maintenance gene expression, even at low levels, is required for the long-term viability of the growth-arrested populations, there are few known mechanisms for the active upregulation of targeted genes under growth arrest. Furthermore, the mechanisms that are known, such as the recently-identified *Pseudomonas aeruginosa* transcription factor SutA, are thought to act as global modulators of a large portion of the transcriptome [8, 9]. The activity of gene-specific transcriptional regulators, particularly those with a well-defined and specific DNA binding sequence, is greatly understudied under these physiological conditions.

The existing work on this front essentially consists of a single report, published by Gefen et al. [10], that used a microfluidic device to measure the expression of a fluorescent protein in E. coli that reached growth arrest by naturally depleting the resources in their media. The authors induced the expression of GFP driven by two synthetic promoters, the IPTG-inducible P_{Tac} and the atc-inducible $P_{L\text{-}Tet}$, by adding the inducers to the culture 15 hours after the onset of growth arrest. They

found that not only did most (90%) of the cells respond to the inducer, but that the GFP expression rate turned on almost immediately and remained at a nearly constant level for up to 10 hours. The authors therefore termed this physiological condition the Constant Activity at Stationary Phase (CASP) state.

Unfortunately, Gefen et al. did not provide any detailed information about the dynamics or dose-response profile of the cells in the microfluidic condition. They instead shifted to a batch culture setting where they once again found that this constant rate of protein expression was observed, with a protein synthesis rate that was approximately 10-fold lower than during exponential growth. The authors even measured an induction curve for their two promoter systems during CASP, showing that they followed the typical sigmoidal response profile [10]. Unfortunately, the authors did not measure these curves during exponential phase growth, so that assessments of how the functional attributes of the induction curve (such as its steepness or sensitivity) change under CASP conditions cannot be made.

Despite the intriguing nature of this result, to our knowledge there has been no follow-up work further investigating CASP's implications for either our scientific understanding of microbial growth arrest or our ability to engineer synthetic biology devices that can function reliably under growth-arrested conditions. The closest example is a paper by Bittihn et al. [11] that examined the performance of synthetic genetic devices more generally across a variety of physiological growth conditions within a microfluidic chamber. In this setup, media containing fresh nutrients was continuously flowed over the open face of the chamber so that cells near that face could grow and divide perpetually– the cells in the back of the chamber, however, ceased to actively grow after 1 hour because the nutrients from the media presumably do not reach them. In this way, the setup models the spatial nutrient gradients within a biofilm, where cells on the interior are limited for nutrients available in the outside environment. The authors found that a fluorescent reporter gene driven by either $P_{L\text{-}LacO1}$ or P_{LuxI} could be induced to different levels when varying concentrations of inducer (IPTG and the Lux AHL, respectively) were added 5 hours after growth arrest. As before, however, the authors did not directly compare these induction curves to those obtained during exponential growth, preventing an assessment of how these properties vary.

As such, there still remains a need for an experimental study that directly measures transcriptional induction curves for a population in both exponential phase and growth-arrested conditions, so that the nature of the shifts in its response properties

can be quantitatively characterized. In the following section we describe the design of such an assay.

5.3 Experimental design

Method of growth arrest

As many authors have pointed out, the terms 'stationary phase' or even 'growth arrest' do not correspond to specific, well-defined physiological states [2]. Depending on the nature of the actual limiting nutrient, key physiological properties of the cell can differ widely even when they converge to the same high-level property of a lack of growth [12, 13]. This variability is exacerbated when cells reach stationary phase in the conventional way, by naturally depleting the nutrients in their media– depending on the media formulation and strain growth dynamics, the specific limiting nutrient can vary across experimental setups. While efforts to characterize the various growth limitations over the course of a 'standard' laboratory growth phase exist [14], they are not yet extensive enough to reliably infer the true physiological state of the cell.

An additional confounding factor is the fact that even when a consistent limiting nutrient is chosen for an experiment, the way in which this limitation is imposed will also impact the cells' physiological response [15]. Suddenly transitioning cells experiencing exponential growth to a medium containing no carbon sources, as was performed by Schink et al. [16], will likely lead to a different physiological response to starvation as the cells have had not had the opportunity to sense and prepare for its onset, a well-documented phenomenon involving specific signaling molecules like (p)ppGpp and GTP [2, 3].

Any assay to study growth arrest in microbial populations will therefore need to make motivated decisions about both the choice of limiting nutrient and the way in which that nutrient will become limited. For our experiments, we chose to use carbon as the limiting nutrient as it is believed to be a common limiting nutrient for bacteria in natural environments, particularly in the soil [17, 18].[1]

As to the method of inducing carbon limitation, we chose to follow the approach taken by Bergkessel and Delavaine [15], where cells were allowed to grow to stationary phase and naturally deplete the nutrients in their media, but then are washed into a carbon-limited media and diluted to a low density. This helps ensure

[1] There are, of course, known examples of soil microbes being limited for other nutrients. Nitrogen limitation has been observed in tundra soils [19, 20], for example, and both nitrogen and phosphorous limitation have been observed in tropical forest soils [21, 22].

that the observed effects in the assay are truly due to nutrient starvation and not due to density-dependent factors while also ensuring that the cells in the final arrested state are indeed limited for carbon.

Assay design

Our assay consists of growing engineered fluorescent reporter strains using the Bergkessel and Delavaine approach, and inducing subsets of this population at various phases in its growth timeline. These can be measured in a high-throughput way via flow cytometry to quantitatively characterize the induction curves and compare them between the growth phases. The assay also permits the use of timelapse microscopy of these induced subpopulations to characterize any potential changes in the temporal properties of the reporter gene's expression at different growth phases. This process is schematized in Figure 5.2. An important property of this approach is that both flow cytometry and timelapse microscopy will provide measurements at the single-cell level, so that changes in population heterogeneity at the different growth phases can also be assessed quantitatively.

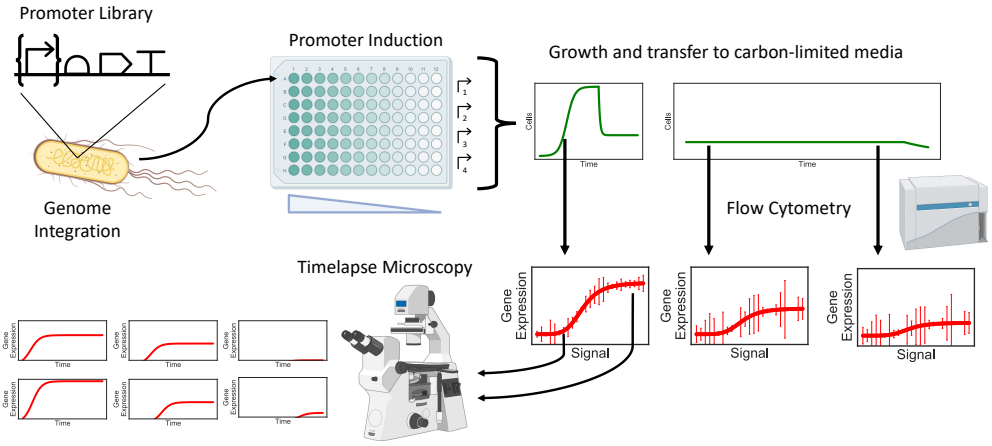

Figure 5.2: Schematic of the experimental procedure. A library of reporter strains are constructed that drive the expression of a fluorescent protein from a particular inducible promoter. These strains are grown to stationary phase in standard conditions, and then washed into carbon-limited media and diluted to a low density. Throughout various points in this growth timeline, a subset of the population can be induced with different concentrations of inducer compound– these cultures are then measured with flow cytometry to characterize the induction curves. This assay also offers the possibility of performing timelapse microscopy on the cultures upon induction in order to determine how the temporal properties of gene expression change under the different physiological conditions. Figure created with the assistance of BioRender.com.

For our initial implementation of the assay, we chose to make two major modifications to the original Bergkessel and Delavaine approach. First, instead of using LB media for the initial growth phases, we chose to use the defined M9CA minimal media supplemented with 1g/L casamino acids, following Gefen et al. [10]. Second, we chose to dilute the stationary phase cultures to an OD600 value of approximately 0.0025, rather than to 0.5 as Bergkessel and Delavaine did. In these initial tests, we also chose to focus exclusively on flow cytometry and measure the induction curves at two timepoints: one during exponential phase growth and one 48 hours after the cells were transitioned into carbon-limited media.

Initial choice of promoters

It now remained to choose a candidate organism and set of promoters to use in our initial assay. For the choice of organism, we decided to use E. coli for two major reasons. First, as it is the model synthetic biology host organism, the vast majority of existing genetic part characterization was performed within its host context. Second, although synthetic biologists often think of E. coli as a gut microbe, it actually has a biphasic life cycle where it spends time both inside mammalian intestinal tracts but also in external environments like soils [23]. It is therefore reasonable to expect that the evolutionary forces selecting for particular transcriptional response profiles under environmentally-relevant growth arrest conditions would be present in E. coli.

For the initial choice of promoters, we wanted a minimal set that covered a diversity in the various properties that might affect the induction curve. These include:

- The bioavailability of the inducer molecule, relating to the properties of its import and potential catabolism in different growth phases.
- The mechanism and affinity of binding between the inducer and the transcription factor, and whether this induces or inhibits its activity.
- The mechanism and affinity of binding between the transcription factor and the DNA, and the mechanism by which the transcription factor interacts with RNA polymerase.
- Promoter-specific transcriptional activity effects, such as those relating to the specific sigma factor(s) driving expression from the promoter.

We converged on a set of three inducible promoters: P_{Sal} , P_{Tet} , and P_{Tac} . These promoters differ in their origins: P_{Sal} originally comes from *Pseuodmonas putida*

[24], while P_{Tet} comes from an E. coli-associated mobile genetic element [24] and P_{Tac} is a synthetic hybrid promoter made by fusing elements of the native E. coli promoters P_{Trp} and P_{Lac} [10]. They also differ in their regulatory architecture, as P_{Sal} is driven by the LysR-family transcriptional activator NahR and P_{Tet} and P_{Tac} are driven by repressors (the TetR-family repressor TetR and the LacI/GalR-family repressor LacI, respectively). The promoters also differ in the function of the pathways that they natively regulate. P_{Sal} and P_{Tac} are both related to carbon metabolism, as P_{Sal} is involved in the catabolism of napthalene [25, 26] and the source promoters of P_{Tac} , P_{Trp} and P_{Lac} , are involved in the catabolism of tryptophan and lactose, respectively. P_{Tet} , on the other hand, is involved in the expression of a multi-drug efflux pump which confers resistance to tetracycline [27]. Finally, P_{Tac} is one of the two inducible promoters used by Gefen et al. [10], so that the results from our two assays can be compared for the same system.

5.4 Results

E. coli growth ceases within 48 hours of carbon limitation

We first began by confirming that E. coli cells are indeed in a growth-arrested state 48 hours after transitioning into carbon-limited media, when we planned to induce them. We performed a timelapse microscopy assay where cells were allowed to grow to stationary phase in M9CA minimal media, and then washed into carbon-limited media and diluted down to low density. At this point, cells were spotted onto agarose pads created from the carbon-limited media and observed over time. It was assumed that E. coli cannot metabolise agarose for use as a carbon source.

During the first approximately 10 hours of incubation, cells diluted into both M9 media and carbon-limited media both grew into microcolonies (Figure 5.3), presumably using excess carbon and energy stores carried over from the original stationary-phase conditions. By the time 1 day had passed, however, the M9 condition had overgrown the field of view while the carbon-limited microcolony was roughly stable, with very little cell growth being observed over the next 48 hours. Cells at the very periphery of the microcolony were, however, able to divide at a very slow rate (no more than 1-2 observed divisions over the 2 day window), as can be seen by the changes in the microcolony periphery in Figure 5.3. These results are consistent with expectations that long-term nutrient-limited populations of E. coli exhibit very slow rates of growth that balance the death of other cells in the population to maintain an approximately constant live cell density [28].

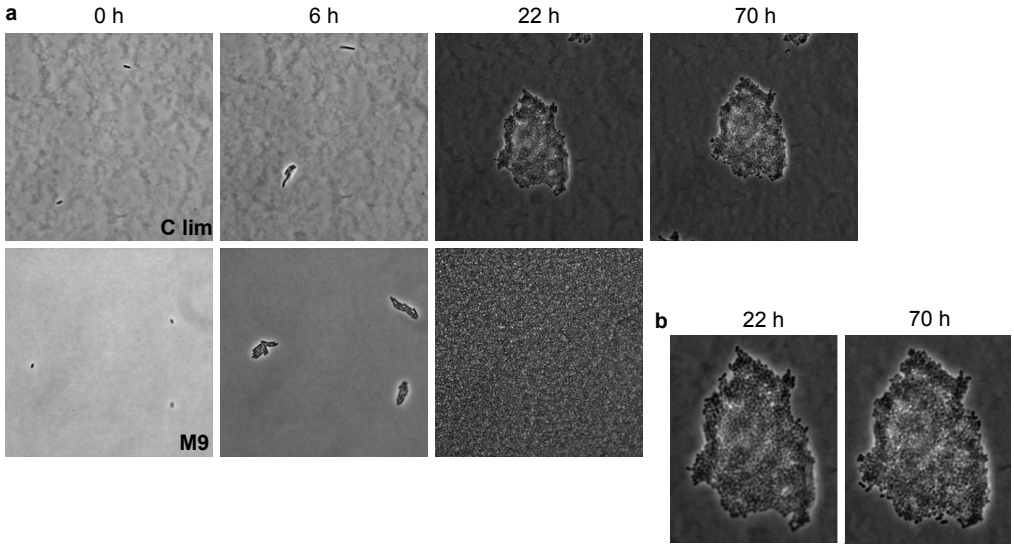

Figure 5.3: Timecourse of E. coli growth over time under carbon-limited or carbon-replete media. (a) Snapshots of E. coli growth after dilution from a stationary culture into carbon-limited media (top row) or fresh M9 media (bottom row). Some drifting in the field of view occurs between each image. (b) Focus on the central microcolony in the 22h and 70h images of the carbon-limited condition, aligned to a similar position for better comparison.

We assumed that these results were indicative of the physiological state of the cells during the actual experimental assay, although in the latter case the cells would experience the addition of inducer molecules at the point analogous to 0 hours in the microscopy assay above. However, for the the inducible expression systems that we chose for our initial test, all three inducers are expected to be non-metabolizable by E. coli. atc and IPTG, the inducers for P_{Tet} and P_{Lac} , are documented in the literature as being non-metabolizable by E. coli [10]. And although P_{Sal} evolved in the context of the regulation of a carbon metabolism pathway, to our knowledge its inducer salicylate has not been observed to be metabolized by E. coli– in fact, salicylate typically acts as a growth inhibitor through various mechanisms including the formation of reaction oxygen species [29].

The induction curves of different promoters respond differently to carbon starvation

We therefore proceeded to construct reporter strains by genomically integrating a cassette containing constitutive expression of a specific transcription factor and a sfGFP driven by its cognate inducible promoter. We then used these strains to conduct the experimental assay described in Section 5.3. After obtaining at least

10, 000 fluorescence measurements for each reporter strain in each condition, we performed density-dependent thresholding to exclude all measurements that fell outside the densest region of the forward scatter - side scatter plot in order to help ensure that each observation consisted of a single individual cell (Figure 5.4). We used a 40% inclusion threshold, following Razo-Mejia et al. [30].

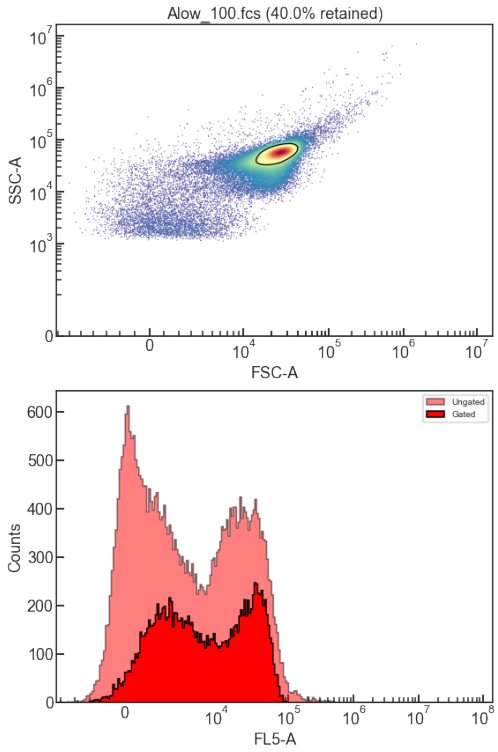

Figure 5.4: Representative gating profile for a single experimental condition. A density-dependent threshold (black contour, top) was applied to the forward scatter - side scatter plot to exclude 60% of the measured events. This gate was propagated to the GFP fluorescence channel (bottom).

We then fit the median fluorescence value F for each inducer concentration I to a phenomenological Hill function, following standard procedure in the field [24], given by

$$F(I) = \alpha + \beta \frac{I^n}{K^n + I^n}, \tag{5.1}$$

where α represents the amount of leaky gene expression, β represents the maximal activity of the promoter, K is the half-activation constant, and n represents the sharpness of the response[2].

[2]Note that Equation 5.1 can be applied to inducible systems governed by both activators and repressors– the only difference will be that the mechanistic interpretation of K, for example whether it is proportional to the regulator:DNA binding affinity, will be inverted for the two architectures.

Figures 5.5, 5.6, and 5.7 show the results from these initial measurements. Looking at the P_{Sal} (Figure 5.5) and P_{Tet} (Figure 5.6) results, we immediately see a striking increase in the heterogeneity of the populations induced during growth arrest. These populations display a pronounced multimodality during carbon starvation– the P_{Sal} response is bimodal at high concentrations of salicylate, and the P_{Tet} response transitions between bimodality and trimodality.

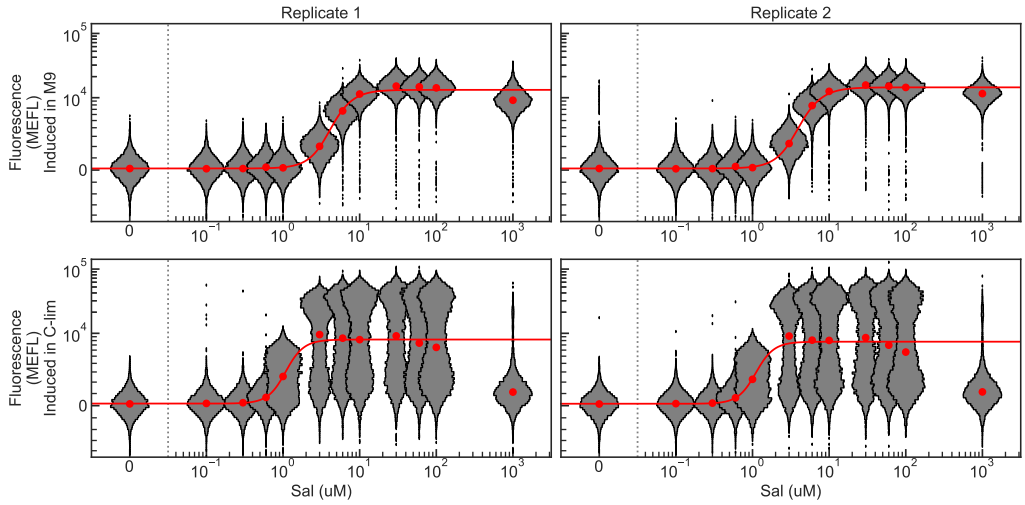

Figure 5.5: Response of the P_{Sal} reporter strain to induction by salicylate during exponential phase (top row) and during carbon starvation (bottom row). Both biological replicates were measured on the same day under the same conditions. Fluorescence values are measured in absolute units (Molecules of Equivalent Fluorescein, MEFL). Red dots indicate the median fluorescence values of each condition, and the smooth curve is obtained by fitting these medians to Equation 5.1.

Because the results of our flow cytometry measurements are calibrated to absolute fluorescence units (Methods), we can also see that the fluorescence values observed in the brightest modes of the populations induced during growth arrest are of comparable magnitude to, and sometimes even brighter than, the fluorescence values observed in the populations induced during the exponential growth phase. This is consistent with the hypothesis that bacterial populations under long-term nutrient starvation might experience a pronounced heterogeneity where a small subset of the population retains a large amount of gene expression capacity (M. Bergkessel, personal communication).

We also noted that the two population states responded differently to a given concentration of inducer. Cells under carbon starvation appeared to be more susceptible to

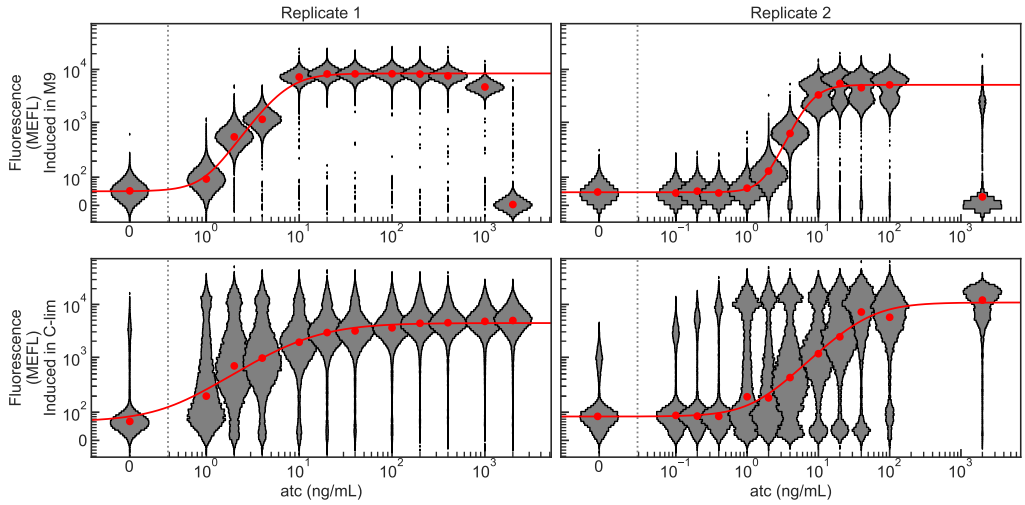

Figure 5.6: Response of the P_{Tet} reporter strain to induction by atc during exponential phase (top row) and during carbon starvation (bottom row). The biological replicates were measured on different days using different inducer concentrations (note the x axis values). Fluorescence values are measured in absolute units (Molecules of Equivalent Fluorescein, MEFL). Red dots indicate the median fluorescence values of each condition, and the smooth curve is obtained by fitting these medians to Equation 5.1.

salicylate toxicity[3], yielding almost no GFP response to 1 mM salicylate induction despite the fact that only a slight toxicity was detected at the same concentration in exponential phase (Figure 5.5). In contrast, cells exhibited the opposite response to atc– induction with 2 mg/mL atc was toxic to cells in exponential-phase growth, but yielded the strongest GFP response when those same cells were instead induced after 48 hours of carbon starvation (Figure 5.6).

Although atc exhibits reduced antibacterial activity compared to tetracycline [32], it can still function as an antibiotic at sufficiently high concentrations. Since the mechanism of action of tetracycline is to inhibit translation [33], it is not immediately apparent why the growth-arrested physiology should confer a natural resistance to atc's antibiotic activity, as it might be if it acted via a growth-related mechanism like inhibiting cell wall synthesis. Further investigation into possible mechanisms for this resistance, like a natural upregulation of antibiotic efflux pumps during carbon starvation, may be interesting.

[3]Note that this notion of 'toxicity' is inferred entirely from a lack of GFP expression in the cells. Direct measurements of cell viability without specifically sorting out target subpopulations is difficult– commonly-used proxies like propidium iodide, which stains for membrane permeability, are known to consistently yield false negatives when used as a measure of cell viability [31].

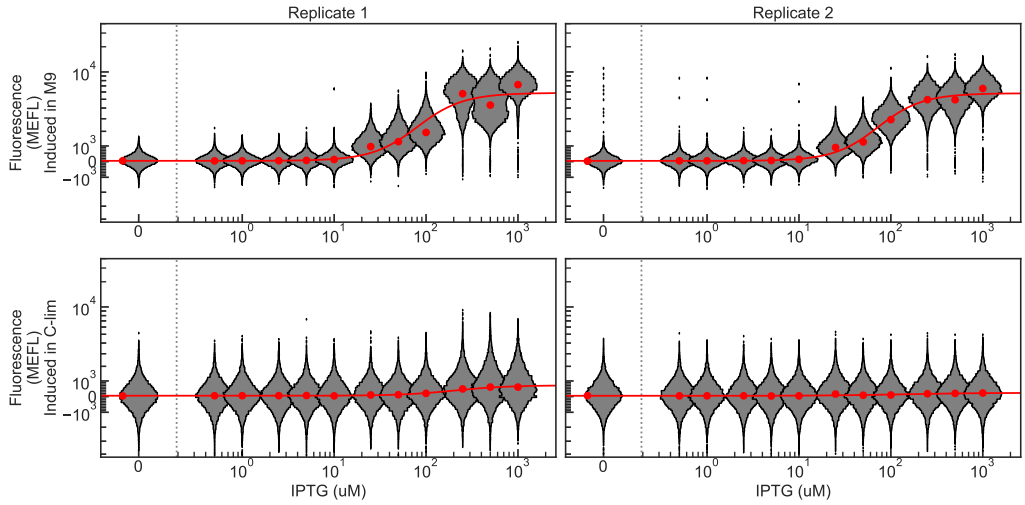

Figure 5.7: Response of the P_{Tac} reporter strain to induction by IPTG during exponential phase (top row) and during carbon starvation (bottom row). Both biological replicates were measured on the same day under the same conditions. Fluorescence values are measured in absolute units (Molecules of Equivalent Fluorescein, MEFL). Red dots indicate the median fluorescence values of each condition, and the smooth curve is obtained by fitting these medians to Equation 5.1.

Despite the fact that the P_{Sal} and P_{Tet} systems showed strong induction in the growth-arrested population, the P_{Tac} reporter strain exhibited an almost undetectable level of response when it was induced with IPTG during growth arrest (Figure 5.7). Interestingly, P_{Tac} was one of the two expression systems reported by Gefen et al. [10] to be inducible during stationary phase. As our starvation procedure is likely more stressful to the cells then those used by Gefen et al., it may be that the cells have entered a distinct physiological state where they no longer respond to IPTG. Further investigation of this question is warranted.

Because each induction curve was fit to a Hill-type function (Equation 5.1), the values of its four parameters obtained from each fit could be used to represent how each system's induction properties shifted from exponential phase to growth arrest. By doing this, we saw that P_{Sal} and P_{Tet} shifted most of their parameters in opposite directions– the P_{Sal} induction curve became more sensitive (lower K) and more switchlike (higher n) under growth arrest, while the P_{Tet} induction curve became less sensitive and more graded (Figure 5.8). Both P_{Sal} and P_{Tet} increased their leaky expression levels under growth arrest, and P_{Sal} decreased its maximal expression while P_{Tet} was inconclusive between its two replicates. However, the fact that these parameter values were obtained from fitting to the median of a

multimodal distribution means that the expression-strength values α and β may not be representative of the behavior of a specific individual cell.

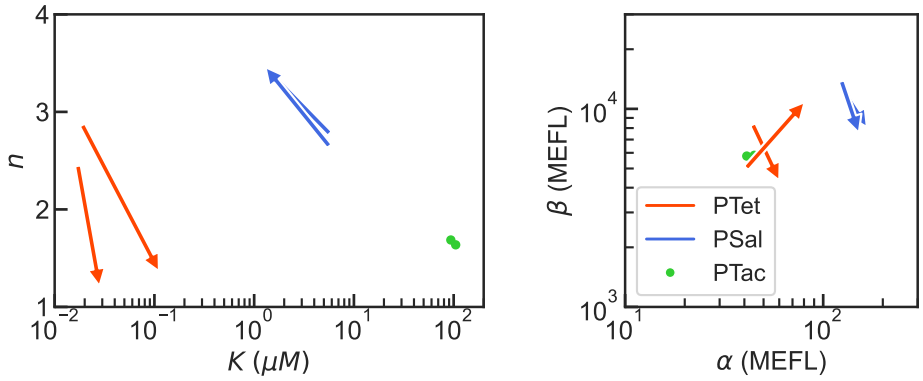

Figure 5.8: Shifts in induction curve properties from exponential phase to growth arrest. The tails and heads of the arrows show the values of the fit parameters from the exponential phase and growth arrested induction curves, respectively. Each arrow is one biological replicate– recall that the P_{Tet} replicates were measured on two different days while the P_{Sal} and P_{Tac} replicates were measured on the same day. Fit parameters for growth-arrested P_{Tac} reporter cells are not shown because the cells did not respond to induction. atc values were converted to μM to allow direct comparison with the other inducers. Data are from Figures 5.5 - 5.7.

P_{Sal} induction under carbon starvation is inhibited by cell density

We close this section by pointing out a serendipitous observation– when stationary-phase cells containing the P_{Sal} reporter construct were diluted to an optical density of 0.5 following the wash into carbon-limited media, rather than to an optical density of approximately 0.0025 as was done for the data shown in Figures 5.5-5.8, the cells no longer responded to salicylate induction at any of the tested concentrations (Figure 5.9). These optical density values correspond approximately to cell densities of $2 * 10^7$ and $1 * 10^5$ cells per mL, and interestingly this higher density was the one used by Bergkessel and Delavaine [15] in their growth arrest experiments.

While it is intriguing to speculate on the potential causes and consequences of this density-dependent inducibility (e.g. whether the inability of P_{Tac} to induce during growth arrest was also related to a density effect), these observations are still very much preliminary– we have not yet even assessed whether this effect is observable with other promoters. Awareness of this potential phenomenon, however, seems prudent for further studies of gene expression in long-term starvation conditions.

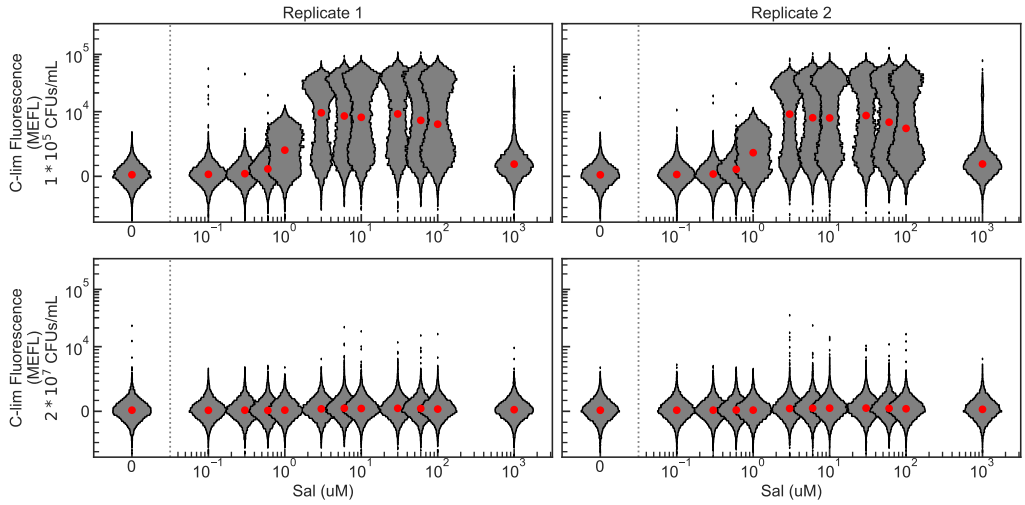

Figure 5.9: Induction of P_{Sal} reporter strains with salicylate during carbon starvation in cultures of different densities. The data from the low-density condition (top row) is the same data presented in Figure 5.5. Fluorescence values are in absolute units (Molecules of Equivalent Fluorescein, MEFL). Red dots indicate the median fluorescence values of each condition.

5.5 Future directions: Isolating transcriptional response curves

The results presented in the previous section suggest that a larger screen covering many of the inducible promoters typically used in synthetic biology would be feasible. Furthermore, the fact that different promoters in our initial screen responded to carbon starvation in different ways (Figure 5.8) suggests that the results of such a screen might potentially be useful in revealing general trends of how different classes of promoters might respond in different but consistent ways to this transition. However, one issue with our assay is that such a trend, even if observed, would be purely phenomenological– in order to gain any insights into the molecular mechanisms underlying such potential trends, the assay would need to be modified to, at the very least, isolate the influences of the inducer and of the regulator.

To illustrate this point, consider a simple model of inducible gene regulation (in this case, an inducible repressor). We will say that the inducer can diffuse in and out of the cell to take states I_{in} or I_{ex}, respectively, and that the internal inducer can reversibly bind to the regulator R. Thus this system is governed by the binding reactions

$$\begin{aligned} I_{\text{ex}} &\rightleftharpoons I_{\text{in}} \\ I_{\text{in}} + R &\rightleftharpoons R_I. \end{aligned} \tag{5.2}$$

If we assume that the reactions in network 5.2 occur at a faster timescale than transcription, then we obtain the quasi-equilibrium expressions

$$I_{\text{in}} = \frac{I_{\text{ex}}}{K_I},$$
$$R_I = \frac{RI_{\text{in}}}{K_R}, \tag{5.3}$$

where K_I and K_R are the dissociation constants of their respective reactions. If we then model the regulation of the activity A of the gene by the repressor R using a standard Hill-type repression function

$$A = \alpha + \beta \frac{1}{1 + \left(\frac{R}{K_G}\right)^n}, \tag{5.4}$$

then combining Equations 5.3 and 5.4 yields the following expression for the activity A as a function of the external inducer concentration I_{ex}:

$$A(I_{\text{ex}}) = \alpha + \beta \frac{1}{1 + \left(\frac{R_I}{I_{\text{ex}}} \frac{K_R K_I}{K_G}\right)^n}. \tag{5.5}$$

$A(I_{\text{ex}})$ increases monotonically with I_{ex}.

Comparing Equation 5.5 to the empirical function used to fit the flow cytometry data (Equation 5.1), we see that the observed value of K obtained from our measurements manifests as a parameter cluster $K_G/K_R K_I$ in our more mechanistic model. This means that the relative contributions of each molecular component cannot be disentangled from each other using our measurements[4].

In this section we describe a variant on the experimental approach presented in Section 5.3 that can isolate the impact of the transcription factor specific properties underlying any potential trends in how transcriptional response curves shift between exponential phase and growth arrest. Such insights would not only be valuable to researchers studying bacterial adaptation to long-term stress conditions, but also would have an intrinsic value to synthetic biologists. Transcriptional response curves, particularly for repressors, are the basis for the function of many important classes of genetic circuits, including bistable memory switches [35] and logical computation circuits [36] .

[4] An exception to this point is if there exists a set of two inducible promoters that can each be activated by two different inducers. By measuring all four pairwise combinations of inducer and promoter, one would obtain four equations with four unknowns and could therefore isolate the general contribution of the individual inducers and regulators. This scenario could potentially be obtained using chimeric transcription factors if the chimera variants are assumed to have identical regulation properties– but this assumption is not supported by the literature [34].

Experimental procedure

In order to isolate the impact of transcription factor-specific properties from the impact of inducer-specific properties in the response curves for different promoters, we can follow the approach taken by Parisutham et al. [37] and tag the transcription factor regulating the promoter with a fluorescent protein. When this tagged transcription factor is then placed under inducible control its concentration can be tracked directly, bypassing any physiological or inducer-specific properties that would affect the expression of the transcription factor in different conditions. By then expressing a spectrally-distinct fluorescent protein under the control of the tagged transcription factor, the two fluorescent proteins could be measured simultaneously in single cells to obtain a single empirical transcriptional response curve in a given physiological state.

In order for this procedure to truly decompose the influence of inducer-specific properties from transcription factor-specific properties, however, the transcription factor must be able to operate in the absence of the inducer. This means that this assay would only be applicable to transcriptional repressors, which operate via steric hindrance of RNA polymerase and can therefore act without the inducer present, and a small set of transcriptional activators that do not require inducers to function (e.g. the T7 phage RNA polymerase). However, as pointed out above, transcriptional repression curves are of central importance to genetic circuit design (Figure **??**). So this assay, even with its restricted scope, would still yield valuable results for the field.

Preliminary result

As an initial test of this approach, we constructed five reporter strains that use P_{Tet} to drive the expression of evolved repressors from the Marionette library that are optimized for strongly-defined induction curves [24]. These repressors were tagged with the mCherry variant used by Parisutham et al. [37] and integrated onto the E. coli genome alongside a sfGFP cassette driven by the cognate repressed promoter.

Initial characterization of these strains revealed that the fluorescence signal from the mCherry-tagged repressors was too dim to observe via either plate readers or flow cytometry, although it was observable using a fluorescent microscope (Figure 5.10). Modifying this assay to enable a high-throughput screening of a large library of repressors will therefore require optimizing the brightness of the red protein or creating a scalable process for high-throughput microscopy.

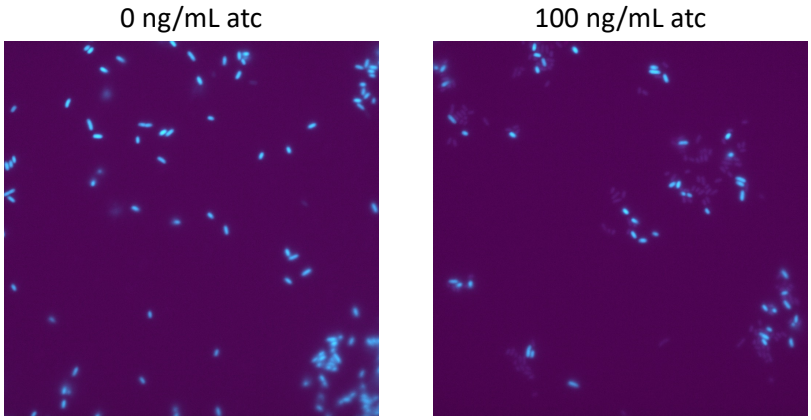

Figure 5.10: Representative images of the P_{Tet} LacI-mCherry P_{Lac} sfGFP strain with and without induction of the P_{Tet} promoter. Cells were induced at exponential phase and grown for 24 hours prior to imaging. The sfGFP and mCherry channels are colored as cyan and magenta, respectively. The two images share the same lookup table so the intensity values are comparable. LacI-mCherry is dimly visible under P_{Tet} induction (right) but not in its absence (left).

Discussion

The potential results from such an experiment would be exciting in that it would provide some of the first direct observations of the functional impact of growth-arrested physiology on the regulatory activity of specific transcription factors. Such results would have interesting implications when set against the known physiological adaptations that E. coli undergoes in growth arrest, particularly the global compaction of its chromosome into a crystalline state via the protein Dps [38].

Janissen et al. [39] presented the intriguing result that Dps-mediated chromosome compaction does not influence transcriptional activity in stationary phase E. coli. This was supported by two lines of evidence– first, the transcriptome and proteome of Δ*dps* mutants were not detectably different from wild-type cells 24-96 hours after the onset of stationary phase. However, this assay does not specifically isolate the impact of new transcription that occurred after Dps-mediated chromosome compaction became prevalent within the cell, and could be biased by transcripts and proteins that persist from a pre-compaction state. Second, the authors found through an in vitro assay that RNA polymerase can transcribe Dps-bound genes, and that the transcriptional repressor LexA can prevent such transcription from Dps-bound DNA. Whether other types of transcription factors can access Dps-bound DNA, however was not determined– this is particularly relevant given that the activity

of other types of DNA-binding proteins, such as restriction endonucleases, were blocked by Dps under the same conditions.

Determining whether this result holds more generally to other types of transcription factors will be an interesting question enabled by this research– an intriguing possibility is that different transcription factor families, which have different DNA-binding modalities [40–48], might be affected in different ways by the Dps-compacted DNA present in growth-arrested cells. Insights like these would not only pave the way towards more reliable engineering of genetic circuit intended to operate in growth-arrested cells, but also advance our fundamental understanding of the various strategies that microbes adopt to survive under conditions of long-term nutrient limitation.

5.6 Materials and methods

Strain and construct assembly

The parent strain of the Keio single-gene knockout library, E. coli BW25113 [49], was used as the basis for all strains with the exception of the LacI-mCherry strain shown in Figure 5.10, which was constructed from the Δ*ara* Δ*lac* mutant JS006 [50]. Reporter cassettes were constructed using 3G assembly [51] and integrated onto the genome alongside a kanamycin resistance cassette using the pOSIP clonetegration system [52].

Media preparation

The M9CA minimal media was purchased from Teknova. For making the carbon-limited media, a 100X base solution was first prepared by adding 100g NaCl, 40g MgCl2·6H2O, 10g CaCl2·2H20, and 50g KCl to 1L of water and sterilizing it by autoclave. The carbon-limited media was then prepared by combining 10 mL of the base solution, 10 mL of ATCC trace mineral supplement MD-TMS, 10 mL of 0.5M ammonium chloride (filter-sterilized), 250 µL of 1M sodium sulfate (filter-sterilized), 1 mL of 100 mM potassium phosphate (filter-sterilized) and sterilized deionized water to a total volume of 1 L.

Cell culturing

Individual colonies of each cell strain was grown overnight in 2 mL of M9CA media with kanamycin selection in a 15 mL polypropylene culture tube in a shaking incubator set to 30C and 250rpm. The following morning, these cultures were diluted 1:500 into 500 µL of fresh M9 media with kanamycin selection alongside

the appropriate concentration of inducer and returned to the shaking incubator. 24 hours after induction, these cells were prepared for flow cytometry.

Simultaneously, the original overnight culture was washed into carbon-limited media at this point by spinning the cells at 1,377g for 10min, removing the supernatant, and resuspending it in an equivalent volume of carbon-limited media. This wash was performed twice. The OD600 value of the culture was then measured and the cells were diluted in fresh carbon-limited media (without kanamycin selection) to a density corresponding to an OD600 value of approximately 0.0025 in a total volume of 8 mL. This culture was returned to the shaking incubator and remained there for 48 hours, after which it was split into 12 individual 500 uL cultures, which were each induced with an appropriate concentration of inducer. These cultures were returned to the shaking incubator for another 24 hours before being prepared for flow cytometry.

Flow cytometry

Cultures were prepared for flow cytometry by passing them through a 40 μm filter to eliminate large clumps of cells. During each flow cytometry session, calibration beads (Spherotech Rainbow Calibration Particles RCP-30-5A) were measured to serve as a reference standard for conversion of fluorescence values to absolute units [53].

Curve fitting

Density gating on the fluorescence distributions were performed as described in Figure 5.4. The medians of the gated fluorescence distributions were fit by nonlinear least-squares error minimization using the python LMFIT package [54] to Equation 5.1 after log-transforming the data so large values do not dominate the residuals.

5.7 Acknowledgments

I would like to thank Megan Bergkessel and Dianne Newman for insightful discussions on the design of this project, Jamie Tijerina of the Caltech Flow Cytometry facility for her assistance with flow cytometry, Mark Prator for helping construct and measure the strains, and Elin Larsson for our discussions on experimental design.

References

[1] Ilenne Del Valle et al. "Translating New Synthetic Biology Advances for Biosensing Into the Earth and Environmental Sciences". *Frontiers in Microbiology* 11 (2021).

[2] Megan Bergkessel, David W. Basta, and Dianne K. Newman. "The physiology of growth arrest: uniting molecular and environmental microbiology". *Nature Reviews Microbiology* 14.9 (2016), pp. 549–562.

[3] Jonathan Dworkin and Caroline S. Harwood. "Metabolic reprogramming and longevity in quiescence". *Annual Review of Microbiology* 76 (2022), pp. 91–111.

[4] Roberto Kolter, Deborah A. Siegele, and Antonio Tormo. "The stationary phase of the bacterial life cycle". *Annual Review of Microbiology* 47.1 (1993), pp. 855–874.

[5] Karin E. Kram, Autumn L. Henderson, and Steven E. Finkel. "Escherichia coli has a unique transcriptional program in long-term stationary phase allowing identification of genes important for survival". *Msystems* 5.4 (2020), e00364–20.

[6] David W. Basta, Megan Bergkessel, and Dianne K. Newman. "Identification of Fitness Determinants during Energy-Limited Growth Arrest in Pseudomonas aeruginosa". *mBio* 8.6 (2017). Ed. by Marvin Whiteley.

[7] Megan Bergkessel. "Regulation of protein biosynthetic activity during growth arrest". *Current Opinion in Microbiology* 57 (2020), pp. 62–69.

[8] Brett M. Babin et al. "SutA is a bacterial transcription factor expressed during slow growth in Pseudomonas aeruginosa". *Proceedings of the National Academy of Sciences* 113.5 (2016).

[9] Megan Bergkessel et al. "The dormancy-specific regulator, SutA, is intrinsically disordered and modulates transcription initiation in Pseudomonas aeruginosa". *Molecular Microbiology* 112.3 (2019), pp. 992–1009.

[10] Orit Gefen et al. "Direct observation of single stationary-phase bacteria reveals a surprisingly long period of constant protein production activity". *Proceedings of the National Academy of Sciences* 111.1 (2014), pp. 556–561.

[11] Philip Bittihn et al. "Genetically engineered control of phenotypic structure in microbial colonies". *Nature Microbiology* 5.5 (2020), pp. 697–705.

[12] Astrid G. Chapman, Lana Fall, and Daniel E. Atkinson. "Adenylate energy charge in Escherichia coli during growth and starvation". *Journal of Bacteriology* 108.3 (1971), pp. 1072–1086.

[13] Sophia Hsin-Jung Li et al. "Escherichia coli translation strategies differ across carbon, nitrogen and phosphorus limitation conditions". *Nature Microbiology* 3.8 (2018), pp. 939–947.

[14] Guennadi Sezonov, Daniele Joseleau-Petit, and Richard D'Ari. "Escherichia coli Physiology in Luria-Bertani Broth". *Journal of Bacteriology* 189.23 (2007), pp. 8746–8749.

[15] Megan Bergkessel and Laurent Delavaine. "Diversity in starvation survival strategies and outcomes among heterotrophic proteobacteria". *Microbial Physiology* 31.2 (2021), pp. 146–162.

[16] Severin J. Schink et al. "Death Rate of E. coli during Starvation Is Set by Maintenance Cost and Biomass Recycling". *Cell Systems* 9.1 (2019), 64–73.e3.

[17] Louise Aldén, Fredrik Demoling, and Erland Baath. "Rapid method of determining factors limiting bacterial growth in soil". *Applied and Environmental Microbiology* 67.4 (2001), pp. 1830–1838.

[18] Fredrik Demoling, Daniela Figueroa, and Erland Bååth. "Comparison of factors limiting bacterial growth in different soils". *Soil Biology and Biochemistry* 39.10 (2007), pp. 2485–2495.

[19] Riikka Rinnan et al. "Mineralization and carbon turnover in subarctic heath soil as affected by warming and additional litter". *Soil Biology and Biochemistry* 39.12 (2007), pp. 3014–3023.

[20] Seeta A. Sistla, Shinichi Asao, and Joshua P. Schimel. "Detecting microbial N-limitation in tussock tundra soil: implications for Arctic soil organic carbon cycling". *Soil Biology and Biochemistry* 55 (2012), pp. 78–84.

[21] Lei Liu et al. "Effects of nitrogen and phosphorus additions on soil microbial biomass and community structure in two reforested tropical forests". *Scientific Reports* 5.1 (2015), pp. 1–10.

[22] Tessa Camenzind et al. "Nutrient limitation of soil microbial processes in tropical forests". *Ecological Monographs* 88.1 (2018), pp. 4–21.

[23] Jan Dirk Van Elsas et al. "Survival of Escherichia coli in the environment: fundamental and public health aspects". *The ISME Journal* 5.2 (2011), pp. 173–183.

[24] Adam J. Meyer et al. "Escherichia coli "Marionette" strains with 12 highly optimized small-molecule sensors". *Nature Chemical Biology* 15.2 (2019), pp. 196–204.

[25] W. Park and E.L. Madsen. "Characterization in Pseudomonas putida Cg1 of nahR and its role in bacterial survival in soil". *Applied Microbiology and Biotechnology* 66 (2004), pp. 209–216.

[26] E. Grund, B. Denecke, and R. Eichenlaub. "Naphthalene degradation via salicylate and gentisate by Rhodococcus sp. strain B4". *Applied and Environmental Microbiology* 58.6 (1992), pp. 1874–1877.

[27] Thea S.B. Møller et al. “Relation between tetR and tetA expression in tetracycline resistant Escherichia coli”. *BMC Microbiology* 16.1 (2016), pp. 1–8.

[28] Steven E. Finkel. “Long-term survival during stationary phase: evolution and the GASP phenotype”. *Nature Reviews Microbiology* 4.2 (2006), pp. 113–120.

[29] Tiebin Wang, Imane El Meouche, and Mary J. Dunlop. “Bacterial persistence induced by salicylate via reactive oxygen species”. *Scientific Reports* 7.1 (2017).

[30] Manuel Razo-Mejia et al. “Tuning Transcriptional Regulation through Signaling: A Predictive Theory of Allosteric Induction”. *Cell Systems* 6.4 (2018), 456–469.e10.

[31] Shawn Lewenza et al. “Pseudomonas aeruginosa displays a dormancy phenotype during long-term survival in water”. *PLoS One* 13.9 (2018). Ed. by Eric Cascales, e0198384.

[32] M.L. Nelson and M.Y. Ismail. “The Antibiotic and Nonantibiotic Tetracyclines”. *Comprehensive Medicinal Chemistry II*. Elsevier, 2007, pp. 597–628.

[33] Ian Chopra and Marilyn Roberts. “Tetracycline Antibiotics: Mode of Action, Applications, Molecular Biology, and Epidemiology of Bacterial Resistance”. *Microbiology and Molecular Biology Reviews* 65.2 (2001), pp. 232–260.

[34] Sarah Meinhardt et al. “Novel insights from hybrid LacI/GalR proteins: family-wide functional attributes and biologically significant variation in transcription repression”. *Nucleic Acids Research* 40.21 (2012), pp. 11139–11154.

[35] Lauren B. Andrews, Alec A. K. Nielsen, and Christopher A. Voigt. “Cellular checkpoint control using programmable sequential logic”. *Science* 361.6408 (2018).

[36] A. A. K. Nielsen et al. “Genetic circuit design automation”. *Science* 352.6281 (2016), aac7341–aac7341.

[37] Vinuselvi Parisutham et al. “Tunable transcription factor library for robust quantification of regulatory properties in Escherichia coli”. *Molecular Systems Biology* 18.6 (2022), e10843.

[38] Sudha Nair and Steven E. Finkel. “Dps protects cells against multiple stresses during stationary phase”. *Journal of Bacteriology* 186.13 (2004), pp. 4192–4198.

[39] Richard Janissen et al. “Global DNA compaction in stationary-phase bacteria does not affect transcription”. *Cell* 174.5 (2018), pp. 1188–1199.

[40] Juan L. Ramos et al. “The TetR family of transcriptional repressors”. *Microbiology and Molecular Biology Reviews* 69.2 (2005), pp. 326–356.

[41] Sarah E. Maddocks and Petra C.F. Oyston. “Structure and function of the LysR-type transcriptional regulator (LTTR) family proteins”. *Microbiology* 154.12 (2008), pp. 3609–3623.

[42] Liskin Swint-Kruse and Kathleen S. Matthews. “Allostery in the LacI/GalR family: variations on a theme”. *Current Opinion in Microbiology* 12.2 (2009), pp. 129–137.

[43] Laura S. Busenlehner, Mario A. Pennella, and David P. Giedroc. “The SmtB / ArsR family of metalloregulatory transcriptional repressors: structural insights into prokaryotic metal resistance”. *FEMS Microbiology Reviews* 27.2-3 (2003), pp. 131–143.

[44] Nigel L. Brown et al. “The MerR family of transcriptional regulators”. *FEMS Microbiology Reviews* 27.2-3 (2003), pp. 145–163.

[45] Inna A. Suvorova, Yuri D. Korostelev, and Mikhail S. Gelfand. “GntR family of bacterial transcription factors and their DNA binding motifs: structure, positioning and co-evolution”. *PLoS One* 10.7 (2015), e0132618.

[46] Inna A. Suvorova and Mikhail S. Gelfand. “Comparative analysis of the IclR-family of bacterial transcription factors and their DNA-binding motifs: structure, positioning, co-evolution, regulon content”. *Frontiers in Microbiology* 12 (2021), p. 675815.

[47] Dinesh K. Deochand and Anne Grove. “MarR family transcription factors: dynamic variations on a common scaffold”. *Critical Reviews in Biochemistry and Molecular Biology* 52.6 (2017), pp. 595–613.

[48] Paul Thaw et al. “Structural insight into gene transcriptional regulation and effector binding by the Lrp/AsnC family”. *Nucleic Acids Research* 34.5 (2006), pp. 1439–1449.

[49] Tomoya Baba et al. “Construction of Escherichia coli K-12 in-frame, single-gene knockout mutants: the Keio collection”. *Molecular Systems Biology* 2.1 (2006), pp. 2006–0008.

[50] Jesse Stricker et al. “A fast, robust and tunable synthetic gene oscillator”. *Nature* 456.7221 (2008), pp. 516–519.

[51] Andrew D. Halleran, Anandh Swaminathan, and Richard M. Murray. “Single day construction of multigene circuits with 3G assembly”. *ACS Synthetic Biology* 7.5 (2018), pp. 1477–1480.

[52] François St-Pierre et al. “One-step cloning and chromosomal integration of DNA”. *ACS Synthetic Biology* 2.9 (2013), pp. 537–541.

[53] Jacob Beal et al. “Comparative analysis of three studies measuring fluorescence from engineered bacterial genetic constructs”. *PLOS ONE* 16.6 (2021), e0252263.

[54] Matthew Newville et al. *LMFIT: Non-Linear Least-Square Minimization and Curve-Fitting for Python*. Version 0.8.0. 2014. DOI: 10.5281/zenodo.11813.

Chapter 6

CONCLUSION

Having now concluded the presentation of these three projects, we can now re-examine them in the context of the core research priorities of environmental synthetic biology. Three of the four major research areas identified in Chapter 1 are directly addressed by the projects presented in this thesis, although each area nonetheless still has much that needs to be done.

For the area of autonomous operation and error correction, the work on DNA messaging presented in Chapter 2 provides a framework that allows an engineered consortium to dynamically control the flow of information within itself. This is a necessary condition for creating multicellular systems that can autonomously reconfigure their own organization, which will itself be a key component of engineering adaptable systems that persist across environments that change in unpredictable ways. An important next step for our work would be to harness our communication framework to implement such an autonomously-adapting system. Doing so would require closed-loop interactions between the actual content of the message and its addressing machinery, while throughout our current work the content of the message was essentially fully inert. Of course, the framework for intercellular communication is only one of many components required to engineer a multicellular consortium. To make such a consortium adaptable to variable environments, the capacity for autonomous adaptability must be similarly incorporated into its other components such as composition control systems and distributed processing modules.

In the case of control and monitoring, the preliminary work on screening the performance of inducible transcriptional response systems under growth arrest (Chapter 5) is a first step towards a more environmentally-motivated characterization of various chemical inducers. The fact that IPTG was unable to induce the P_{Tac} promoter under carbon-limited growth arrest, for example, suggests that it would be a poor choice for implementing post-deployment control of a synthetic biology system. Results such as these should be coupled with physico-chemical characterizations of the dispersal and persistence of these inducers within natural environments like soils in order to build up a comprehensive, end-to-end understanding of how different candidate inducers would actually behave under environmental application settings.

The growth arrest characterization project also relates to the challenge of ensuring robust and predictable performance for synthetic biology systems in environmental contexts, by providing empirical predictions of how transcriptional response functions would change under more environmentally-relevant physiological cell states. Of course, one cannot simply assume that the carbon-limited growth arrest we induce in our assay is fully representative of cellular conditions in natural environments. Follow-up work to assess yet again the nature of the shifts in response functions between carbon-limited growth arrest and real natural environments like soils will be required to determine the extent to which these laboratory-imposed growth arrest conditions are reasonable models of natural environments.

This challenge of accurately capturing the salient environmental variables for creating an experimental substrate highlights the value of holistic mathematical analyses that can depict the behavior of a system under all possible environments. The reaction order analysis framework that we develop in Chapters 3 and 4 is an example of such an analysis system. There are likely other potential analysis frameworks that can similarly provide meaningful insights about biological system behavior in arbitrary contexts, and efforts towards discovering and formalizing them would be fruitful. Existing theoretical work on hard bounds for noise and variability in stochastic biomolecular systems, for example, can provide a potential basis for such frameworks.

The challenge of system delivery is the final core research area for environmental synthetic biology, and the one not addressed by the three projects described in this thesis. It is also the area that is the most under-served by existing research priorities of conventional synthetic biology, as the question of delivering the system to the setting of an application in a well-controlled environment is often trivial. For environmental synthetic biology, however, this question of delivery is one of the most foundational concerns. Determining how to address this challenge, whether it be exclusively through engineering approaches or through an integrated collaboration with scientists who study the environments themselves, will be a critical choice in shaping the nature of this field in the years to come.

The future of environmental synthetic biology

Unlike synthetic biology proper, the emerging field of environmental synthetic biology has not had a single landmark publication around which many scientists, previously working in disparate fields, can rally. The rapid coalescing of viewpoints from physicists, computer scientists, and engineers that defined the culture and priorities of the nascent field of synthetic biology in the early 2000s will likely not be replicated for environmental synthetic biology.

As such, we as future environmental synthetic biologists must think carefully and critically about what we want the foundations of this new field to be. An important first step will be in attracting scientists from different research areas into this field– the domain expertise of environmental microbiologists, immunologists, soil scientists, and others will be essential in making the grand challenge of deploying engineered biological systems into these environments more tractable.

Thankfully for us, this field is still young and malleable, and has not yet hardened to become set in its ways. The decisions we make today about the questions we choose to answer, the way that we answer them, and the way we communicate these insights will have an outsized impact on the trajectory of how environmental synthetic biology will develop. It is a great responsibility that we must treat with respect and care.

Appendix A

SOME CONVENIENT LOG DERIVATIVE FORMS

For general positive functions $f(x), g(x)$,

$$\frac{\partial \log f(x)}{\partial \log x} = \frac{x}{f(x)}\frac{\partial f(x)}{\partial x} \tag{A.1}$$

$$\frac{\partial \log(f(x)+g(x))}{\partial \log x} = \frac{f(x)}{f(x)+g(x)}\frac{\partial \log f(x)}{\partial \log x} + \frac{g(x)}{f(x)+g(x)}\frac{\partial \log g(x)}{\partial \log x} \tag{A.2}$$

If $f(\boldsymbol{x})$ is a positive multivariate monomial $k\boldsymbol{x}^{\boldsymbol{n}}$, e.g. $f(x) = kx_1^{n_1}x_2^{n_2}$, then

$$\frac{\partial \log f(\boldsymbol{x})}{\partial \log \boldsymbol{x}} = \boldsymbol{n}, \qquad \frac{\partial \log f(x_i)}{\partial \log x_i} = n_i. \tag{A.3}$$

If $f(\boldsymbol{x})$ is a positive rational function where the numerator is one of the terms in the polynomial denominator, i.e.

$$f(\boldsymbol{x}) = \frac{k_{j'}\boldsymbol{x}^{\boldsymbol{n}_{j'}}}{\sum_j k_j \boldsymbol{x}^{\boldsymbol{n_j}}},$$

then

$$\frac{\partial \log f(\boldsymbol{x})}{\partial \log x_i} = \sum_{j\neq j'}(n_{j'i} - n_{ji})\frac{k_j \boldsymbol{x}^{\boldsymbol{n_j}}}{\sum_a k_a \boldsymbol{x}^{\boldsymbol{n_a}}}. \tag{A.4}$$

Equation (A.4) is useful in situations that are often observed in models of biomolecular reaction systems. Some specific illustrative examples are:

$$\frac{\partial \log(x+\alpha)}{\partial \log x} = \frac{x}{\alpha + x} \tag{A.5}$$

$$\frac{\partial \log\left(\beta\frac{x^n}{K^n+x^n}\right)}{\partial \log x} = n\left(\frac{K^n}{K^n+x^n}\right) \tag{A.6}$$

$$\frac{\partial \log\left(\beta\frac{K^n}{K^n+x^n}\right)}{\partial \log x} = -n\left(\frac{x^n}{K^n+x^n}\right) \tag{A.7}$$

Appendix B

PROCEDURE FOR OBTAINING REACTION ORDER VERTICES AND EDGES

Finding the dominance regimes

We will begin by formally defining the notion of a dominance regime. A *dominance regime* is a region of concentration space where each conserved quantity $t_i = \sum_j L_{ij} x_j$ satisfies the relation $t_i \approx x_{i*}$, implying $x_{i*} \gg \sum_{j \neq i*} x_{i_j}$. In other words, we say that x_{i*} *dominates* t_i. Note that we can only asymptotically approach the equality $t_i = x_{i*}$, as reaching it would require the other x_{i_j} to take nonpositive values.

Every dominance regime for a system could be obtained by iterating over every possible permutation π of the species x_i and imposing a relation $x_{\pi_1} \gg x_{\pi_2} \gg \ldots \gg x_{\pi_n}$ on them. However, for n species there will be $n!$ such permutations and the vast majority of these will be redundant as they lead to the same dominance regime.

It is instead much easier to push the conservation law matrix $\boldsymbol{L}$ into the dominance regimes directly. Because the rows of $\boldsymbol{L}$ correspond to the conserved quantities t_i, in the asymptotic limit $\boldsymbol{A}$ of a given dominance regime, $\boldsymbol{L}$ will have exactly one nonzero entry in each row, at the column associated with the dominating species x_{i*}. We can therefore simply iterate over all nonzero entry of $\boldsymbol{L}$ and set all but one of them to zero in each row to generate every possible dominance regime $\boldsymbol{A}$. There are $\prod_i d_i$ such possibilities where d_i is the number of species involved in the conserved quantity t_i.

We note, however, that this procedure can generate invalid $\boldsymbol{A}$ matrices that do not correspond to a consistent ordering of $\boldsymbol{x}$. Consider the situation where two conserved quantities share two species, as in $t_1 = x_1 + x_2 + x_3$ and $t_2 = x_2 + x_3 + x_4$. It is impossible for $t_1 \approx x_2$ and $t_2 \approx x_3$ to simultaneously be true, as the first relation implies $x_2 \gg x_3$ and the second relation implies $x_3 \gg x_2$. Checking for these invalid results during the iterative generation of $\boldsymbol{A}$ matrices is simple, but it means that the true number of distinct dominance regimes can be less than $\prod_i d_i$.

Finding the finite elements of the reaction order polytope

Having calculated the system's dominance regimes in the previous section, we can see in general that the set $\left\{\boldsymbol{\Lambda}_{\boldsymbol{t}}^{-1} \boldsymbol{L} \boldsymbol{\Lambda}_{\boldsymbol{x}} : \boldsymbol{x} \in \mathbb{R}^n_{>0}\right\}$ forms a convex polytope in

concentration space whose vertices are the dominance regimes $\boldsymbol{A}$. We will now map the vertices of this dominance polytope into reaction order space, in order to obtain the reaction order polytope. Note that this operation will not necessarily preserve convexity.

We will write

$$\boldsymbol{H}(\boldsymbol{x}) := \frac{\partial \log \boldsymbol{x}}{\partial \log(\boldsymbol{t}, \boldsymbol{k})} = \begin{bmatrix} \boldsymbol{\Lambda_t}^{-1} \boldsymbol{L} \boldsymbol{\Lambda_x} \\ \boldsymbol{N} \end{bmatrix}^{-1} \approx \begin{bmatrix} \boldsymbol{A} \\ \boldsymbol{N} \end{bmatrix}^{-1} =: \boldsymbol{M}(\boldsymbol{x})^{-1}, \tag{B.1}$$

so that our goal is to map each dominance regime $\boldsymbol{M}(\boldsymbol{x})$ to its associated $\boldsymbol{H}(\boldsymbol{x})$. If $\boldsymbol{M}(\boldsymbol{x})$ is invertible, then we are done. Cases where $\boldsymbol{M}(\boldsymbol{x})$ is uninvertible will be treated in the next section.

Having calculated the reaction order vertices, we now want to determine how they are connected. To do so we will find the connectivity between the vertices of the concentration-space polytope (the dominance regimes), as the edges between these vertices will map to edges between the reaction order vertices (this is proven in Theorem 3.8.2 of Fangzhou Xiao's thesis [1]).

Recall that since $\left\{\boldsymbol{\Lambda_t}^{-1} \boldsymbol{L} \boldsymbol{\Lambda_x}, \boldsymbol{x} \in \mathbb{R}^n_{>0}\right\}$ is a convex polytope, its edges correspond to rank-1 changes between its vertices $\boldsymbol{A}_i$. Because the matrices $\boldsymbol{A}_i$ take the form of having each row contain only a single nonzero value (of 1), rank-1 changes between two matrices $\boldsymbol{A}_1, \boldsymbol{A}_2$ can be easily identified by checking whether they differ only in a single row (row i), which itself can only differ by shifting the location of the 1 entry between columns j_1 and j_2.

This relation can be written as

$$\boldsymbol{A}_2 - \boldsymbol{A}_1 = \boldsymbol{e}_i \boldsymbol{b}^\intercal, \tag{B.2}$$

where $\boldsymbol{e}_i$ is a vector with a single nonzero value (of 1) at entry i, and $\boldsymbol{b} = \boldsymbol{e}_{j_2} - \boldsymbol{e}_{j_1}$.

By simply iterating over all pairs of unique dominance regimes $\boldsymbol{A}_1, \boldsymbol{A}_2$ and performing the check described by Equation B.2, one can determine all of the edges between the dominance vertices. Each edge can then be mapped to reaction order space by linearly connecting the appropriate reaction order vertices $\boldsymbol{H}_1, \boldsymbol{H}_2$.

Finding the infinite reaction order vertices

The final point left to be resolved is the case where a dominance vertex $\boldsymbol{M}(\boldsymbol{x})$ is singular, so that it cannot be inverted to obtain the corresponding reaction order

vertex $\boldsymbol{H}(\boldsymbol{x})$. These cases actually correspond to vertices at infinity in reaction order space.

Because we cannot invert $\boldsymbol{M}$ to find the infinite vertex directly, we will instead approach the infinite vertex from a finite vertex that it is connected to. Consider two connected dominance vertices $\boldsymbol{M}_f, \boldsymbol{M}_\infty$ where $\boldsymbol{M}_f$ is nonsingular (and hence is associated with a finite reaction order vertex) and $\boldsymbol{M}_\infty$ is singular.

We will parametrize the edge between these dominance vertices with the scalar parameter $\lambda \in [0, 1]$, according to $\boldsymbol{M}(\lambda) = (1 - \lambda)M_f + \lambda M_\infty$. We can rewrite Equation B.1, which must be satisfied in general, using the definition of the matrix inverse as

$$\boldsymbol{M}(\lambda)\boldsymbol{H}(\lambda) = \boldsymbol{I} = \boldsymbol{H}(\lambda)\boldsymbol{M}(\lambda). \tag{B.3}$$

The infinite vertex $\boldsymbol{H}_\infty$ is therefore the limit of $\boldsymbol{H}(\lambda)$ as $\lambda \to 1$. In order to determine this limit, we will express the products of $\boldsymbol{M}(\lambda)$ and $\boldsymbol{H}(\lambda)$ in powers of λ.

From Equation B.2, we know that $\boldsymbol{M}_\infty - \boldsymbol{M}_f = \boldsymbol{e}_i\boldsymbol{b}^\intercal$. This means that we can write $\boldsymbol{M}(\lambda) = \boldsymbol{M}_f + \lambda(\boldsymbol{M}_\infty - \boldsymbol{M}_f) = \boldsymbol{M}_f + \lambda\boldsymbol{e}_i\boldsymbol{b}^\intercal$.

Now, applying the Sherman-Morrison formula, we have

$$\boldsymbol{H}(\lambda) = \boldsymbol{M}(\lambda)^{-1} = \boldsymbol{M}_f^{-1} - \frac{\lambda}{1 + \lambda\boldsymbol{b}^\intercal\boldsymbol{M}_f^{-1}\boldsymbol{e}_i}\boldsymbol{M}_f^{-1}\boldsymbol{e}_i\boldsymbol{b}^\intercal\boldsymbol{M}_f^{-1}. \tag{B.4}$$

We can rewrite the term $1 + \lambda\boldsymbol{b}^\intercal\boldsymbol{M}_f^{-1}\boldsymbol{e}_i$ in Equation B.4 as $1 - \lambda + \lambda(1 + \boldsymbol{b}^\intercal\boldsymbol{M}_f^{-1}\boldsymbol{e}_i)$. We now want to simplify the expression $1 + \boldsymbol{b}^\intercal\boldsymbol{M}_f^{-1}\boldsymbol{e}_i$ into a simple form.

Consider the matrix $\begin{bmatrix} \boldsymbol{M}_f & -\boldsymbol{b}^\intercal \\ \boldsymbol{e}_i & 1 \end{bmatrix}$. Due to the Schur complement formula, its determinant can be written as $\det(\boldsymbol{M}_f)(1 + \boldsymbol{b}^\intercal\boldsymbol{M}_f^{-1}\boldsymbol{e}_1) = 1 \cdot \det(\boldsymbol{M}_f + \boldsymbol{e}_i\boldsymbol{b}^\intercal)$. This last term is equal to $\det \boldsymbol{M}_\infty$, through Equation B.2. Since $\det \boldsymbol{M}_\infty = 0$ because $\boldsymbol{M}_\infty$ is singular, it follows that

$$1 + \boldsymbol{b}^\intercal\boldsymbol{M}_f^{-1}\boldsymbol{e}_i = 0. \tag{B.5}$$

Therefore Equation B.5 implies that $1 + \lambda\boldsymbol{b}^\intercal\boldsymbol{M}_f^{-1}\boldsymbol{e}_i = 1 - \lambda$, which will allow us to rewrite Equation B.4 in a much simpler form. For convenience, we will now define $\tau := \lambda/(1 - \lambda)$ and $\boldsymbol{R} := -\boldsymbol{M}_f^{-1}\boldsymbol{e}_i\boldsymbol{b}^\intercal\boldsymbol{M}_f^{-1}$ to obtain

$$\boldsymbol{H}(\lambda) = \boldsymbol{M}_f^{-1} + \tau\boldsymbol{R}. \tag{B.6}$$

Because $\lambda \to 1$ corresponds to $\tau \to \infty$, Equation B.6 shows that $\boldsymbol{H}_\infty$ can be conceptualized as the limit of a ray in direction $\boldsymbol{R}$ anchored at the finite vertex

$\boldsymbol{M}_f^{-1} = \boldsymbol{H}_f$. Furthermore, $\boldsymbol{R}$ can be determined directly from $\boldsymbol{M}_f$ and $\boldsymbol{M}_\infty$ as $\boldsymbol{R} = \boldsymbol{M}_f^{-1} - \boldsymbol{M}_f^{-1}\boldsymbol{M}_\infty\boldsymbol{M}_f^{-1}$ using the relation $\boldsymbol{M}_\infty - \boldsymbol{M}_f = \boldsymbol{e}_i\boldsymbol{b}^\intercal$. But we can do even better and determine $\boldsymbol{R}$ solely from $\boldsymbol{M}_\infty$.

To do so, we will rewrite the terms in Equation B.3 to obtain

$$\left((1-\lambda)\boldsymbol{M}_f + \lambda\boldsymbol{M}_\infty\right)\left(\boldsymbol{M}_f^{-1} + \tau\boldsymbol{R}\right) = \boldsymbol{I} = \left(\boldsymbol{M}_f^{-1} + \tau\boldsymbol{R}\right)\left((1-\lambda)\boldsymbol{M}_f + \lambda\boldsymbol{M}_\infty\right). \tag{B.7}$$

We can rewrite the left equality solely in terms of τ, giving

$$\boldsymbol{M}_f\boldsymbol{M}_f^{-1} + \tau\left(\boldsymbol{M}_\infty\boldsymbol{M}_f^{-1} + \boldsymbol{t}\boldsymbol{M}_f\boldsymbol{R}\right) + \tau^2\boldsymbol{M}_\infty\boldsymbol{R} = (1 + \tau\boldsymbol{I}). \tag{B.8}$$

Because this equation must be true for all $\tau \in [0, +\infty)$, the powers of τ on the left and right hand sides of the equation must match. Therefore, we have that $\boldsymbol{M}_f\boldsymbol{M}_f^{-1} = \boldsymbol{I}$, $\boldsymbol{M}_\infty\boldsymbol{M}_f^{-1} + \boldsymbol{M}_f\boldsymbol{R} = \boldsymbol{I}$, and $\boldsymbol{M}_\infty\boldsymbol{R} = \boldsymbol{0}$. Similarly if we rewrite the right equality solely in terms of τ, we obtain $\boldsymbol{M}_f^{-1}\boldsymbol{M}_f = \boldsymbol{I}$, $\boldsymbol{M}_f^{-1}\boldsymbol{M}_\infty + \boldsymbol{R}\boldsymbol{M}_f = \boldsymbol{I}$, and $\boldsymbol{R}\boldsymbol{M}_\infty = \boldsymbol{0}$.

Since all of these expressions must be true for all τ, the ray matrix $\boldsymbol{R}$ can be obtained by solving

$$\boldsymbol{M}_\infty\boldsymbol{R} = \boldsymbol{0} = \boldsymbol{R}\boldsymbol{M}_\infty. \tag{B.9}$$

However, recall that $\boldsymbol{M}_\infty$ is a singular matrix. Because we obtained $\boldsymbol{M}_\infty$ via a rank-1 change from the invertible matrix $\boldsymbol{M}_f$, we know that the rank of $\boldsymbol{M}_\infty$ must be 1 less than the rank of $\boldsymbol{M}_f$. This means that Equation B.9 is underdetermined, and so has multiple valid solutions $\widetilde{\boldsymbol{R}}$. These matrices $\widetilde{\boldsymbol{R}}$ all differ by a scalar coefficient, and so the true ray matrix $\boldsymbol{R}$ can be obtained from any given solution $\widetilde{\boldsymbol{R}}$ by finding the appropriate scalar ρ and calculating $\boldsymbol{R} = \rho\widetilde{\boldsymbol{R}}$.

Because $\boldsymbol{H}_\infty$ is the limit of $\boldsymbol{H}(\tau) = \boldsymbol{M}_f^{-1} + \tau\boldsymbol{R}$ as $\tau \to \infty$, however, we actually only need to know the sign of ρ to determine $\boldsymbol{H}_\infty$ from any given solution $\widetilde{\boldsymbol{R}}$. To do this, we first note that $\operatorname{sgn}\det\boldsymbol{H}(\boldsymbol{1}) = \operatorname{sgn}\det\boldsymbol{M}(\boldsymbol{1}) = \operatorname{sgn}\det\begin{bmatrix}\boldsymbol{L}\\ \boldsymbol{N}\end{bmatrix}$, since the sign of the determinant is preserved by the matrix inverse. Then we note that $\operatorname{sgn}\det\boldsymbol{H}(\boldsymbol{x}) = \operatorname{sgn}\det\boldsymbol{H}(\boldsymbol{1})$ for any $\boldsymbol{x} \in \mathbb{R}_{>0}$ because $\boldsymbol{M}(\boldsymbol{x})$ is invertible for all $\boldsymbol{x} \in \mathbb{R}_{>0}$ and the determinant is a continuous function, meaning its sign will never change. Thus it follows that for any $\boldsymbol{H}(\tau)$, if $\tau \in [0, \infty)$ then it must be true that $\operatorname{sgn}\det\boldsymbol{H}(\tau) = \operatorname{sgn}\det\left(\boldsymbol{M}_f^{-1} + \tau\boldsymbol{R}\right) = \operatorname{sgn}\det\begin{bmatrix}\boldsymbol{L}\\ \boldsymbol{N}\end{bmatrix}$.

Therefore, we can choose any finite value of τ and compute $\operatorname{sgn}\det\left(\boldsymbol{M}_f^{-1} + \tau\widetilde{\boldsymbol{R}}\right)$. If it is the same as $\operatorname{sgn}\det\begin{bmatrix}\boldsymbol{L}\\ \boldsymbol{N}\end{bmatrix}$, then $\widetilde{\boldsymbol{R}}$ correctly captures the orientation of the infinite ray in reaction order space. If the sign does not match, then the orientation must be flipped, so the infinite ray in reaction order space is given by $-\widetilde{\boldsymbol{R}}$.

References

[1] Fangzhou Xiao. "Biocontrol of Biomolecular Systems: Polyhedral Constraints on Binding's Regulation of Catalysis from Biocircuits to Metabolism". PhD thesis. California Institute of Technology, 2022.